university of groningen

Mitigating Flow Induced Vibrations

Using Tunable Porous Metamaterials to Diffuse Turbulence in High-Tech Industrial Applications

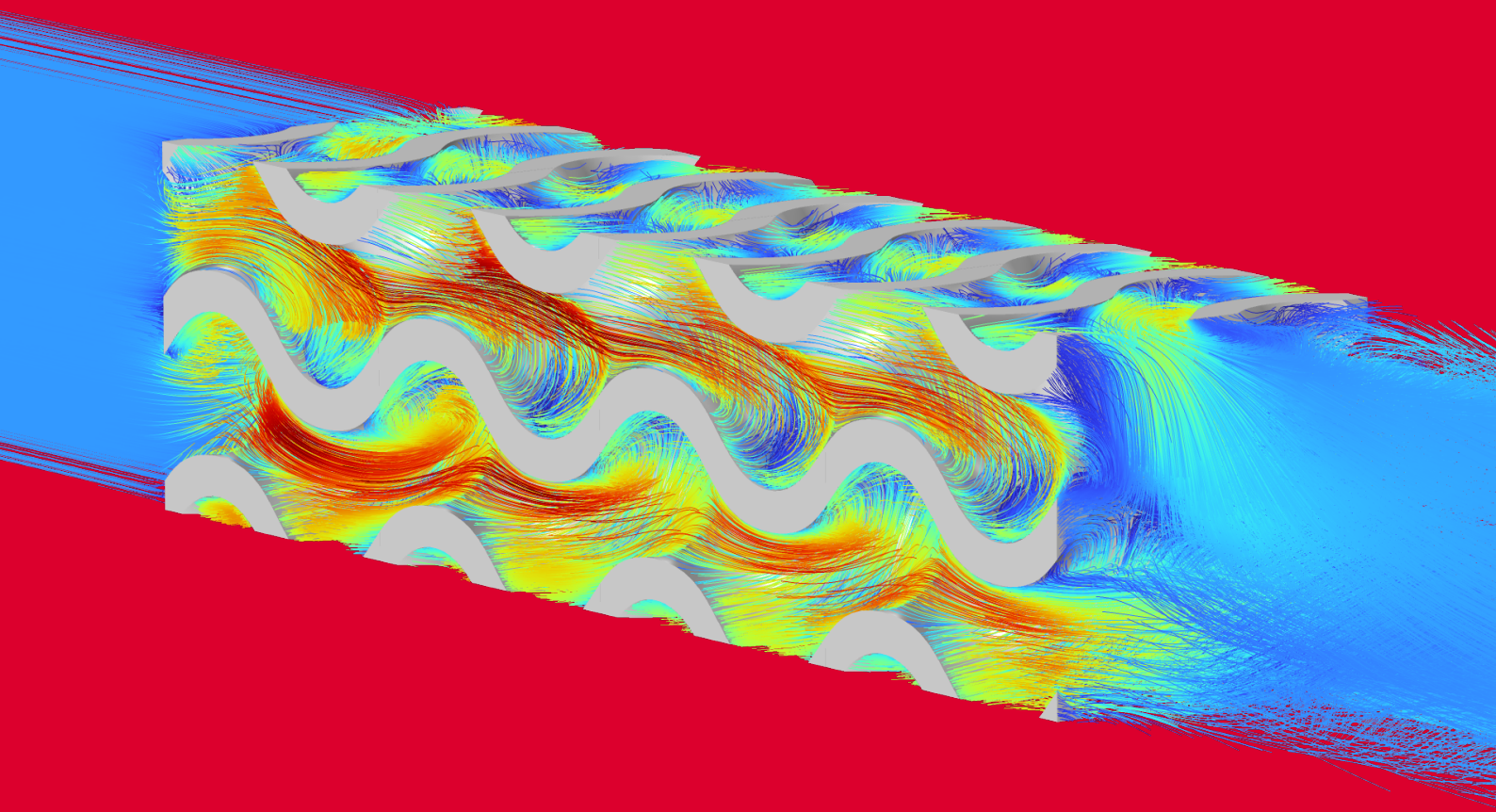

B.J.T. Piest

MSc Mechanical Engineering Research Project

February 2, 2024

university of groningen

Mitigating Flow Induced Vibrations

Using Tunable Porous Metamaterials to Diffuse Turbulence in High-Tech Industrial Applications

MSc Mechanical Engineering Research Project

Author

B.J.T. Piest | S2981521

Supervisors

dr. A.O. Krushynska
dr. ir. P.D. Druetta

February 2, 2024

Abstract

Flow induced vibrations (FIV) pose significant challenges in high-tech industries such as semiconductor manufacturing, necessitating innovative solutions to minimize their impact. This research project focuses on leveraging metamaterials concepts to reduce FIV in high-tech industrial cooling systems. More specifically, a class of metamaterials known as triply periodic minimal surfaces (TPMS). The use of TPMS in engineering applications has become increasingly feasible because of the advent of additive manufacturing.

A model was proposed to approximate the behaviour of a three-dimensional array of TPMS based on the Darcy-Forcheimer equation. Based on this model, full scale simulations of a sudden expansion were carried out to investigate the influence of TPMS inserts on FIV. The simulations revealed that TPMS structures exhibit promising characteristics for FIV mitigation, demonstrating a reduction of approximately 81 % in turbulent kinetic energy and a 12.5 % reduction in vorticity.

To validate the computational findings, two sets of experiments were conducted. The first set aimed to validate the Darcy-Forcheimer model by assessing pressure drop in a straight tube with a TPMS insert. Unexpectedly, contradictory data emerged, necessitating further investigation to conclusively validate the model. The second set of experiments focused on evaluating the TPMS inserts' effectiveness in reducing FIV. Results from hydrodynamic and acoustic pressure fluctuations indicated that the TPMS inserts did not significantly alter FIV presence, contrary to simulation expectations.

While computational simulations demonstrate TPMS structures' potential for the mitigation of, experimental discrepancies highlight the need for additional investigation and refinement of the Darcy-Forcheimer model. This study provides a starting point for more extensive research into the complex interplay between porous metamaterials and FIV in industrial applications.

Acknowledgments

I would like to extend my gratitude to project supervisors dr. Anastasiia Krushynska and dr. ir. Pablo Druetta for their continued support, guidance and valuable insights throughout this research project. I am also grateful for the help and support of Zhaohang Zhang, who was especially helpful in overcoming issues during the computational phase of this research. I would also like to extend my gratitude to Nicholas Waterson, dr. Alessia Aulitto & Ozan Erdem Demirel from ASML for their contributions, expertise and help during the experimental phase of this research. Finally, I thank the University of Groningen (UG) and ASML for providing the necessary resources and facilities for this research to succeed. Completing this MSc Mechanical Engineering Research Project without the collective support of these individuals and institutions would not have been possible.

Bastiaan J.T. Piest
MSc Mechanical Engineering
February 2, 2024

Table of Contents

List of Tables

List of Figures

List of Abbreviations

AI	artificial intelligence 10
CAD	computer aided design 28, 45
CFD	computational fluid dynamics vi, 1, 16, 27–29, 34–36, 38, 51–53, 70, 85, 86, 94
DBD	dielectric barrier discharge 9
DNS	direct numerical simulation 31, 35
EUV	extreme ultraviolet 1, 2, 4, 10, 12, 38
F-RD	Schoen F-Rhombic Dodecahedron 13, 40, 50
FDM	fused deposition modeling xi, 40, 45, 46, 87
FIV	flow induced vibrations viii, 1, 4–10, 23, 43, 44, 46, 48, 55, 65, 70–72
HPC	high-performance computing 31, 38
IPC	interpenetrating phase composites 14
IW-P	Schoen I-Graph and Wrapped Package vi, vii, xi, 13, 40, 52, 53, 61, 67, 68, 94, 97, 98
LES	large eddy simulation 31, 35
PμSLA	projection micro stereolithography ix, 46
PETG	polyethylene terephthalate glycol 45
PLA	polylactic acid 40
PSD	power spectral density x, 48, 65–67
RANS	Reynolds averaged Navier-Stokes 30, 31, 35, 64
SD	Schwarz Diamond vi, x, xi, 13, 40, 51, 53, 61, 63, 64, 94–96, 98
SG	Schoen Gyroid vi, ix–xi, 13, 40–42, 45, 46, 50, 52, 53, 56–59, 61, 63, 64, 67–69, 71, 94, 96, 98
SHS	super hydrophobic surfaces 11
SLA	stereolithography ix, 41, 45, 46
SP	Schwarz Primitive vi, x, xi, 13, 51, 53, 55, 60, 61, 94, 95, 98
TPMS	triply periodic minimal surfaces vi, viii–x, xv, 6, 12–15, 31, 32, 38–46, 48, 50–56, 58–61, 63–65, 67–72, 81–83, 94
UG	University of Groningen ii, 4, 38, 86
VIV	vortex-induced vibrations viii, 7, 8, 12, 56

Glossary

ASML	ASML is a Dutch company and a leading manufacturer of photolithography equipment used in the semiconductor manufacturing industry. ii, 1–4, 10, 12, 35, 38, 44, 47
BMBD	Bioinspired MEMS and Biomedical Devices is a research group within the Faculry of Science and Engineering of the University of Groningen ix, 46
BMF	Boston Micro Fabrication is the world leader in advanced additive manufacturing solutions based on Projection Micro Stereolithography. ix, 46
CMME	Computational Mechanical and Materials Engineering is a research group within the Faculry of Science and Engineering of the University of Groningen 4, 5
NASA	NASA is the United States government agency responsible for the nation's civilian space program and for aeronautics and aerospace research. 13
STL	An STL file is a widely used mesh file format in computer-aided design and 3D printing. 38
TSMC	TSMC is a prominent Taiwanese semiconductor manufacturing company and the world's largest independent foundry. 1

Nomenclature

Physics Constants

Symbol	Description	Definition
g	Gravitational acceleration	$9.8067\ ms^{-}2$

Greek Symbols

Symbol	Description	Unit
α	Unit cell size	m
β	Forcheimer coefficient	m^{-1}
δ_{ij}	The Kronecker delta	$-$
ϵ	Dissipation rate of turbulent kinetic energy	m^2s^{-3}
γ	The eigenvalues of a system of ordinary differential equations	$-$
κ	Turbulent kinetic energy	m^2s^{-2}
μ	Dynamic viscosity	Pas
∇	The gradient operator	m^{-1}
ν	Kinematic viscosity	m^2s^{-1}
ω	The specific dissipation rate	$m^2(s^{-}3)$
$\vec{\omega}$	Vorticity	s^{-1}
ϕ	Porosity	$-$
ρ	Density	kgm^{-3}
σ_{ij}	Cauchy's stress tensor	Pa
τ_{ij}	Shear stress tensor	Pa

Roman Symbols

Symbol	Description	Unit
A	Cross-sectional area	m^2

C_F	Dimensionless Forcheimer coefficient or inertial drag factor	$-$
D	Pipe diameter	m
D_o	Orifice/narrow section diameter	m
D_p	Pore size	m
D_{rel}	Relative density of triply periodic minimal surfaces (TPMS) $(1-\phi)$	$-$
$\boldsymbol{f}$	Field of body forces	ms^{-2}
F	Force	N
f	Friction factor	$-$
h_L	Head loss	m
K	Permeability	m^2
k_{ij}	Second order permeability tensor	m^2
$\boldsymbol{n}$	Unit vector normal to surface	$-$
p	Pressure	Pa
r	Radius of curvature	m
$R_{squared}$	Coefficient of determination	$-$
Re	Reynolds number $(\rho v D/\mu)$	$-$
t	Time	s
U_i	Mean component of velocity in direction x_1	ms^-1
V	Volume	m^3
v	Velocity	ms^{-1}
x_i	Position in the i-th direction	m

Chapter 1

Introduction and Research Context

1.1 Introduction

For the entirety of modern history, humans have used systems to convey fluids. The first record of such a system is the system of aqueducts used by the ancient Romans in order to provide them with water to drink and bathe in. In modern times, fluid transportation systems are used for the transport of gas, water, oil and other fluids in a wide range of industrial applications and at several orders of magnitude in terms of size.

While fluid transportation systems may generally seem simple, proper design of these systems needs to take many factors in consideration. Many failures of fluid transport systems are caused by fatigue loading due to excessive vibrations [1]. The excessive vibrations at the root of failures can originate from several factors. The phenomenon known as flow induced vibrations (FIV) are a type of vibration that originate from the flow of a gas or liquid and their interaction with their environment, both in internal flows and external flows.

A famous case where FIV resulted in a catastrophic failure is the collapse of the Tacoma Narrows Bridge in Washington State, USA in 1940. In this case, the interaction of the wind with the bridge resulted in significant oscillations. These oscillations already surfaced during the construction of the bridge. Several measures were taken to reduce the amplitude of the oscillations. However, these attempts were futile, and the bridge eventually collapsed. In the 1940's, engineers did not have access to the advanced modeling and analysis tools that are available nowadays. If the Tacoma Narrows Bridge were to be built today, there is a high likelihood that the mistakes made in the design of the bridge would have been caught well before the start of construction.

One of these advanced tools with widespread applications is computational fluid dynamics (CFD). In CFD, a computer is used to model and analyze fluid dynamic systems, a discipline in the broader field of mechanics that is concerned with the behaviour of liquids and gasses in motion. The field of fluid dynamics is an integral part of a vast range of physical phenomena, from blood flow in the human body to the formation of planets and stars. Likewise, many engineered systems are also directly or indirectly influenced by fluid dynamics. For each and every one of these systems in which fluid dynamics are present, there is a vast range of possibilities in terms of flow characteristics.

This project focuses on the reduction of FIV in cooling systems for high-tech industrial applications. While this project is performed in close collaboration with ASML, the lessons learned can be applied in a broader range of high-tech industrial applications.

1.2 Cooling Systems in High Precision Industry at ASML

ASML is a global industry leader in the manufacturing of photolithographic system for the production of semiconductors. The equipment that ASML manufactures is a crucial part of the global semiconductor supply chain, and ASML collaborates closely with major semiconductor manufacturers such as Intel, Samsung and TSMC. ASML invests heavily in research and development to advance lithography technology in order to maintain their position as an industry leader. ASML's current generation of extreme ultraviolet (EUV) lithography machines are able to produce semiconductors with feature sizes in the order of magnitude of nanometers. Because of the incredible precision with which ASML's EUV lithography machines are able operate, every small perturbation that is introduced into the system can have detrimental effects on the production yield. ASML's machines operate in a highly controlled environment in order to prevent perturbations to the system. Some of the considerations that have to be made to ensure industry leading levels of product quality include:

- The lithography machines operate in a cleanroom environment to minimize particle contamination of the system.
- The temperature of the system is tightly controlled, as fluctuations in temperature can have detrimental effect on the alignment of various components.
- Humidity is tightly controlled to prevent detrimental effects on delicate components.
- The lithography machines and the cleanrooms are isolated from external vibrations.
- The quality of input materials such as gasses, chemicals, EUV source material and silicon wafers is held to a very high standard in order to prevent detrimental effects that fluctuations in quality would have on the process.

Tight temperature control of the EUV systems requires thermal management. Firstly, because the some parts of the process produce a significant amount of thermal energy, and in general, to isolate the process from fluctuations in environmental conditions. In order to achieve this, EUV systems utilize an active fluid cooling system. In general, industrial cooling systems commonly contain both rigid sections as well as sections of flexible tubes. The combination of rigid and flexible sections can cause fluid resonances as demonstrated in the research by Kottapalli et al. [2]. In addition to these fluid resonances, significant vibrations can also be produced by cooling systems because of turbulent fluid flow. The interaction of the fluid with the geometry of the cooling system, with elements such as suddenly expanding or narrowing sections, baffle plates and orifices, and furcations and valves, can also generate vibrations. In most industrial applications, small vibrations are a negligible because they do not significantly influence the quality of the produced products. In the case of ASML, however, because the lithography process requires nanometer precision, small vibrations can have severely detrimental effects on the production quality and the subsequent production yield of the lithography process.

1.2.1 System Description

In short, ASML's NXE EUV system is used to transfer a desired pattern on a silicon wafer. This is achieved by focusing a beam of EUV light with a wavelength of 13.5 nm through a system of mirrors and lenses through a photomask, also know as a reticle. This reticle contains the desired pattern that is to be transferred to a silicon die. In order to achieve this with a high production yield, a large number of systems and sub-systems need to function optimally.

While the complex engineered system that is ASML's NXE EUV lithography systems poses an interesting object of research from many angles, this research project focuses on the cooling systems that are used in the NXE EUV systems. These cooling systems are characterized by:

- Flexible tube sections as well as stainless steel sections with a typical internal diameter of $10.2\ mm$.
- Distilled water at room temperature, $22\ ^{\circ}C$, is used as a coolant.
- Reynolds numbers for the fluid flow in the cooling systems ranging from $10,000$ to $20,000$.
- Fluid velocity ranging from $1\ m/s$ to $2\ m/s$.
- The frequency of the vibrations of interest ranging from $1\ Hz$ to $1\ kHz$.

Several other characteristics of the cooling system can be derived from the engineering requirements stated above:

- The dynamic viscosity μ of the fluid is $9.54 \cdot 10^{-4}\ Pa \cdot s$
- The density ρ of the fluid is $997.8\ kg/m^3$

The relevance of these engineering requirements is extensively covered in Chapter 3.

Industrial cooling systems typically involve changes in geometry. Some geometries that are of interest to ASML include 90°elbows, mitered elbows, smooth elbows, orifices, sudden expansions and sudden contractions which are schematically presented in Figure 1.1.

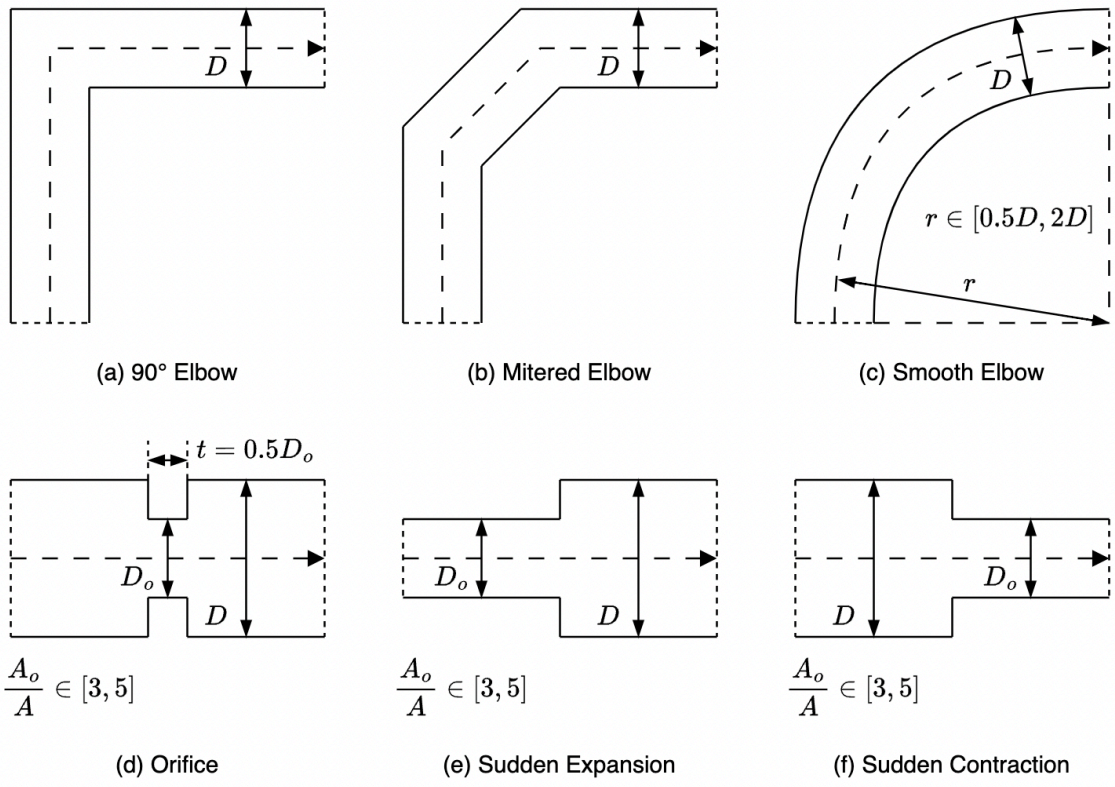

Figure 1.1: Schematic overview of (a) a 90° elbow, (b) a mitered elbow, (c) a smooth elbow, (d) an orifice, (e), a sudden expansion and (f) a sudden contraction.

Where D is the diameter of the primary section of pipe, and D_o is the diameter of the orifice, or the smaller section of pipe. A and A_o represent the cross-sectional area resultant from D and D_o respectively. As indicated in Figure 1.1 (c) the radius r for a smooth elbow typically ranges from 0.5 D to 2 D. In Figure 1.1 (d), the thickness t of the orifice plate is typically 0.5 D_o. For Figure 1.1 (d), (e) and (f), the ratio of area A_o to A typically ranges from 3 to 5.

1.3 Computational Mechanical and Materials Engineering Research Group

In addition to the collaborative effort with ASML, this research project is carried out under in the CMME research group at the University of Groningen (UG). The CMME is focused on engineering and modeling system across scales, from metamaterials up to integrated energy technologies to predict and optimize the performance of materials, components and systems.

Metamaterials are artificial materials that are engineered to have certain properties. Metamaterials are designed at micro or even nano-scale and their structure is tailored to achieve specific electromagnetic, acoustic, thermal, mechanical and fluid dynamical properties. Metamaterials exhibit unique behaviors that are not commonly observed in nature. For example, metamaterials can be engineered to have a negative Poisson's ratio (auxetic behaviour) or very high stiffness and low density. The direction of this research project and its proposed solutions is steered by this focus of the CMME research group.

1.4 Research Objective

Research into FIV is already a well established field, which has mostly focused on the petrochemical industry, the aerospace industry and civil engineering industry. In oil and gas transportation systems, high volumes of fluids have to be transported through thousands of kilometers of pipes. In these transport processes, extra care has to be taken to assure that such systems are able to perform optimally for their projected lifespan. In the aerospace industry, modeling of lift generating surfaces and designing them such that the frequency of vibrations generated are not the same as resonance frequencies of the structure. As for the civil engineering industry, one of the applications of FIV research is to prevent accidents like the catastrophic failure of the Tacoma Narrows Bridge. In high-tech fabrication applications such as EUV lithography, FIV can be detrimental to production performance because of the introduction of vibrations into a system which requires nanometer precision.

The primary objective of this research project is to develop a methodology to reduce FIV in high-tech cooling applications by developing methods to promote laminarization of turbulent flows. In order to effectively develop such a methodology, potential strategies are identified from literature. These strategies are evaluated on their ability to laminarize turbulent flows. From this literary basis, a potential solution is modeled, analyzed, and experimentally validated.

1.4.1 Research Questions

The formulation of clear and well-defined research questions is fundamental to the success of any thesis, providing a guiding framework for investigation and analysis. In the context of studying FIV

in internal pipe flows in high-tech industrial applications at ASML and in the context of the CMME research group at the UG, the following research questions are proposed:

1. What are the key phenomena contributing to FIV in internal flows?
   (a) How do parameters such as flow velocity, hydrostatic pressure and characteristic dimensions affect the presence of FIV?
   (b) How do fluid properties such as dynamic viscosity and fluid density affect the presence of FIV?
   (c) How do changes in the internal pipe geometry affect FIV?
   (d) Can the application of specific flow control strategies effectively reduce or eliminate undesirable FIV in internal pipe systems?
2. How can metamaterials concepts, one of the core competences of the CMME research group, be leveraged in order to reduce FIV?
   (a) What are metamaterials?
   (b) What are the inherent properties of metamaterials that make them suitable for high-tech industrial applications?

Chapter 2

Literature Review

The objective of this chapter is to review the state-of-the art of FIV in high-tech industrial cooling systems. This starts with an introduction to FIV and its respective relevant mechanisms in Section 2.1. Knowledge of the origination mechanism of FIV is of paramount importance when trying to mitigate these vibrations. The mechanisms that are potentially relevant in this research are discussed, and subsequently, several commonly proposed solution to reduce FIV are introduced in Section 2.2. These sections contribute to addressing the initial research question and its corresponding sub-questions. Finally, a class of metamaterials known as TPMS is introduced in Section 2.3.

2.1 Flow Induced Vibrations

Research into FIV, particularly in the context of internal flows, is centered around studying the vibrations which are generated by the interaction of the fluid and the structures that the fluid flows through. The field of FIV has become more important in recent years due to the progression of technological development of intricate manufacturing methods e.g. nuclear power plants, aerospace and the semiconductor industry. Research into FIV has started relatively recently. The first book on flow induced vibrations was written by Blevins [3]. Blevins [3] classified FIV into steady flow induced and unsteady flow related [4]. Subsequent research into many niche cases of FIV has drastically increased the knowledge on the phenomena that lie at the root of FIV.

For this work, the main form of FIV of interest are vibrations that arise in steady-state turbulent internal flows. Nakamura et al. [4] developed a classification system for common causes of FIV as shown in Figure 2.1. By identifying the root causes of FIV, a strategy to mitigate these vibrations can be developed. The main goal of this strategy is to prevent structural damage, equipment failure, or as most relevant for this research, performance degradation.

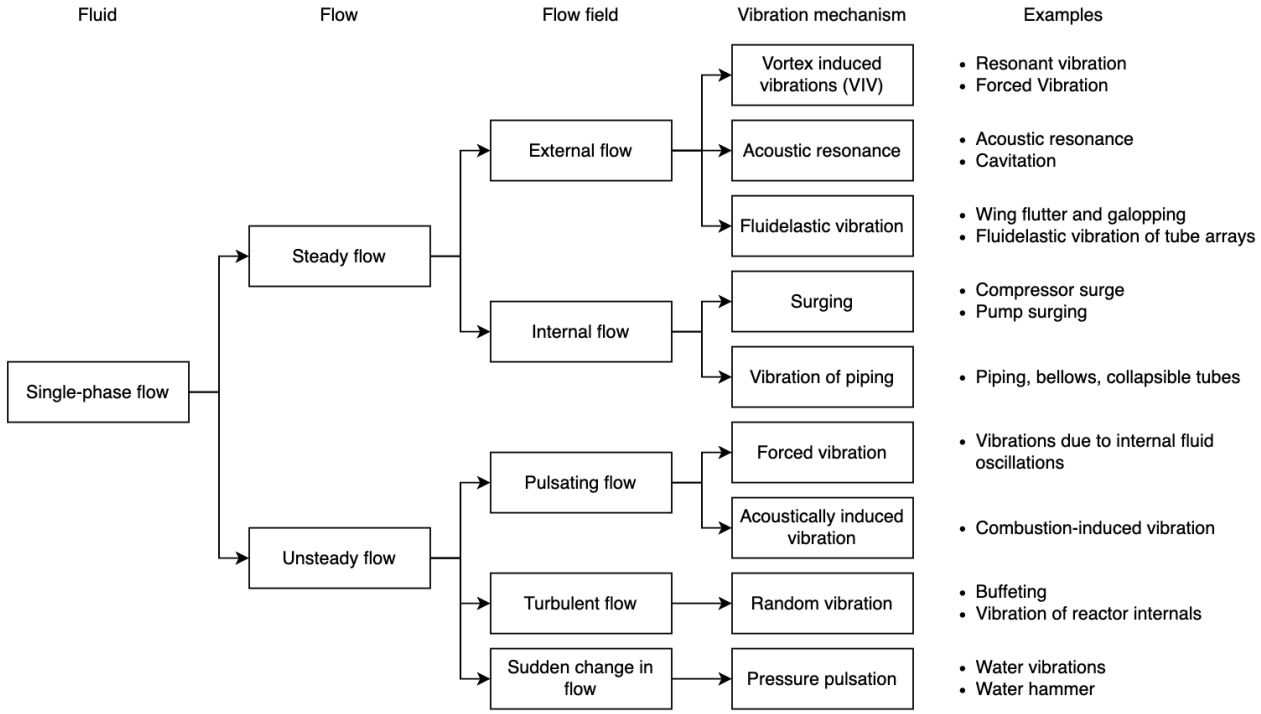

Figure 2.1: Flowchart of classifications of FIV based on Nakamura et al. [4].

The flowchart for the classification of FIV as developed by Nakamura et al. [4], was adapted to fit this research. Because this project is focused on single phase flows, the section on two phase is irrelevant, and therefore excluded. For this research, the relevant FIV mechanisms are possibly resultant from a combination of vortex-induced vibrations (VIV) caused by geometry changes, fluidelastic vibrations and random vibration resultant from turbulent flow.

VIV is a phenomenon characterized by the presence of a wake produced by obstacles or geometric irregularities. In certain cases, the wake behind the object can shed vortices. When the shedding of vortices becomes periodic, this can lead to periodic forces on the object. When the frequency of these periodic forces coincide with resonance frequencies of the system, this can lead to catastrophic failures. A classical example of VIV is fluid flow around a cylinder as shown in Figure 2.2a, however, in internal flows, changes in geometry such as elbows, sudden expansions and orifices can also cause significant VIV caused by recirculating flow as illustrated in Figure 2.2b.

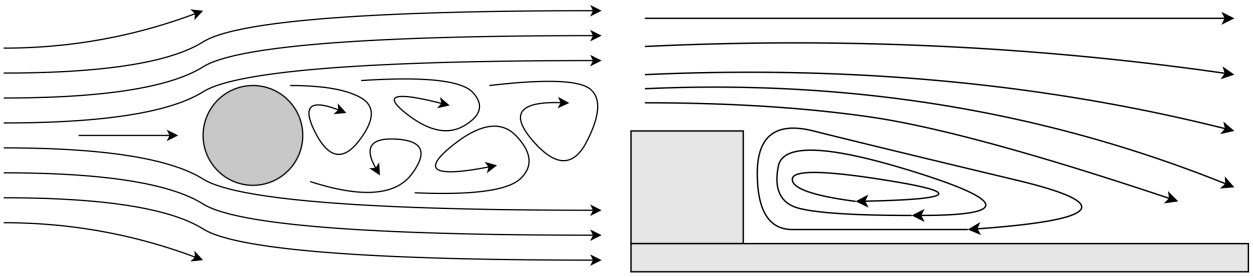

(a) Flow around cylinder (b) Flow through expansion

Figure 2.2: Schematic overview the flow path in (a) open channel flow around a cylinder and (b) recirculating flow after an expansion in internal flows which can cause the presence of VIV.

Fluidelastic vibrations arise from the interaction between fluid flow and the structure, leading to dynamic deformations. This phenomenon is often pronounced in flexible structures such as polymer tubing experiencing fluid forces. While fluidelastic vibrations are more pronounced when flexible materials are used for flow containment, because all materials have a finite stiffness, these kinds of vibrations can also occur in flow through stiff materials under the right conditions.

Random vibrations are caused by the irregular and chaotic motion of turbulent flows which excite vibrations in the nearby structures. Turbulent flow introduces random fluctuations in fluid velocity and pressure, contributing to non-periodic vibrations in the piping system. These random vibrations can have significant implications for fatigue life and structural integrity. And in high-tech applications,

2.2 Mitigation of Flow Induced Vibrations

A variety of solutions have been proposed for the mitigation of FIV. These mitigation strategies generally target one of the FIV mechanisms described in Section 2.1. Focusing on the mitigation of the detrimental effects of FIV caused by turbulent flow, several active and passive methods have been proposed. These methods generally attempt to reduce the turbulent kinetic energy by laminarizing the flow. In addition to these types of mitigation strategies, several proposed solution to mitigate VIV are reviewed. Where possible, the feasibility of implementation and the efficiency of of such solutions is discussed.

2.2.1 Active Control Methods

Active control methods use some sort of an actively controlled actuation system to reduce FIV. Most implementations of active control system require active sensing of flow conditions and the subsequent use of a feedback control loop to dynamically alter the flow. The main advantage of active control system is real-time adaptability to varying flow conditions. However, active control methods generally require complex sensing, control and actuation systems which limits its applicability in engineered system.

Pipe Wall Movement

Scarselli et al. [5], were able to successfully laminarize fluid flows by means of wall motion. Using this wall motion, the researchers significantly alterered the velocity profile of the flow, resulting

in laminar flow. The experiment consisted of a movable Perspex pipe which was slipped over two stationary stainless steel pipes. A schematic overview of the experimental setup is shown in Figure 2.3.

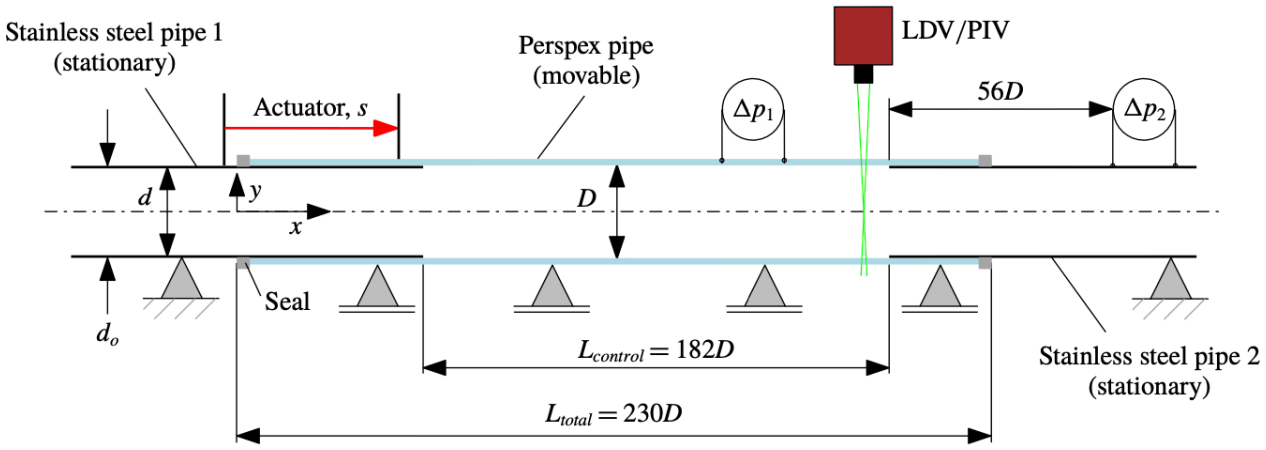

Figure 2.3: Schematic overview of the experimental setup used by Scarselli et al. [5].

For lower Reynolds numbers at around 5000, the researchers were able to laminarize flows with arbitrary wall velocities for a certain period of time. For larger Reynolds numbers, however, pipe wall velocities close to the bulk fluid velocities were required to laminarize the flow. Because of the linearly proportional relationship between the required pipe wall velocity and the bulk fluid velocity, the practical applicability of such active flow control methods is limited.

Annular Fluid Injection

Annular fluid injection is an active flow control method which involves the controlled introduction of a secondary fluid flow in in the annular space surrounding the primary pipe flow. The interaction between the injected secondary flow and the primary flow aims to disrupt the formation of turbulent spots, and thereby reduce the presence of turbulent flow structures responsible for FIV. Kühnen et al. [6], succeeded in fully laminarizing turbulent fluid flows by employing an actively controlled annular fluid injection system at Reynolds number up to 6000.

Plasma Actuators

Plasma actuators are devices employing high voltage, high-frequency discharges to create localized ionized air. This innovative technology, extensively discussed by Kotsonis [7] and Corke et al. [8], offers an approach to manipulating fluid dynamics. Plasma actuators operate on the principle of dielectric barrier discharge (DBD). When a high-voltage potential is applied across a dielectric barrier, it creates an electric field that ionizes the surrounding air or gas. The resulting plasma, composed of ions and electrons, interacts with the fluid flow, inducing localized changes in conductivity and creating a dynamic force that influences the fluid's behavior. However, it's worth noting that plasma actuators are primarily deployed in dry and semi-dry applications, finding practical utility in scenarios such as the flow conditioning of airflow over airplane wings. This actuation method is inherently unsuitable for the control of fluid flow because of its dependence on the ionization of air or gas.

Fluidic Oscillators

Fluidic oscillators are devices that harness fluid dynamics principles to generate controlled oscillatory fluid jets without the need for traditional mechanical components. These devices rely on the inherent instability of fluid flows and the interaction of fluidic elements to produce pulsatile or oscillatory outputs. One of the most common current applications of fluidic oscillators is as nozzles for windshield washers because of their ability to produce a wider time averaged distribution of mass than conventional nozzle designs [9]. Actively controlled injection of fluid using fluidic oscillators can significantly alter the flow characteristics because of the disruptive effect these fluid injections have on the formation of turbulent eddies.

There exist several other interesting active control systems which aim to achieve laminarization of turbulent flows, for this research however, the focus lies on passive methods. In ASML's NXE EUV systems, there is a limited amount of physical space, and implementation of active control systems adds an additional degree of complexity to the problem. For those reasons, the focus of this research lies on the implementation of passive solutions.

2.2.2 Passive Control Methods

Passive control methods do not use active monitoring of flow condition. This makes passive control methods less versatile and adaptable, however, it drastically reduces the complexity of the FIV mitigation strategy.

Custom Flow Channel Design

With the convergence of several technologies in recent years, procedurally generated custom flow channels have become a feasible solution to optimize fluid flows. Li et al. [10] were able to drastically reduce turbulent vorticity by iteratively generating an optimized fluid path as shown in Figure 2.4.

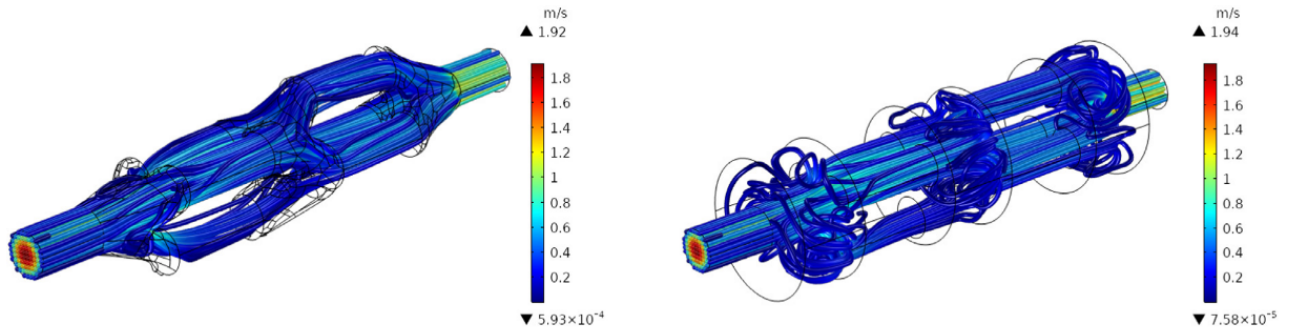

Figure 2.4: Velocity streamline profile of (left) the iteratively optimized fluid path and (right) the non-optimized fluid path [10].

Because of the advent of additive manufacturing and generative artificial intelligence (AI), design of custom flow channels has become feasible in more and more engineering applications. Multiple engineering software packages that are used in industry are able to generatively design an optimized fluid flow path, as well as optimized structural components. The goal of these optimizations is typically to reduce pressure drop over the length of the system, thereby improving efficiency, and in many

cases this also reduces FIV. As these fluid flow paths are typically generated using AI, a vast solution space can be investigated. Using traditional design methods, exploring this solutions space would be impractical. This methods thus allows for the generations of designs that might not have been considered by human engineers. Additionally, this generative methods allows for the optimization of several flow parameters e.g. the minimization of pressure drop while maximizing heat transfer.

Passive Flow Control Devices

Passive flow control devices include vortex generators, fins, spoilers, strakes, flow straighteners and specially designed inserts. In wind tunnels, honeycomb flow straighteners are often used Honeycomb to address irregularities and turbulence in fluid flows. These honeycomb structures counteract the swirling and and uneven velocity profile associated with turbulent flows in addition to their ability to dissipate turbulent kinetic energy. Kühnen et al. [6] were able to laminarize turbulent flows up to a Reynolds number of 10000 by employing a flow straightener with a honeycomb-like geometry.

Altering of Pipe Wall Surface

In nature, animals such as sharks, dolphins and penguins have evolved to have a skin or fur which reduces their friction during swimming. While, this gives these animals an advantage when it comes to hunting their prey, one could imagine the benefits one could obtain when these principles could be applied to e.g. producing more efficient freight ships or increasing the efficiency of pipe flow in industrial applications.

Nordell [11] tried to mimic the natural friction reducing effects of owl wings, which they use to fly silently. Using a channel with walls covered in a hair-like material, the researcher was able to laminarize turbulent airflow through a channel at $Re > 100,000$.

In a review by Golovin et al. [12] of so called super hydrophobic surfaces (SHS), the researchers found that, especially in the laminar flow regimes, SHS were able to produce significant decreases in drag. These SHS work by trapping small air bubbles in their surface texture. Turbulent flow, however, adds many challenges to the use of SHS for drag reduction. Secondary flow structures, such as eddies and vortices, that are present in turbulent flows potentially interact with the SHS, mitigating any drag reducing effects. The pressure fluctuations in turbulent flows can also promote wetting of the SHS, removing the entrapped air bubbles and thereby mitigating the drag reducing effect. Golovin et al. [12] found that researchers had had varying degrees of success while experimenting with various types of wall treatments to reduce frictional drag with SHS in the turbulent flow regime. While these types of solutions are promising, because of the unpredictable nature of these solutions, as well as poor manufacturability on industrial scales, the practical applications of bio-inspired SHS are still limited.

In addition to engineered wall surfaces, some solutions exist in the form of super hydrophobic wall coating. In an experiment carried out by Rios-Rodriquez et al. [13], a significant reduction in wall friction was observed. In the experiment set up by the researchers, they were able to achieve a 20 % reduction in pressure drop and an increase in measured slip velocity when compared to non-coated wall surfaces.

Porous Insert to Prevent Circulating Flows

Chan and Lien [14] looked into the dynamics of fluid flow through a porous medium. Flow through porous media typically modeled using Darcy's law, a linear relation between permeability and

pressure differential over a porous element. In cases where the linear relationship does not hold, the flow is said to be non-Darcian, and conversely, if the linear relationship holds, the flow is characterized as Darcian flow.

Chan and Lien [14] found that porous inserts in turbulent pipe flow were able to decrease turbulent kinetic energy κ after a sudden expansion in the flow drastically. The researchers found that lowering the permeability K, or decreasing the value of the Darcy number of the porous material generally reduced and eliminated turbulent recirculation as demonstrated in Figure 2.5.

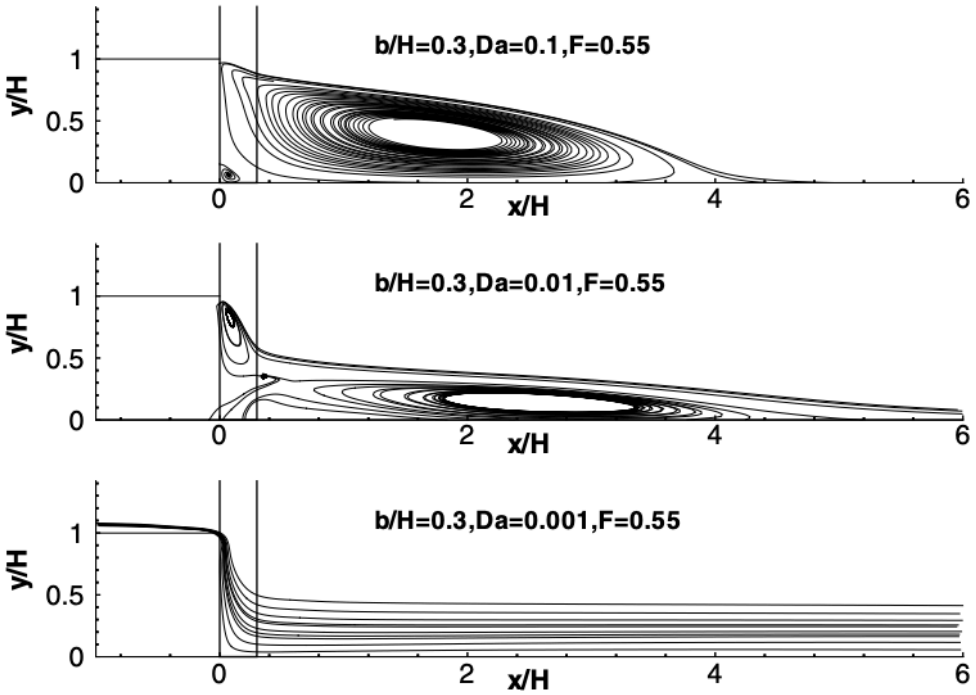

Figure 2.5: Sensitivity of flow field to changes in Darcy number [14].

This phenomenon inspired an avenue towards reducing VIV resultant from sudden expansions in the industrial cooling systems used in ASML's NXE EUV lithography systems while leveraging metamaterials concepts. Section 2.3 outlines a mathematical concept known as TPMS. TPMS are an interesting class of mathematical surfaces with periodicity in three dimensions. Metamaterials based on these mathematical principles possess excellent mechanical properties and great manufacturability using additive manufacturing techniques. When choosing a unit cell which is sufficiently small, the behaviour of fluid flow through a TPMS is analogous flow through a foam-like porous medium as described by Chan and Lien [14]

2.3 Triply Periodic Minimal Surfaces

Triply periodic minimal surfaces (TPMS) occur in nature, and more recently have become increasingly attractive in engineering applications [15]. Using conventional subtractive manufacturing methods, most TPMS are impossible to manufacture due to their complex internal structures. In recent

years, manufacturing of TPMS has become feasible because of the rise of various additive manufacturing methods.

2.3.1 Mathematical Definition of TPMS

A surface is said to be minimal if the surface $S \subset \mathbb{R}^3$ has zero mean curvature at any point [16]. The mean curvature, H, is given by

$$H = \frac{k_1 + k_2}{2}, \tag{2.1}$$

where k_1 and k_2 are the principal curvatures [17]. When that minimal surface lacks self-interactions, i.e. the edges of the surface do not cross one another, the minimal surface is said to be embedded. If an embedded minimal surface is periodic in three independent directions such that the pattern is infinitely repeatable, the surface is said to be a TPMS.

Some of the most commonly used TPMS used in engineering applications are the Schwarz Primitive (SP) and the Schwarz Diamond (SD) developed by Herman Schwarz in the 19th century and the Schoen Gyroid (SG), the Schoen I-Graph and Wrapped Package (IW-P) and the Schoen F-Rhombic Dodecahedron (F-RD) developed by Alan Schoen while working at the NASA in the 20th century [15, 18, 19]. The mathematical expression of these common TPMS are given in Table 2.1.

Table 2.1: Five commonly used TPMS, their abbreviations and mathematical expressions.

Name	**Symbol**	**Expression**
The Schwar Primitive	SP	$f(x,y,z) = cos(x) + cos(y) + cos(z) = C$
The Schwarz Diamond	SD	$f(x,y,z) = sin(x)sin(y)sin(z) + sin(x)cos(y)cos(z)$ $+ cos(x)sin(y)cos(z) + cos(x)cos(y)sin(z) = C$
The Schoen Gyroid	SG	$f(x,y,z) = cos(x)sin(y) + cos(y)sin(z)$ $+ cos(z)sin(x) = C$
The Schoen I-Graph and Wrapped Package	IW-P	$f(x,y,z) = 2\,(cos(x)cos(y) + cos(y)cos(z) + cos(z)cos(x))$ $-\ (cos(x) + cos(y) + cos(z)) = C$
The Schoen F-Rhombic Dodecahedron	F-RD	$f(x,y,z) = 4cos(x)cos(y)cos(z) - (cos(2x)cos(2y)$ $+ cos(2y)cos(2z) + cos(2z)cos(x)) = C$

From these TPMS, two approaches can be taken to create a metamaterial. The first approach considers the volume that is bound by the TPMS to be a solid. This approach is henceforth referred to as the solid-wise TPMS. The second approach considers two surfaces which are offset from the TPMS along its respective normal direction, resulting in two surfaces, in between which the volume is filled. The second approach is henceforth referred to as the sheet-wise TPMS. In Figure 2.6, the five common TPMS are shown. In Appendix C, Figure C.1 and Figure C.2 show the unit cells of the TPMS in the solid-wise and sheet-wise lattices respectively. In Figure C.3 and Figure C.4, for each of the discussed TPMS a lattice is constructed consisting of nine unit cells to illustrate the periodic nature of TPMS. These TPMS are generated using MSLattice, a highly configurable software package to generate TPMS meshes [20].

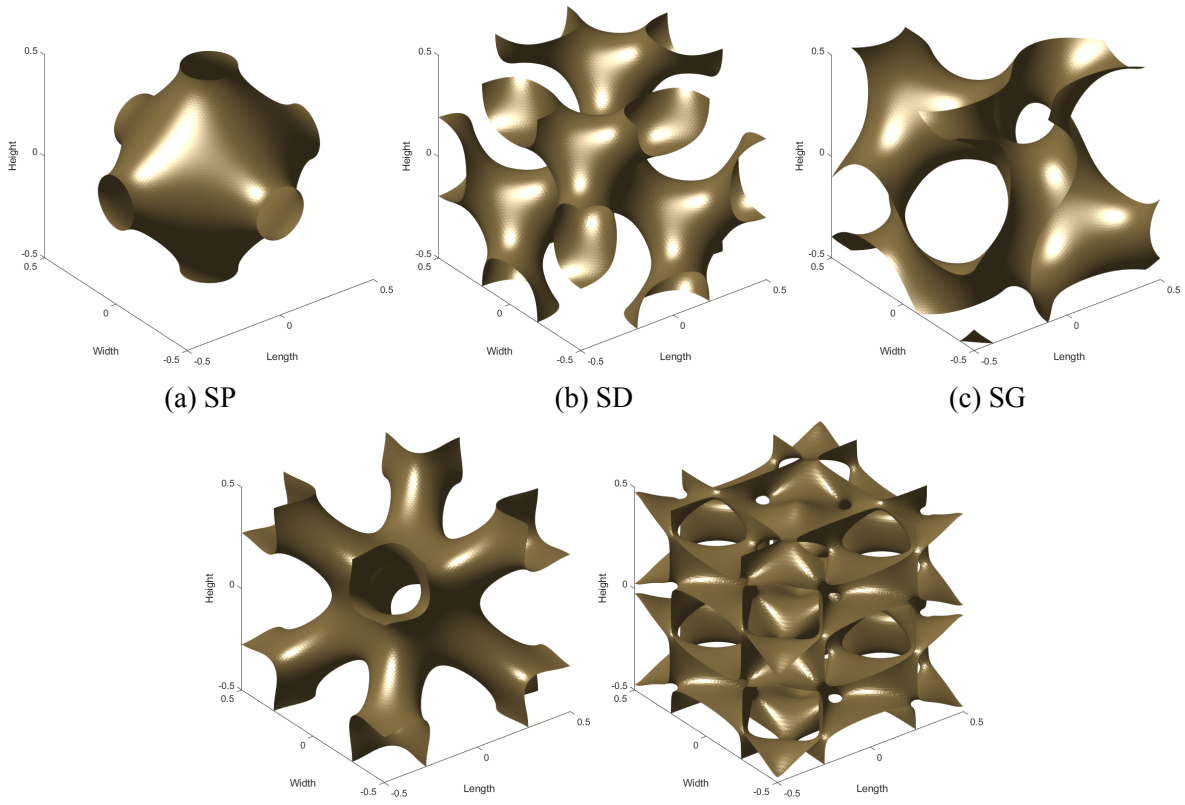

(a) SP (b) SD (c) SG

(d) IW-P (e) F-RD

Figure 2.6: Unit cells of five commonly used TPMS.

2.3.2 Applications of TPMS

TPMS are known to have a high stiffness-to-weight ratio, heat dissipation control and enhanced mechanical energy absorption and are commonly referred to as metamaterials, because their physical properties stem from both their base material as well as their geometry [15]. TPMS structures have become increasingly popular in biomedical engineering applications with the onset of additive manufacturing [19], as TPMS structures mimic the topography of trabecular bone structures. When using TPMS as a scaffold in the process of bone regeneration, it promotes many cellular processes, as well as being mechanically strong enough to promote bone regeneration [21–23].

Additionally, in mechanical engineering applications, the excellent mechanical properties of TPMS can be leveraged to produce strong parts with highly configurable mechanical properties. One such applications is the use of TPMS lattices as infill patterns for additive manufacturing. In the early days of additive manufacturing, the infill patterns which are used to fill volumes inside 3D printed parts were relatively simple. In the last few years, however, many popular 3D printing slicer software packages such as Ultimaker Cura and PrusaSlicer have added TPMS lattices as infill patterns. In interpenetrating phase composites (IPC), a class of advanced composite materials characterized by the simultaneous presence of two or more interwoven networks or phases within a single structure, TPMS are excellent candidates for IPC's because the required properties co-continuousness and connectedness are inherent to the definition of TPMS. In IPC, TPMS can be leveraged to produce metamaterials with excellent mechanical properties [15].

TPMS lattices have also been found to be excellent candidates in applications with fluid-solid

interactions. TPMS lattices have already found use in reverse osmosis and ultrafiltration processes, and TPMS lattices are regarded as highly efficient geometries for heat exchangers because of their large surface area to volume ratio [24, 25].

A continuation of the review of TPMS follows in Section 3.6 after some prerequisite concepts have been introduced in Chapter 3.

Chapter 3

Background

The objective of this chapter is to outline basic concepts which govern the field of fluid dynamics for internal flows and flow through porous media. This starts with the Continuity equation in Section 3.1, followed by the derivation of the Navier-Stokes equations based on the work of Munson et al. [26], Irgens [27] and Shelley et al. [28] in Section 3.2. Thereafter, the dimensionless quantity known as the Reynolds number and the different flow regimes are defined in Section 3.3 based on the work of Landau and Lifshitz [29] and Shelley et al. [28]. In Section 3.4, several concepts that are inherent to the behaviour of internal turbulent flows are laid out. In Section 3.5, an overview of CFD is presented along with typical CFD workflows and several turbulent flow modeling approaches Finally, Darcy's law and the Darcy-Forcheimer equation are explained in Section 3.7. These principles are the basis on which this research is built, and are prerequisites to understanding the reasoning in subsequent chapters.

3.1 The Continuity Equation

The basic concepts that are a prerequisite to the derivation of the Navier-Stokes equations are: the material derivative, the Cauchy stress tensor and the continuity equation. The explanation on these subjects is based on the work of Munson et al. [26] and Irgens [27]. The explanation on the material derivative and the Cauchy stress tensor are given in Appendix A.1 and Appendix A.2 respectively, whereas the explanation of the continuity equation is given below.

The continuity equation is better known as the principle of conservation of mass. Consider an arbitrary volume V where surface S represents the surface enclosing volume V. The continuity equation simply states that for the principle of conservation of mass to hold, the flux of mass through the surface S, must be equal to the rate of change of the mass in volume V [27] such that

$$\frac{\partial}{\partial t}\int_V \rho(x,t)dV = -\int_s \rho(x,t)\boldsymbol{v}\cdot\boldsymbol{n}dS, \tag{3.1}$$

where $\rho(x,t)$ is the density of the fluid as a function of time and position and $\boldsymbol{v}\cdot\boldsymbol{n}$ is the flow velocity multiplied with the unit vector normal to the surface S. Using the divergence theorem as in Appendix A.1 this becomes

$$\int_V \frac{\partial \rho(x,t)}{\partial t} dV = -\int_V \nabla \cdot (\rho(x,t)\boldsymbol{v}) dV. \tag{3.2}$$

Such that

$$\int_V \frac{\partial \rho(x,t)}{\partial t} + \nabla \cdot (\rho(x,t)\boldsymbol{v}) dV = 0. \tag{3.3}$$

In order for the principle of conservation of mass to hold, this must be true for any volume V, such that

$$\frac{\partial \rho(x,t)}{\partial t} + \nabla \cdot (\rho(x,t)\boldsymbol{v}) = 0. \tag{3.4}$$

Finally, for the case of an incompressible fluid, the density $\rho(x,t)$ is a constant

$$\frac{\partial \rho(x,t)}{\partial t} = 0. \tag{3.5}$$

Such that

$$\nabla \cdot \boldsymbol{v} = 0. \tag{3.6}$$

3.2 The Navier-Stokes equations

The Navier-Stokes equations were progressively developed in the 19th century by French engineer and physicist Claude-Lois Navier and Irish physicist and mathematician George Gabriel Stokes, and is the governing equation for the motion of any fluid. The derivation of the Navier-Stokes equations is based on Newton's second law, which states that the net force acting upon an object is equal to the object's mass multiplied with its acceleration. Following Newton's second law, consider a small element of fluid with volume V and density ρ,

$$F = \rho V \frac{D\boldsymbol{v}}{Dt}, \tag{3.7}$$

where the acceleration of the fluid volume is the material derivative as in Equation A.5. In order to determine the forces acting upon a fluid, we use Cauchy's stress tensor σ_{ij}, as in Equation A.11, to express the force acting on the fluid as a result of stress. George Gabriel Stokes developed a method in which Cauchy's stress tensor is split up in a so called volumetric stress tensor and a stress deviator tensor,

$$\sigma_{ij} = \sigma_{volumetric} + \sigma_{deviator}$$

$$\begin{bmatrix} \sigma_{11} & \sigma_{12} & \sigma_{13} \\ \sigma_{21} & \sigma_{22} & \sigma_{23} \\ \sigma_{31} & \sigma_{32} & \sigma_{33} \end{bmatrix} = -\begin{bmatrix} p & 0 & 0 \\ 0 & p & 0 \\ 0 & 0 & p \end{bmatrix} + \begin{bmatrix} \tau_{11} & \tau_{12} & \tau_{13} \\ \tau_{21} & \tau_{22} & \tau_{23} \\ \tau_{31} & \tau_{32} & \tau_{33} \end{bmatrix} \tag{3.8}$$

$$\sigma_{ij} = -p\delta_{ij} + \tau_{ij}, \tag{3.9}$$

where the volumetric stress tensor $\sigma_{volumetric}$ represents the pressure p that is exerted on the fluid by the surrounding environment, and the stress deviator tensor $\sigma_{deviator}$ represent the shear stresses τ_{ij} that act upon the fluid. For a Newtonian fluid, a fluid in which the viscous stress acting upon it is linearly proportional to the strain rate, the shear stress is

$$\tau_{ij} = \mu \left(\frac{\partial v_j}{\partial x_i} + \frac{\partial v_i}{\partial x_j} \right), \tag{3.10}$$

where μ is the dynamic viscosity of the fluid volume and v and x are the velocity and position in an arbitrary coordinate system. Substituting this in Equation 3.9 results in:

$$\sigma_{ij} = -p\partial_{ij} + \mu \left(\frac{\partial v_j}{\partial x_i} + \frac{\partial v_i}{\partial x_j} \right). \tag{3.11}$$

We can now combine the stress tensor with Equation A.11 to obtain the force acting on the fluid in the *i* direction

$$F_i = V \left(-\frac{\partial p}{\partial x_i} + \mu \frac{\partial}{\partial x_j} \left(\frac{\partial v_j}{\partial x_i} + \frac{\partial v_i}{\partial x_j} \right) \right), \tag{3.12}$$

which can be simplified to

$$F_i = V \left(-\frac{\partial p}{\partial x_i} + \mu \frac{\partial}{\partial x_i} \left(\frac{\partial v_j}{\partial x_j} \right) + \mu \frac{\partial^2 v_i}{\partial x_j^2} \right). \tag{3.13}$$

Subsequently, summing over *i* to arrive at the total stress,

$$F_{stress} = V \left(-\nabla p + \mu \nabla \left(\nabla \cdot \boldsymbol{v} \right) + \mu \nabla^2 \boldsymbol{v} \right). \tag{3.14}$$

Using the divergence theorem, and the fact that the divergence is zero for incompressible fluids as in Equation 3.6 we can set $(\nabla \cdot \boldsymbol{v}) = 0$ such that

$$F_{stress} = V \left(-\nabla p + \mu \nabla^2 \boldsymbol{v} \right). \tag{3.15}$$

In addition to the stress forces, a fluid can also experience body forces such as gravitational forces or magnetic forces. A general expression of the body forces acting upon the fluid is given by

$$F_{body} = \int \rho \boldsymbol{f} dV, \tag{3.16}$$

where $\boldsymbol{f}$ is the field contributing to their respective body force. Under the assumption that the body force is constant over the entire volume, the body force simplifies to

$$F_{body} = \rho \boldsymbol{f} V. \tag{3.17}$$

In the case that a fluid is experiencing multiple body forces, these can simply be calculated separately and subsequently summed. Now that all the components of the force acting upon the fluid are known, Equation 3.7, Equation 3.15 and can be combined such that

$$\rho \frac{D\boldsymbol{v}}{Dt} = \left(-\nabla p + \mu \nabla^2 \boldsymbol{v}\right) + \rho \boldsymbol{f}. \tag{3.18}$$

Next, the material derivative from Equation A.5 is used to obtain the Navier-Stokes equations in matrix form

$$\rho \left(\frac{\partial \boldsymbol{v}}{\partial t} + (\boldsymbol{v} \cdot \nabla) \boldsymbol{v} \right) = -\nabla p + \mu \nabla^2 \boldsymbol{v} + \rho \boldsymbol{f}. \tag{3.19}$$

Under the assumption that there are no body forces acting upon the fluid, the Navier-Stokes equations, using $\boldsymbol{v} = \begin{bmatrix} u & v & w \end{bmatrix}$ and $x_1 = x$, $x_2 = y$ and $x_3 = z$, are

$$\begin{aligned}
\rho \left(\frac{\partial u}{\partial t} + u\frac{\partial u}{\partial x} + v\frac{\partial u}{\partial y} + w\frac{\partial u}{\partial z} \right) &= -\frac{\partial p}{\partial x} + \rho g_x + \mu \left(\frac{\partial^2 u}{\partial x^2} + \frac{\partial^2 u}{\partial y^2} + \frac{\partial^2 u}{\partial z^2} \right) \\
\rho \left(\frac{\partial v}{\partial t} + u\frac{\partial v}{\partial x} + v\frac{\partial v}{\partial y} + w\frac{\partial v}{\partial z} \right) &= -\frac{\partial p}{\partial y} + \rho g_y + \mu \left(\frac{\partial^2 v}{\partial x^2} + \frac{\partial^2 v}{\partial y^2} + \frac{\partial^2 v}{\partial z^2} \right) \\
\rho \left(\frac{\partial w}{\partial t} + u\frac{\partial w}{\partial x} + v\frac{\partial w}{\partial y} + w\frac{\partial w}{\partial z} \right) &= -\frac{\partial p}{\partial z} + \rho g_z + \mu \left(\frac{\partial^2 w}{\partial x^2} + \frac{\partial^2 w}{\partial y^2} + \frac{\partial^2 w}{\partial z^2} \right).
\end{aligned} \tag{3.20}$$

3.3 Flow Regimes

3.3.1 The Reynolds Number

The Reynolds number is a dimensionless quantity which is useful for classifying the general behaviour of a fluid. The concept of the Reynolds number was developed by George Gabriel Stokes, but the quantity was named after Osborne Reynolds, who popularized the quantity in the field of fluid mechanics in the late 19th century. The Reynolds number is used in a wide range of applications, ranging from the flow of air over an aircraft wing to the flow fluids through piping systems. The Reynolds number can be derived from the Navier-Stokes equations in Equation 3.19 by converting it to a dimensionless form as shown in Appendix B. The general definition of the Reynolds number is:

$$Re = \frac{\mu U L}{\rho}, \tag{3.21}$$

where μ is the dynamic viscosity; U is the characteristic velocity, which, for internal flows is the mean fluid velocity v; L is the characteristic length, which for internal flows in cylindrical tubes is the tube diameter D, and ρ is the fluid density. Such that the Reynolds number for internal flows is:

$$Re = \frac{\mu v D}{\rho}. \tag{3.22}$$

The Reynolds number is often used to distinguish between flow regimes in engineering applications and represents the ratio between inertial and viscous forces. As the Reynolds number goes to zero, the viscous term in the Navier-Stokes equations becomes the dominant driver of fluid behaviour. As the Reynolds number goes to infinity, the inertial forces become the dominant driver of fluid behaviour. The dominance of viscous forces generally results in laminar, or plate-like flow, while the dominance of inertial forces generally results in turbulent flow behaviour.

3.3.2 Stokes Flow

Laminar flow typically occurs at $Re < 2040$ for internal flows [30]. A special case of laminar flow is is when $Re \ll 1$. In this case the inertial component of the Navier-Stokes equations tends to zero

$$0 \approx \left(-\nabla p + \mu \nabla^2 \boldsymbol{v}\right) + \rho \boldsymbol{f}. \tag{3.23}$$

This special case of laminar flow is known as Stokes flow. In this case, the non-linear and time dependent terms in the Navier-Stokes equations are dropped. In practical terms, this means that in Stokes flow, a reversing of the forces is equivalent to a reversion of time. Some nice examples of this phenomenon can be found in literature, such as research by Fonda and Sreenivasan [31], in which the time-reversible nature of Stokes flow is demonstrated by shining a laser point at a photochromic viscous fluid, whereafter the fluid is mixed by rotating a plastic cylinder in the middle of the system. Subsequently, the fluid is ”unmixed” by reversing the rotation of the plastic cylinder as shown in Figure 3.1.

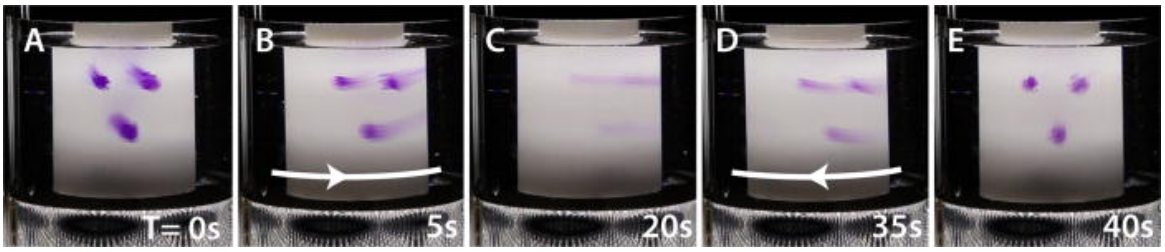

Figure 3.1: A demonstration of the reversibility of Stokes flow. In (A) the photochromic material is activated using a laser, in (B), the fluid starts rotating, (C) shows the mixed state, in (D), the fluid starts counter-rotating and (E) shows the return of the fluid to its original state [31].

3.3.3 Laminar and Turbulent Flow Regime

In other scenarios, the inertial term in the Navier-Stokes equations cannot be disregarded, and therefore flow in the laminar regime is generally not time-independent. The distinction between laminar flow and turbulent flow lies in the ability of the flow to return to its original state after a small perturbation. Setting the velocity v and pressure p of the flow equal to

$$\boldsymbol{v} = \boldsymbol{v}_s + \boldsymbol{v}_p \qquad\qquad p = p_s + p_p, \tag{3.24}$$

where $\boldsymbol{v}_s$ and p_s represent the steady state solutions to the Navier-Stokes equations and $\boldsymbol{v}_p$ and p_p represent small perturbations to this state. Substitution into the Navier-Stokes equations, under the assumption that there are no body forces present, results in

$$\rho\left(\frac{\partial\left(\boldsymbol{v}_s+\boldsymbol{v}_p\right)}{\partial t}+\left(\left(\boldsymbol{v}_s+\boldsymbol{v}_p\right)\cdot\nabla\right)\left(\boldsymbol{v}_s+\boldsymbol{v}_p\right)\right)=-\nabla\left(p_s+p_p\right)+\mu\nabla^2\left(\boldsymbol{v}_s+\boldsymbol{v}_p\right), \tag{3.25}$$

or, in the expanded form

$$\rho\left(\frac{\partial\boldsymbol{v}_s}{\partial t}+\frac{\partial\boldsymbol{v}_p}{\partial t}+\left(\boldsymbol{v}_s\cdot\nabla\right)\boldsymbol{v}_s+\left(\boldsymbol{v}_s\cdot\nabla\right)\boldsymbol{v}_p+\left(\boldsymbol{v}_p\cdot\nabla\right)\boldsymbol{v}_s+\left(\boldsymbol{v}_p\cdot\nabla\right)\boldsymbol{v}_p\right)= \\ -\nabla p_s-\nabla p_p+\mu\left(\nabla^2\boldsymbol{v}_s+\nabla^2\boldsymbol{v}_p\right). \tag{3.26}$$

Omitting the higher order terms in $\boldsymbol{c}_p$ and p_p results in

$$\rho\left(\frac{\partial\boldsymbol{v}_p}{\partial t}+\left(\boldsymbol{v}_s\cdot\nabla\right)\boldsymbol{v}_p+\left(\boldsymbol{v}_p\cdot\nabla\right)\boldsymbol{v}_s\right)=-\nabla p_p+\mu\nabla^2\boldsymbol{v}_p. \tag{3.27}$$

Considering the continuity equation in Equation 3.6,

$$\nabla\cdot\boldsymbol{v}_p=0. \tag{3.28}$$

Because this is a system of ordinary differential equations, the solution can be decomposed. The solution is a sum of expressions where $\boldsymbol{v}_p$ depends on time t in $e^{-i\gamma t}$, where γ are the eigenvalues of the system of ordinary differential equations. If the $Im[\gamma]$ is positive, the solution increases with time. In terms of the system behaviour this means that once perturbations are introduced into the system, they continue to propagate and grow. This is characteristic for turbulent flow. If $Im[\gamma]$ is negative, the magnitude of the perturbation decreases exponentially with time, in other words, the flow returns to its steady state once the perturbations are removed. This is known as laminar flow. The mathematical analysis required for the investigation of these principles is extremely complex, and is yet to be solved. Because of this, research into laminar and turbulent flows and the transition between the two is based on experimental data.

Avila et al. [30] have developed a method, that allows the characterization of conditions, mechanisms, and control strategies related to the transition from laminar to turbulent flows. The researchers proposed that turbulent flows mainly originate from transient turbulent spots in laminar flows, and that these provide a pathway for transition to fully turbulent flow. By comparing the mean time of decay of turbulence in these localized turbulent zones with the mean time of proliferation of turbulence in these zones, the researchers proposed that as the mean time of decay becomes smaller than the mean time of proliferation, the transition to fully turbulent flow occurs. The point at which the mean time of decay intersects with the mean time of proliferation was found to lie at $Re\approx 2040$ as shown in Figure 3.2. At this critical Reynolds number, the spatial interaction was found to be simple, because of the clear separation of the turbulent spots. At $Re>2400$ however, the researchers found that dynamics of the fluid become increasingly complicated, because of the merging of turbulent spots. From this

point onward, this is referred to as turbulent flow, characterized by the existence of turbulent eddies on several geometrical orders of magnitude.

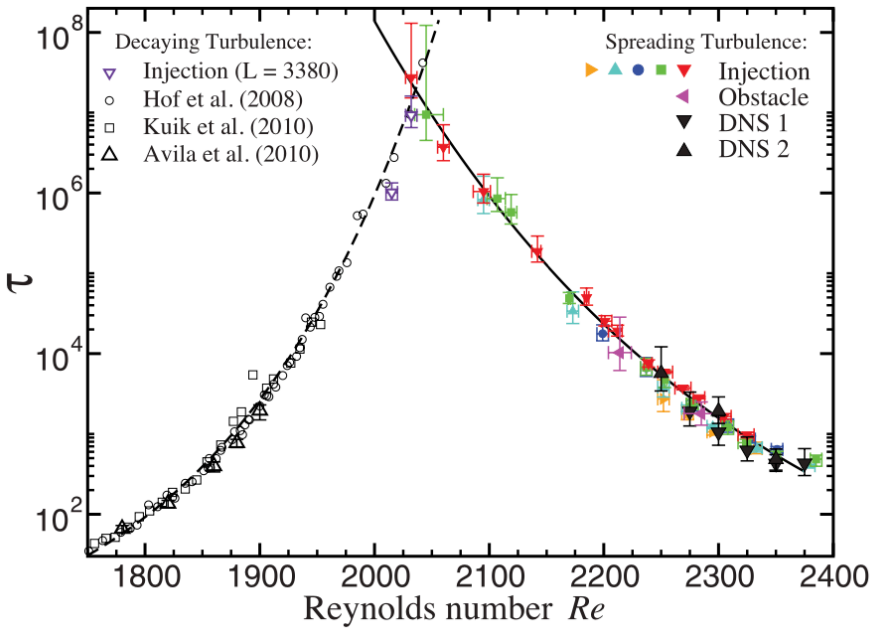

Figure 3.2: Mean lifetime of a puff before decaying or splitting [30].

For curved geometries such as spiral shaped pipes, the Reynolds number at which the transition to the turbulent flow regime occurs is larger than that for straight internal flows. This is attributed to the strong secondary flows that are present in such flows [32]. Because of the complex three-dimensional nature of these fluid dynamics problems, this field of research is largely unexplored.

A schematic overview of laminar versus turbulent flows is shown in Figure 3.3. For turbulent flows, because the turbulent eddies form as an amplification of perturbations, a seemingly infinitely small difference in initial conditions can have massive implications for the state of the system at any subsequent point in time. This produces problems when trying to predict the exact behaviour of the fluid. Fortunately, however, this is rarely necessary for engineering applications, and while turbulent flows are chaotic, when the flow properties are time-averaged the behaviour of the fluid becomes more predictable.

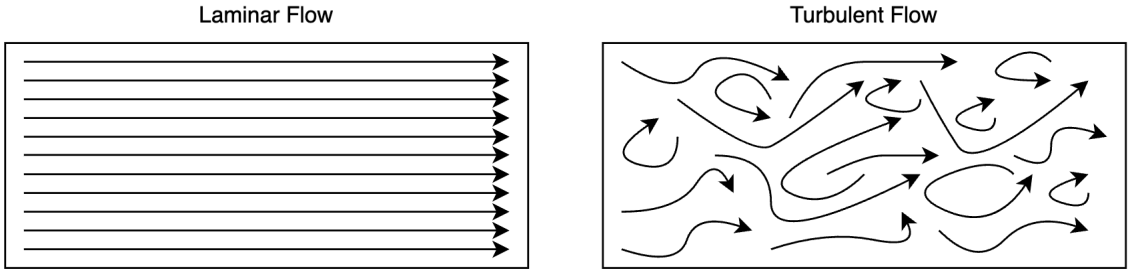

Figure 3.3: A schematic overview of the laminar and turbulent flow regimes.

In an engineering context, there are several advantages and disadvantages to the laminar and turbulent flow regime as shown in Table 3.1. It is important to note that the characteristic flow regime of many engineering systems is often a consequence of other engineering requirements. And as such, in some cases, it is important to negate the negative effects of the flow regime as much as possible.

Table 3.1: The advantages and disadvantages of the laminar and turbulent flow regime.

	Advantages	**Disadvantages**
Laminar Flow	The behaviour of laminar flow, e.g. heat transfer, velocity profile, is predictable because of the sheet-like flow. Laminar flow typically has reduced friction losses. In laminar flow, mixing of the fluid is minimal. Laminar flow generally causes a lower amount of FIV.	Limited amount of mixing, which can be disadvantageous in chemical processes Reduced efficiency of heat transfer Lower mass transfer rates, limited by fluid velocity to remain below $Re = 2040$.
Turbulent Flow	Efficient mixing, because of the turbulent eddies at several orders of magnitude in terms of size. Enhanced efficiency of heat transfer, for a similar reason. Increased mass transfer rate, as not limited by Reynolds number.	The behaviour of turbulent flows is less predictable than laminar flows, due to its chaotic nature, making it more difficult to model, analyze and control. Increased Energy Consumption: Turbulent flow experiences higher frictional losses, requiring more energy to maintain flow rates in pipelines and conduits. FIV are higher in turbulent flows, which may be detrimental to system performance. Erosion and wear are increased because of high shear forces associated with turbulent flow. Turbulent flow often exhibits pressure fluctuations, which can damage their respective systems.

3.4 Internal Flows

Internal flow refers to the movement of fluid within enclosed physical boundaries, such as pipes, tubes, ducts, or channels. In the context of fluid dynamics, internal flow is distinguished from external flow, where the fluid moves over the surface of an object. The important principles that characterize internal fluid flows are explained in the subsequent sections. This section is based on the work of Munson et al. [26].

3.4.1 Navier-Stokes equations for Turbulent Internal Flow

The Navier-Stokes equations of motion can be solved analytically only in a small number of simple fluid dynamics problems. For the case of turbulent three-dimensional internal flow of an incompressible fluid, the Navier-Stokes equations cannot be solved analytically. Subsequently, numerical approximation is necessary to solve the Navier-Stokes equations for such a system. The Navier-Stokes equations for turbulent internal flow is:

$$\begin{aligned}
\frac{\partial}{\partial x}(\overline{u}\cdot\overline{u})+\frac{\partial}{\partial y}(\overline{u}\cdot\overline{v})+\frac{\partial}{\partial z}(\overline{u}\cdot\overline{w}) &= -\frac{1}{\rho}\frac{\partial P}{\partial x}+\frac{\partial}{\partial y}\left(\nu\frac{\partial\overline{u}}{\partial y}\right)+\frac{\partial}{\partial z}\left(\nu\frac{\partial\overline{u}}{\partial z}\right)-\frac{\partial}{\partial y}\left(\overline{u'v'}\right)+R_x \\
\frac{\partial}{\partial x}(\overline{v}\cdot\overline{u})+\frac{\partial}{\partial y}(\overline{v}\cdot\overline{v})+\frac{\partial}{\partial z}(\overline{v}\cdot\overline{w}) &= -\frac{1}{\rho}\frac{\partial P}{\partial y}+\frac{\partial}{\partial y}\left(\nu\frac{\partial\overline{v}}{\partial y}\right)+\frac{\partial}{\partial z}\left(\nu\frac{\partial\overline{v}}{\partial z}\right)-\frac{\partial}{\partial x}\left(\overline{u'v'}\right)+R_y \\
\frac{\partial}{\partial x}(\overline{w}\cdot\overline{u})+\frac{\partial}{\partial y}(\overline{w}\cdot\overline{v})+\frac{\partial}{\partial z}(\overline{w}\cdot\overline{w}) &= -\frac{1}{\rho}\frac{\partial P}{\partial z}+\frac{\partial}{\partial y}\left(\nu\frac{\partial\overline{w}}{\partial y}\right)+\frac{\partial}{\partial z}\left(\nu\frac{\partial\overline{w}}{\partial z}\right)-\frac{\partial}{\partial x}\left(\overline{u'w'}\right)+R_z,
\end{aligned} \tag{3.29}$$

where ν is the kinematic viscosity, $(\overline{u})$, $(\overline{v})$ and $(\overline{w})$ are the mean velocity components, $(\overline{u'v'})$, $(\overline{u'w'})$ and $(\overline{v'w'})$ are the Reynolds stresses representing turbulent fluctuations and (R_x), (R_y), (R_z) are additional terms representing Reynolds stresses due to turbulence modeling. There are various approaches to modeling turbulence which are further expanded upon in Section 3.5.2.

3.4.2 Boundary Conditions

The standard boundary condition for fluid dynamical systems is the no-slip condition. The no-slip condition is a fundamental concept in fluid dynamics that describes the behavior of fluid molecules at a solid boundary. At the boundary, the fluid adheres to the wall due to frictional effects, resulting in a zero relative fluid velocity adjacent to the wall such that

$$v_{||rel} = 0. \tag{3.30}$$

For distances further from the wall, the relative parallel velocities increase with a gradient. This assumption generally holds true for both laminar and turbulent flows as demonstrated in Figure 3.4.

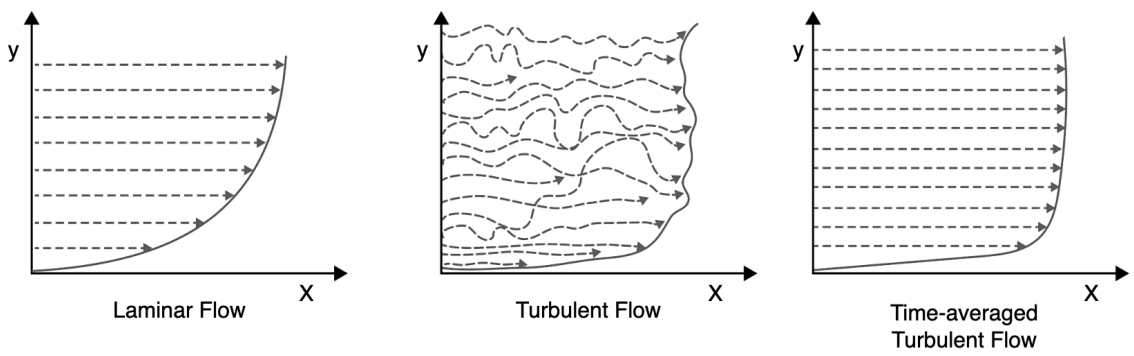

Figure 3.4: A schematic overview of the flow velocity profiles for laminar as well as turbulent pipe flows with the no-slip wall condition.

In some cases, it is more appropriate to assume some slip is present such that $u_{||rel} \neq 0$. In these cases, generally a slip velocity is defined as

$$v_s = b\frac{\partial v}{\partial n}, \tag{3.31}$$

where b is the slip length and $\frac{\partial v}{\partial n}$ is the velocity gradient normal to the surface of the wall. The slip length b is an artificial quantity, the length of which is determined by linear interpolation of the velocity profile such that the no-slip condition would be reached as shown in Figure 3.5.

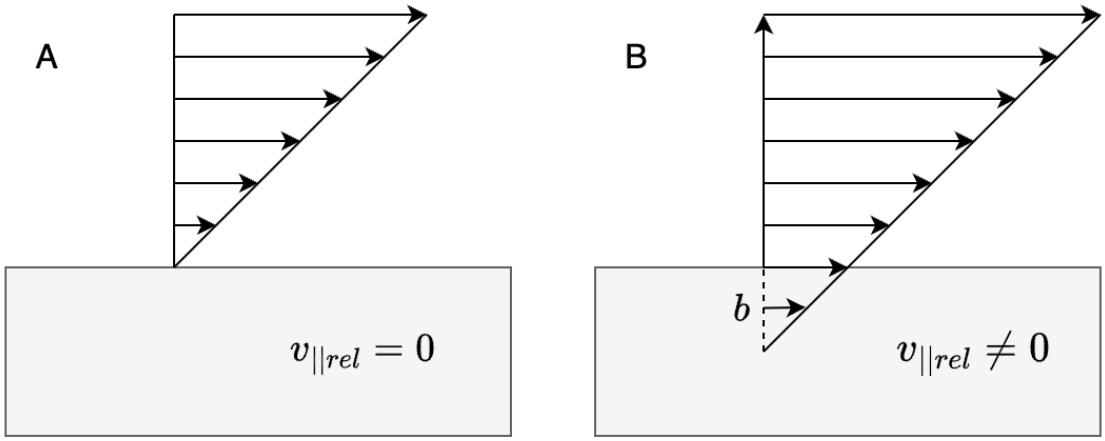

Figure 3.5: Schematic overview of (A) no-slip boundary conditions and (B) slip boundary conditions with the indication of slip length b.

Additionally, there is a range of circumstances in which no wall is present e.g. simulation of a motorcycle driving, a airplane flying or the spinning of wind turbines. However, one must still define a domain for the simulation. In these conditions it is appropriate to discard the non-slip condition and to choose a domain which is sufficiently large in order to prevent the interaction of the object of interest with the wall.

Finally, a periodic flow condition is a method to simulate a virtually infinite periodic system. This is achieved by placing periodic flow conditions on the walls of a simulation domain. Under periodic flow conditions, the flow that exits the system on one side, re-enters the system on on the other side of the domain, parallel to the side where it exited.

3.4.3 Flow Development

Because of the boundary conditions in internal flows, the velocity profile of the fluid changes along the length of a domain when a uniformly distributed flow is introduced. This characteristic development of the velocity profile schematically shown in Figure 3.6.

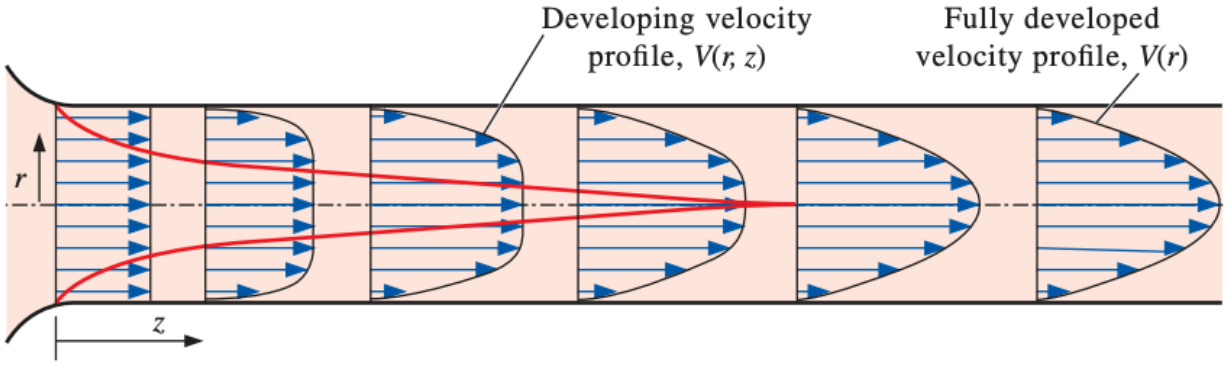

Figure 3.6: Development of the velocity profile in a circular pipe [33].

Flow development in circular pipes is dependent on the length L traveled axially along the flow path expressed in terms of flow diameter D. In fully developed flow, velocity profile of the flow becomes independent of the axial position. The axial length required for the flow to develop fully is known as the entrance length. For laminar flows, the entrance length as defined by Bergman et al. [34] is:

$$L_{h,laminar} = 0.0575 Re_D D. \tag{3.32}$$

For turbulent flows, the entrance length as defined by Çengel and Cimbala [33] is:

$$L_{h,turbulent} = 1.359 D (Re_D)^{\frac{1}{4}}. \tag{3.33}$$

It is important to account for the development of flow when simulating internal flow problems. By setting the incoming flow velocity profile as fully developed, engineers are able to analyze a section of pipe without the need to model a significant length of pipe for the flow to fully develop. This generally makes the analysis computationally less expensive and simpler.

3.4.4 Losses in Internal Flows

Internal fluid flows are characterized by pressure drop and head loss. Pressure drop refers to the decrease in pressure as the fluid flows along the pipe, tube, channel etc., and head loss refers to the energy dissipation in internal flows due to factors such as friction and changes in geometry [26]. These concepts essentially describe the same phenomenon with different units. Their relationship is given by the hydrostatic pressure formula $\Delta P = \rho g \Delta h$, where the difference in height Δh is interchangeable with head loss h_L. These losses are generally categorized as major losses, which are the losses attributed to the wall shear stresses τ_w between the fluid and the pipe wall, and minor losses, which are attributed to changes in geometry such as elbows, expansions, contractions, and valves.

Major Losses

For major losses, the head loss is defined as:

$$h_{L\ major} = f\frac{l}{D}\frac{v^2}{2g}, \tag{3.34}$$

where f is a dimensionless friction factor, l is the length of the pipe, D is the pipe diameter, v is the mean fluid velocity and g is the gravitational acceleration. This equation is also known as the Darcy-Weisbach equation. Subsequently, the Darcy-Weisbach equation can be rewritten in pressure drop per unit length form:

$$\Delta p_{major} = f\frac{\rho l}{D}\frac{v^2}{2}. \tag{3.35}$$

For fully developed laminar flow, the friction factor f is simply inversely proportional to the Reynolds number Re of the flow such that:

$$f_{lam} = \frac{64}{Re}. \tag{3.36}$$

For turbulent flows, however, the relation between the friction factor f and the Reynolds number Re is less straight forward because f is a function of the Reynolds number Re and the roughness of the pipe ϵ, i.e., $f = \phi\left(Re, \frac{\epsilon}{D}\right)$. This relation is rather complex, and has thus far not been successfully derived from theoretical analysis.

Minor Losses

For minor losses, or losses which are attributed to changes in pipe geometry, the head loss is defined as:

$$h_{L\ minor} = K_1\frac{v^2}{2g} + K_2\frac{v^2}{2g} + K_3\frac{v^2}{2g} \tag{3.37}$$

where K_1, K_2 and K_3 are dimensionless quantities known as loss coefficients. K_1 is for entrances and exits, K_2 is for bends and K_3 is for valves and other fittings. The loss coefficients are strongly dependent on the geometry of the components responsible for the head loss and the Reynolds number Re. Because of the relation between the loss coefficients and the geometry of its respective component, the loss coefficients are typically determined experimentally. Rewriting the equation in terms of pressure loss results in

$$\Delta P_{minor} = K_1\frac{\rho v^2}{2} + K_2\frac{\rho v^2}{2} + K_3\frac{\rho v^2}{2}. \tag{3.38}$$

Because sudden expansions are relatively common features in piping systems, the pressure drop in those cases can be generalized with the Borda-Carnot equation:

$$\Delta p = -\rho\frac{A_1}{A_2}\left(1 - \frac{A_1}{A_2}\right)v_1^2. \tag{3.39}$$

where, A_1 and A_2 are the crossectional area of the section, pre-expansion and post-expansion respectively.

3.5 Computational Fluid Dynamics

With the exception of fairly simple steady state problems, the Navier-Stokes equations is generally difficult to analytically solve due to their non-linear nature. For this reason, most problems in the field of fluid dynamics require numerical approximation of the solution. This requires a vast amount of computations, and while it is technically possible for humans to perform these computations, the advances made in digital computing since the 1950's have allowed researchers to offload these computations to digital computers. This field of research is known as computational fluid dynamics (CFD).

CFD is a field of research which focuses on numerically approximating the Navier-Stokes equations in a variety of fluid dynamics problems. The field of CFD is often expanded to solve multiphysics problems e.g. heat convection problems, fluid structure interactions and chemical reaction engineering, and can thus be a beneficial tool in many industries. When it comes to CFD there is an infinite amount of directions to approach a problem. The workflow however, in many cases is comprised of similar steps. The workflow in CFD typically involves:

1. Problem definition and geometry creation:
   (a) Clear definition of the problem to be solved. This means defining the domain, boundaries and objectives of the simulation.
   (b) Create a geometry in a computer aided design (CAD) software package and ensure that this geometry is suitable for CFD.
2. Mesh generation:
   (a) Generate a mesh that discretizes the geometry and is suitable for the simulation. Mesh quality has a significant influence on the accuracy of the simulation and is usually a trade-off between computational cost and desired accuracy.
3. Setup and model selection:
   (a) Choose an appropriate fluid model e.g. incompressible, compressible, turbulent or laminar.
   (b) Choose and set boundary conditions for the problem.
   (c) Specify initial conditions such as the initial velocity or temperature field.
   (d) Define material properties like density, viscosity and thermal conductivity.
   (e) Define whether the simulation is steady-state or transient based on the problem.
4. Software selection and setup:
   (a) Select a software package that is suitable for the relevant problem.
   (b) Configure the solver settings e.g. methods for time-stepping, convergence criteria.
5. Execution:
   (a) Start the simulations and monitor the convergence. In case of non-convergence, adapt settings as needed.
6. Post-processing and visualization:
   (a) Process the data resultant from the simulation in order to generate plots which are beneficial for the applications.

(b) Extract non-visualized performance metrics such as velocity, pressure, drag and lift.

In order to obtain results which closely represent reality, one must validate the results of CFD using experimental data or analytical solutions. Typically, some tweaks, such as refining or changing the mesh and adjustment of software settings, have to be applied iteratively until a satisfactory result is achieved.

3.5.1 Discretization of the Fluid Domain

Discretization of the fluid domain, or meshing, is an essential step in CFD simulation. Meshing divides up the fluid domain in discrete volumes, for each of which the Navier-Stokes equations is numerically approximated. For example, imagine a simple rectangular fluid domain. Considering non-compressible flow in Figure 3.7. For the case without temperature change, and subsequently no density change, the volumetric flow rate in Q_{in} is equal to the volumetric flow rate out Q_{out} due to Equation 3.1.

Figure 3.7: Schematic overview of a very simple rectangular fluid domain.

When the fluid domain in Figure 3.7 is subdivided into four smaller volumes as in Figure 3.8, the principles of continuity still hold for each of these individual volumes.

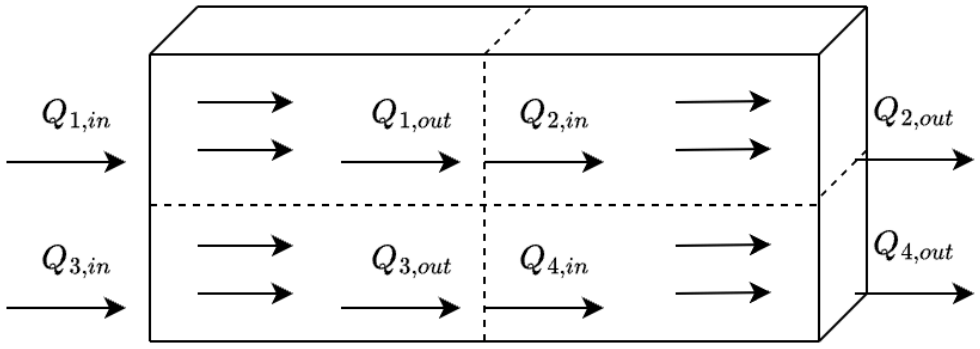

Figure 3.8: Schematic overview of a very simple rectangular fluid domain subdivided in four elements.

This simple example illustrates the principle upon which meshing is based. One aspect that becomes immediately apparent is that the second example in Figure 3.8 gives more information about how the fluid behaves inside the fluid domain. When such a domain is divided into millions of discrete volumes, the this method allows for approximating the behaviour of a continuous physical system. In practice, while more mesh elements, means a better approximation of the physical system, the number of mesh elements that is adequate for a CFD simulation is a trade-off between accuracy and computation time.

3.5.2 Turbulence Modeling

As described in Section 3.4.1, there are several approaches to model turbulent flows. In the Reynolds averaged Navier-Stokes (RANS) approach, the governing Navier-Stokes equations are time-averaged to separate the flow variables into mean and fluctuating components. This averaging process transforms the turbulent equations into a set of equations representing the time-averaged flow, resulting in a closed system that is computationally manageable.

Reynolds Averaged Navier-Stokes Approach

One of the most widely used RANS approaches is the $\kappa - \epsilon$ turbulence model, where additional transport equations are introduced for turbulent kinetic energy κ

$$\rho \frac{D\kappa}{Dt} = \frac{\partial}{\partial x_\kappa} \left[\frac{\mu_t}{\sigma_\kappa} \frac{\partial \kappa}{\partial x_\kappa} \right] + \mu_t \left(\frac{\partial U_i}{\partial x_\kappa} + \frac{\partial U_\kappa}{\partial x_i} \right) \frac{\partial U_i}{\partial x_\kappa} - \epsilon, \tag{3.40}$$

and the dissipation rate of turbulent kinetic energy ϵ

$$\rho \frac{D\epsilon}{Dt} = \frac{\partial}{\partial x_\kappa} \left[\frac{\mu_t}{\sigma_\epsilon} \frac{\partial \epsilon}{\partial x_\kappa} \right] + C_1 \mu_t \frac{\epsilon}{\kappa} \left(\frac{\partial U_i}{\partial x_\kappa} + \frac{\partial U_\kappa}{\partial x_i} \right) \frac{\partial U_i}{\partial x_\kappa} - C_2 \frac{\epsilon^2}{\kappa}, \tag{3.41}$$

where

$$\mu_t = \frac{C_\mu \rho \kappa^2}{\epsilon} \tag{3.42}$$

is the turbulent viscosity; U_i is the mean velocity component in direction x_i, and C_1, C_2, C_μ, σ_κ and σ_ϵ are model constants [35]. The RANS equations are subsequently closed by substituting the dynamic viscosity μ with the turbulent viscosity μ_t.

The $\kappa - \epsilon$ turbulence model is built upon certain assumptions, with a crucial one being the requirement for a sufficiently high Reynolds number. If the Reynolds number is too low, both κ and ϵ have a very small magnitude. Small changes in the flow field can subsequently cause relatively large fluctuation in κ and ϵ. The point at which the Reynolds number is too low is highly dependent on the nature of the simulation.

Another important assumption is that the turbulence within the boundary layers is in equilibrium, such that production equals dissipation. Because these assumptions may not hold universally, this limits the accuracy of the $\kappa - \epsilon$ turbulence model in some cases. Notably, the $\kappa - \epsilon$ turbulence model is known to perform poorly in situations with adverse pressure gradients, that is, there is a pressure gradient in the opposite direction of the fluid flow. In these cases, it can underestimate the spacial

extent of recirculation zones. Despite these limitations, however, the model's compromised accuracy is often deemed acceptable, given the considerable computational resource savings compared to more intricate turbulence models [36].

Another example of a RANS approach is the $\kappa - \omega$ turbulence model where κ, again, is the turbulent kinetic energy and ω is the dissipation per unit of turbulent kinetic energy, also commonly referred to as the specific dissipation rate. The $\kappa - \omega$ turbulence model has some distinct advantages over the $\kappa - \epsilon$ turbulence model. Specifically, it exhibits superior performance in flat plate flows wherein adverse or favorable pressure gradients are present. However, the $\kappa - \omega$ turbulence model also possesses two primary drawbacks. Firstly, the $\kappa-\omega$ model may be sensitive to the free stream inlet values of specific dissipation rate ω. Secondly, the $\kappa - \omega$ model is generally less resilient compared to the $\kappa - \epsilon$ model in terms of numerical robustness [36].

There exist several other RANS turbulence models with advantages and disadvantages but regardless of the specific choice of RANS turbulence model, the RANS approach is computationally efficient because it does not resolve the small scale turbulent structures. This can, however, diminish the accuracy of the model, but in most engineering applications, this approach provides an adequate degree of accuracy.

Large Eddy Simulation

The second approach to model turbulent flows is the Large eddy simulation (LES) approach. This approach works by directly simulating the behaviour of large eddies, while modeling the effects of smaller eddies. Unlike RANS modeling, the LES approach retains information about the large turbulent structures that are present in the system. This approach is especially suited for use cases where predictions are made for unsteady flow, but is computationally more expensive than the RANS approach.

Direct Numerical Modeling

The final approach to modeling of turbulent flows is the direct numerical simulation (DNS) approach. This approach is the most detailed and accurate representation of turbulent flows. The DNS approach directly solves the Navier-Stokes equations without employing any turbulence models. Because this requires the resolution of turbulence at all scales, even the smallest turbulent structures, a very fine mesh is required. This makes this approach the most computationally expensive and is therefore mostly limited to research use cases, where high-performance computing (HPC) clusters are used. It is, however, worth noting that advances in computational techniques, parallel computing and and improvements in algorithms may contribute to making DNS simulations more attainable in the future.

3.6 Fluid Flow Through TPMS

Research on the flow of fluid through TPMS is generally centered around biomedical applications. In these applications, fluid flows are characterized by low Reynolds numbers. At these low Reynolds numbers, flow is Darcian, i.e. there exists a linear relationship between fluid velocity and pressure drop. Jung and Torquato [16] were able to determine the fluid permeability of six TPMS in Stokes flow at a porosity $\phi = 0.5$. Because this numerical analysis is performed under Stokes flow conditions, its

outcome is of limited relevance for this research. Asbai-Ghoudan et al. [37] proposed an analytical model for the prediction of permeability of TPMS. By simulating several unit cells of five TPMS, at five levels of porosity and five unit cell sizes the researchers were able to produce an analytical model where the permeability K is a function of porosity ϕ and pore size D_p as in

$$K = C_0 \cdot D_p^2, \tag{3.43}$$

where C_0 is a dimensionless constant that describes the configuration of the flow path which itself is dependent on porosity ϕ and the shape of the TPMS. Because of the focus on biomedical engineering, the flow conditions for the reported experiment differ significantly from the relevant flow conditions for this research. The analytical model by Asbai-Ghoudan et al. [37] was exclusively tested at a fixed Reynolds number $Re = 1$. Rathore et al. [38] found that the validity of Darcian flow through TPMS only holds up until Reynolds number of around $Re = 20$. Beyond this value, the inertial drag factor C_F becomes sufficiently significant that the flow cannot be approximated by Darcy's law. From this point forward, the researchers proposed the use of the Darcy-Forcheimer equation to approximate the behaviour of the flow through the TPMS.

3.7 Darcy-Forcheimer Flow Through Porous Media

In many cases involving the modeling of flow through a porous medium it does not make practical sense to model the exact geometry of a problem one is working on. For instance, when modeling the flow of oil or gas through porous rock, or the flow of fluids through a filter, the exact geometry of the porous medium is irrelevant. Modeling of such a system would be computationally very expensive because of the required modeling of a large amount of detailed features. Instead, the more interesting aspect of such a model would be the macroscopic behaviour of such a system.

3.7.1 Darcy's Law

In the 19th century, the French engineer Henry Darcy proposed a law on the flow of fluids through a bulk porous medium. Darcy first established this law experimentally, since then however, Darcy's law has been derived from the Navier-Stokes equations under conditions of incompressible Stokes flow. Recall that under these conditions

$$\left(-\nabla p + \mu \nabla^2 \boldsymbol{v}\right) + \rho \boldsymbol{f} \approx 0. \tag{3.44}$$

Assuming the viscous resisting force is linearly proportional to the velocity of a fluid, and ignoring body forces, we can write

$$-\frac{1}{k_{ij}} \mu \phi v_j - \frac{\partial p}{\partial x_i} = 0, \tag{3.45}$$

where k_{ij} is the second order permeability tensor and ϕ is the porosity. Such that the velocity in the n direction is

$$\frac{k_{ni}}{k_{ij}} v_j = \sigma_{nj} v_j = v_n = -\frac{k_{ni}}{\phi \mu} \frac{\partial p}{\partial x_i}. \tag{3.46}$$

Subsequently, Darcy's law in the n direction is

$$v_n = -\frac{k_{ni}}{\mu}\frac{\partial p}{\partial x_i}. \tag{3.47}$$

In the case of an isotropic porous medium, the non-diagonal entries in k_{ij} are zero, and and the diagonal elements in k_{ij} are K. Using these assumptions, the common form of Darcy's law is

$$v = -\frac{K}{\mu}\nabla p/ \tag{3.48}$$

Darcy's law is also commonly written in the form

$$\nabla p = -\frac{\mu}{K}v. \tag{3.49}$$

In the case of flow through a porous element of length Δx, Darcy's law takes the form

$$\nabla p = \frac{\Delta p}{\Delta x} = -\frac{\mu}{K}v, \tag{3.50}$$

where Q is the volumetric flow rate and A is the cross-sectional area, such that $v = Q/A$ is the mean fluid velocity, and Δp is the pressure drop over the porous medium.

3.7.2 The Darcy-Forcheimer Equation

The flow regime for which this linear relationship between pressure drop and permeability holds is know as the Darcian flow regime. This flow regime, however, is only an accurate representation of reality in situations where the inertial forces in the Navier-Stokes equations are negligibly small. Experimental tests have shown that the Darcian flow regime, in general, extends to Reynolds numbers of around 10, although this tends to depend on multiple factors. The transition to non-Darcian flow, however, is a topic of active research [39]. In order to account for the non-linearity that exist in the relation between velocity and pressure drop above these Reynolds numbers, Philip Forcheimer proposed an amended version of Darcy's law, known as the Darcy-Forcheimer equation. The Darcy-Forcheimer equation is

$$\nabla p = \frac{\Delta p}{\Delta x} = -D\mu v - F\rho v^2, \tag{3.51}$$

where D and F are the Darcy contribution and the Forcheimer contribution respectively. Another common definition of the Darcy-Forcheimer equation is

$$\nabla p = \frac{\Delta p}{\Delta x} = -\frac{\mu}{K}v - \frac{C_F}{\sqrt{K}}\rho v^2, \tag{3.52}$$

where K and C_F are the permeability and the dimensionless Forcheimer coefficient respectively sometimes also referred to as the inertial drag factor, and

$$D = \frac{1}{K} \qquad F = \frac{C_F}{\sqrt{K}}. \tag{3.53}$$

In extreme cases where $v^2 \gg v$, the behaviour of the fluid through porous media can be described by

$$\nabla p = \frac{\Delta p}{\Delta x} = -\frac{C_F}{\sqrt{K}} \rho v^2. \tag{3.54}$$

Regardless of the form in which the Darcy-Forcheimer equation is written, the relevant coefficients are typically determined experimentally, both using physical experiments as well as using CFD simulations.

Chapter 4

Methods

In this chapter, the experiment design and methods used in this research project are extensively discussed. This starts with an exploration of CFD methods Section 4.1. Followed by the experiment design in Section 4.2, and the experimental validation in Section 4.3.

4.1 Exploring Computational Fluid Dynamics

A diverse range of CFD software options caters to research needs, spanning from open-source platforms like OpenFOAM to proprietary solutions such as COMSOL Multiphysics, Ansys Fluent, and Simstar STAR-CCM+. In the initial phases of CFD exploration, COMSOL Multiphysics was preferred for its versatility in conducting various simulations. This software facilitates CFD simulations using RANS, LES, and DNS solvers. It accommodates simulations in one, two, and three dimensions, including two-dimensional axisymmetric configurations. Additionally, the software supports both time-dependent and steady-state modes, offering flexibility for a comprehensive investigation into fluid dynamics phenomena.

For the initial exploration, several simple simulations were created. Starting with turbulent flow through a straight pipe with a uniform fluid velocity profile at the inlet. For the second round of simulations, a simple geometry with two 90 °elbows, a geometry with a sudden expansion, and a geometry with a sudden contraction were created. Because this research is focused on the cooling system that is used by ASML in their NXE EUV system, the flow parameters of the simulation must be relevant for the practical application. In the cooling systems used by ASML the typical internal pipe diameter is 10.2 mm (1/2 inch). The liquid that is used in the system is distilled water at a temperature of around 25 $^{\circ}C$. The Reynolds number in the cooling system lies in the range of 10,000 to 20,000. Subsequently, the presence of turbulent flow is highly likely, as the Reynolds number for all cases is significantly larger than 2040. For this reason, the initial simulations were all performed using the $\kappa - \epsilon$ RANS algorithm.

4.1.1 Simple turbulent flow through pipe

The first simple simulation consists of a straight pipe with an inner diameter of 10 mm and a length of 200 mm. This simulation was performed using COMSOL Multiphysics. The fluid velocity was set to 1.5 m/s such that, at room temperature, the Reynolds number of the flow was close to 15,000.

The model that was used is the $\kappa - \epsilon$ turbulence model because of its numerical robustness and low computational cost. Because the results of this initial simulation are not required to be an accurate representation of reality, for the initial simulations, the mesh is chosen to be quite extra course. The naming convention for mesh size in COMSOL Multiphysics is discussed in Section 4.2.

The streamline velocity plot and pressure differential plot resultant of the simulation are shown in Figure 4.1. The inlet velocity is uniformly distributed along the inlet surface. The flow velocity subsequently develops as the flow traverses along the length of the tube as shown in Figure 4.2. In subsequent simulations, these settings were undesirable as it requires the fluid to travel a significant distance through the tube before the flow is fully developed. Therefore, in subsequent simulations, the inlet velocity profile is set to fully developed flow.

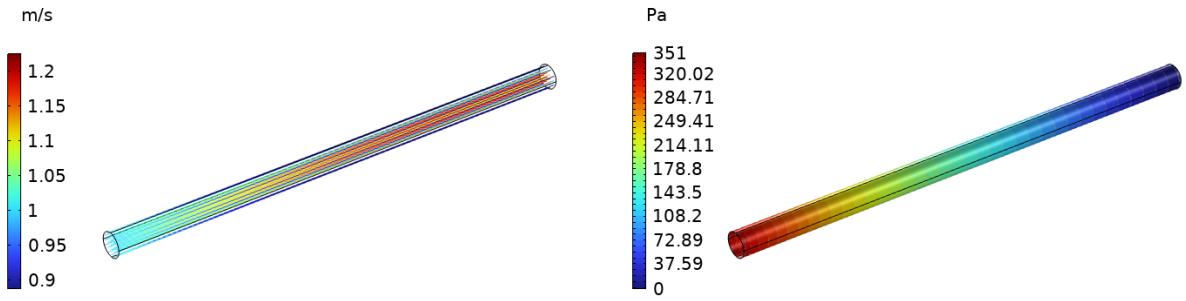

(a) Velocity streamline plot

(b) Pressure differential plot

Figure 4.1: Velocity and pressure plot for a simple straight pipe turbulent flows simulation.

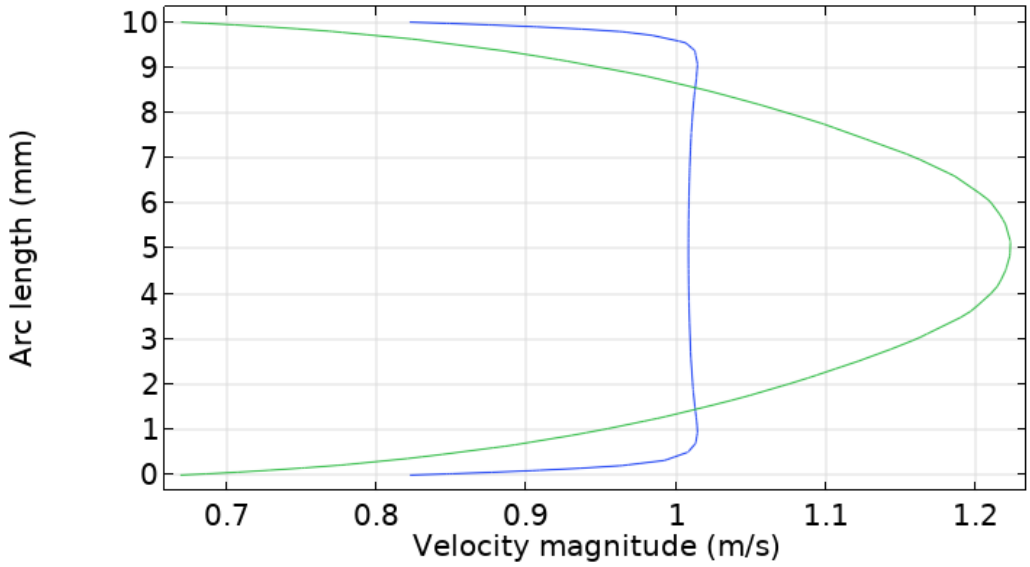

Figure 4.2: Velocity profile of the flow at the beginning of the pipe (blue) and at the end of the pipe (green).

4.1.2 Turbulent flow through simple geometries

The second phase of exploration of CFD involved the modeling of simple geometries which are commonly found in fluid transport systems. The chosen geometries were a pipe which contains two 90 degree elbows, a pipe with a sudden expansion and a pipe with a sudden contraction. The simulations were set up in a similar manner as the first simulation, with a Reynolds number around 15,000, using the $\kappa - \epsilon$ turbulence model.

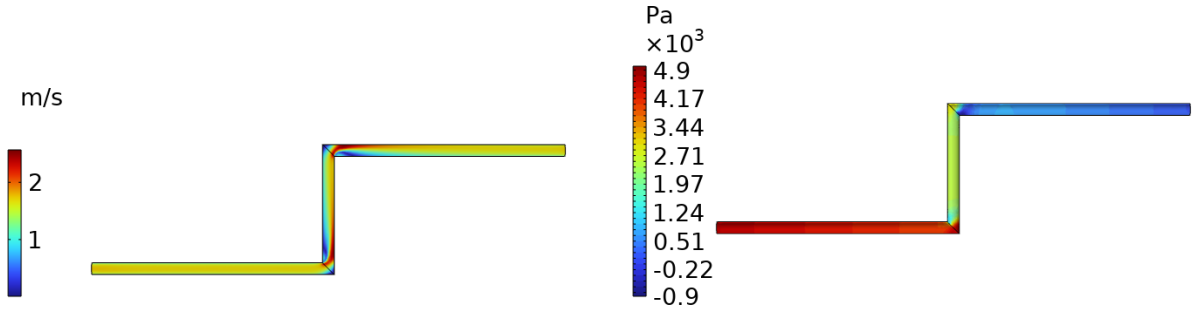

(a) Velocity plot (b) Pressure plot

Figure 4.3: Velocity and pressure distribution in a pipe with a double elbow.

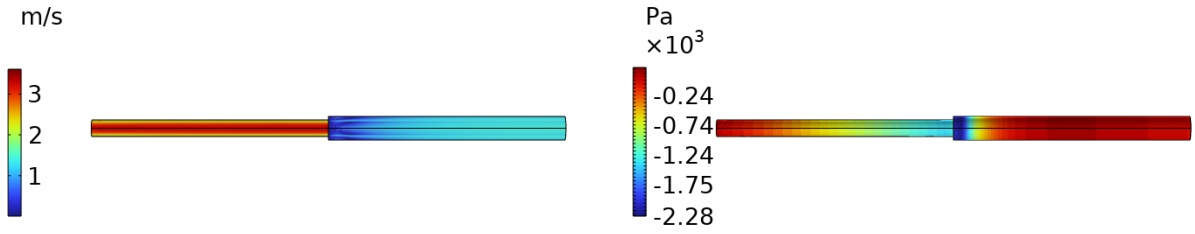

(a) Velocity plot (b) Pressure plot

Figure 4.4: Velocity and pressure distributions in a pipe with sudden expansion.

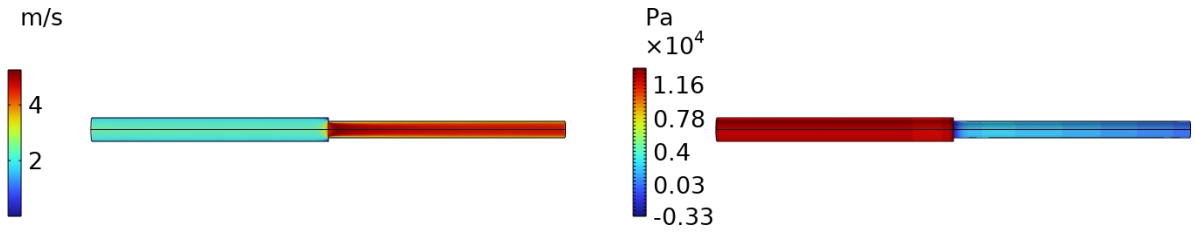

(a) Velocity plot (b) Pressure plot

Figure 4.5: Velocity and pressure distributions in a pipe with sudden contraction.

From the pressure and velocity plots in Figure 4.3, Figure 4.4 and Figure 4.5,it becomes clear that these features have a large impact on the flow behaviour. In the case of the double elbow geometry in

Figure 4.3, the inertia that the flow carries resists the change in direction caused by the elbows. This enables the phenomenon known as flow separation, where the flow of fluid is separated from the pipe wall.

In Figure 4.4 and Figure 4.5, Bernoulli's principle is nicely demonstrated. Bernoulli's principle can be summarized as follows: as the velocity of a liquid or gas increases, the pressure decreases, and conversely, as the velocity of a liquid or gas decreases, the pressure increases. This principle holds as long as the medium is incompressible i.e. constant density. The mathematical expression of this principle is:

$$p + \frac{1}{2}\rho v^2 + \rho g h = constant, \tag{4.1}$$

Once these simple CFD simulations were performed, the choice was made to evaluate a number of other software packages. A detailed report on the evaluation of OpenFOAM and Ansys Fluent can be found in Appendix D. The choice was made to continue working with COMSOL Multiphysics, mainly because of the familiarity of both supervisors with this software package and because of the possibility to offload the computations to the UG's HPC cluster Hábrók.

4.2 Experiment Design

As discussed in Section 1.2, the cooling system used in ASML's NXE EUV includes elbows, orifices, sudden expansions and sudden contractions. The choice was made to narrow the scope of this research on turbulent flows which are caused by a sudden expansion. In the work of Chan and Lien [14], the researchers were able to laminarize the flow and prevent the formation of recirculation zones by placing a porous insert immediately after the sudden expansion. The TPMSs discussed in Section 2.3, when unit cell size is chosen to be sufficiently small, can be considered as a porous material. Taking inspiration from the research by Asbai-Ghoudan et al. [37] and Rathore et al. [38], an experiment is designed with the goal of creating an analytical model which is able to approximate the permeability K and the dimensionless Forcheimer coefficient C_F as a function of porosity ϕ, TPMS type and unit cell size α. The argument for the creation of this model is that CFD simulations of large three-dimensional arrays of TPMS is computationally infeasible.

4.2.1 Generation of TPMS

In MSLattice by Al-Ketan and Abu Al-Rub [15], TPMSs can be generated using various parameters. Relative density D_{rel} is a parameter which varies the fraction of the full cell which is taken up by solid matter, in other words one minus the porosity ϕ. The geometry of the TPMS can be chosen as rectangular, cylindrical or spherical. Furthermore, the unit cell size α, as well as the physical dimensions in the X,Y, and Z direction can be chosen. For the cylindrical and spherical TPMS lattices the physical dimension are chosen using radius r and length l. Finally, the setting mesh density points changes the mesh fineness of the generated TPMS. The generated geometry can then be exported as an STL mesh file.

4.2.2 Mesh Refinement Study

In order to obtain physically relevant and consistent results from the unit cell scale simulations, a mesh refinement study was performed prior to the experiment described in Section 4.2.4. In COMSOL, when using physics defined meshes, the mesh fineness is described by the parameter Element Size, which can range in scale from Extremely Course, to Extremely Fine, with seven steps in between. The Gyroid Sheet geometry with a relative density $D_rel = 30\%$ was arbitrarily chosen to perform the mesh refinement study on. Similarly, to ensure the physical relevance of the results of the Darcy-Forcheimer simulations, a mesh refinement study was conducted for these as well.

The results of the mesh refinement study are shown in Figure 4.6. The mesh refinement study was limited by the 32 gigabytes of available memory on the PC on which the simulations were performed. This unfortunately means that the mesh refinement study could not be performed on the full range of mesh sizes.

In general, mesh refinement studies are expected to converge to a stable value of the metric that is used to assess the mesh refinement. In this case, the metric is the pressure drop over the four unit-cell TPMS element. In this study, as shown in Figure 4.6a, it seems that the pressure drop would converge to a value around 54000 Pa. In order to balance computation time and accuracy of results, the mesh size that is chosen in subsequent computations of unit cell scale systems is the ”Course” mesh as in Table 4.1. At this mesh size, the computations took between six and twelve hours per parametric sweep on a desktop PC with an Intel core i7 7700k with 32 gigabytes of memory. The main culprit to the variation in computation time seemed to be the degree of complexity of the TPMS. For the Darcy-Forcheimer simulation mesh refinement study shown in Figure 4.6b the relative changes of the measured pressure drop were relatively small. the choice was made to perform the Darcy-Forcheimer simulations at the ”Extra Course” mesh size. At this mesh size, the simulations took between one and three hours on the same desktop PC.

Table 4.1: COMSOL Naming convention for mesh size and their respective number of mesh elements for the unit cell scale simulations and the Darcy-Forcheimer simulations.

COMSOL Mesh Size Naming	No. Mesh Elements Unit Cell Scale	No. Mesh Elements Darcy Forcheimer
Extremely Course	$1.07 \cdot 10^5$	$4.11 \cdot 10^4$
Extra Course	$1.79 \cdot 10^5$	$7.39 \cdot 10^4$
Courser	$3.22 \cdot 10^5$	$1.85 \cdot 10^5$
Course	$6.35 \cdot 10^5$	$3.51 \cdot 10^5$
Normal	$1.42 \cdot 10^6$	$9.19 \cdot 10^5$
Fine	$3.21 \cdot 10^6$	$2.87 \cdot 10^6$

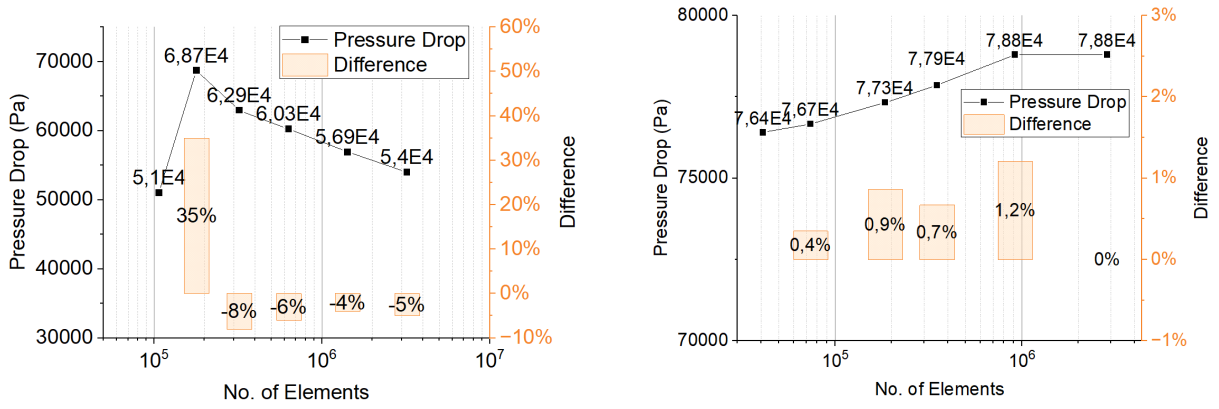

(a) Unit cell scale

(b) Darcy-Forcheimer

Figure 4.6: The results of the mesh refinement study for (a) the unit cell scale simulations and (b) the Darcy-Forcheimer simulations of the Gyroid Sheet geometry with a relative density D_{rel} of 30 %. The figures display the pressure drop as a function of the number of mesh elements, and the relative difference in percentages from each level of mesh refinement to the prior level.

4.2.3 Assessment of Manufacturability

While additive manufacturing has opened up possibilities of using geometries which were previously impossible to manufacture using traditional subtractive manufacturing methods, additive manufacturing methods also have their limits. One of those limits is the printing of overhangs, or layers which are unsupported by the layers below. In many cases, printing of overhangs can be made possible by using one or several remedies.

- Support structures: These structures are temporary structures with the aim of supporting overhangs.
- Print orientation: Through the use of clever orientation of the printed geometry, one can reduce the presence of overhangs.
- Dual extrusion printing: This method involves printing of a support structure of a different material, which can be dissolved or easily broken in post-processing.

While these remedies allow for better printing results, they also add significant post-processing steps. In many cases, the possibility of using these remedies is also limited. Especially in lattices of TPMS, internal overhangs in the lattice are impossible support. Some fused deposition modeling (FDM) printers allow printing with two nozzles, such that a support structure can be printed from a water soluble or breakable material. After completing a print, the support structure can then simply be dissolved in water. Unfortunately, the resolution that is required for the printing of the TPMS inserts is beyond the range of possibilities of FDM printers which allow these methods.

As mentioned in Section 2.3, however, TPMS are well suited for additive manufacturing, because of the lack internal self-interactions in their structure [37]. In order to assess the manufacturability, each of the unit cells are individually assessed using additive manufacturing methods. This involved additively manufacturing the unit cells of each TPMS in a sheet-wise as well as solid-wise configuration using a Creality Ender 3 FDM printer at unit cell size of 20 mm using polylactic acid (PLA).

Appendix E contains images of the samples that were used to assess the manufacturability of the various TPMS unit cells. Assessment of the samples indeed confirmed that overhangs in the geometry of the TPMS are problematic. The geometries that were found to be most problematic are the SD Solid, F-RD Solid, SG Sheet, IW-P Sheet and F-RD Sheet. For the SD Solid and SG Sheet, however, these manufacturability issues are likely reduced when a lattice is constructed from multiple unit cells, as in that case, the overhangs are supported by neighboring unit cells.

In addition to this, a set of SG Sheet inserts is printed using a Formlabs 3+ stereolithography (SLA) resin 3D printer using their proprietary clear resin to assess the manufacturability of the inserts across a range of unit cell sizes. The set of SG Sheet inserts that was produced exposed one of the potential issues which arise with resin 3D printing of these intricate inserts. While the print quality in general is excellent, at unit cell sizes smaller than 2 mm, the resin becomes entrapped in the pores of the TPMS. The entrapped resin is not properly removed during the process of washing the samples with isopropyl alcohol using Formlabs' Form Wash, and subsequently solidifies during the curing process.

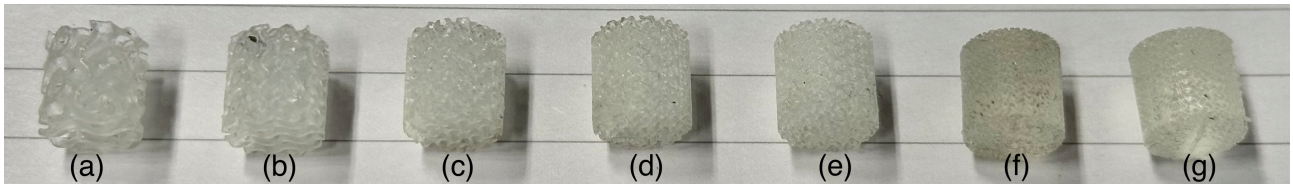

Figure 4.7: SLA resin 3D print of an SG Sheet insert at a unit cell size of (a) 5.0 mm, (b) 3.33 mm, (c) 2.5 mm, (d) 2.0 mm, (e) 1.67 mm, (f) 1.25 mm and (g) 1.0 mm

In subsequent test prints of all TPMS types at a unit cell size of 2 mm, resin became entrapped to a greater degree in other TPMS types than the previously printed SG Sheet. In order to combat this in subsequent prints, the post-processing process was adapted to include a 10 minute wash in isopropyl alcohol in an ultrasonic cleaner. After cleaning the samples were blown dry with a compressed air gun. These steps greatly reduced the entrapment of resin in inserts at a unit cell size of 2 mm.

4.2.4 Experiment to Determine Darcy-Forcheimer Coefficients of TPMS

In COMSOL, simulations were set up for each of the five TPMS geometries for both the solid-wise approach and the sheet-wise approach. The κ-ϵ turbulence model is chosen because of its numerical robustness as discussed in Section 3.5.2. Similar to the computational experimental set up by Asbai-Ghoudan et al. [37], a 1x4x1 unit cell lattice is created for each of the TPMS and for relative densities $D_{rel} = 20\%, 30\%, 40\%, 50\%$ at a unit cell size $\alpha = 1$ mm and $\alpha = 2$ mm. The 1x4x1 unit cell configuration is chosen based on the findings of Asbai-Ghoudan et al. [37]. In their research, a sensitivity analysis of the permeability K to the number of unit cells in the flow direction was performed. They found that increasing the number of unit cells beyond four results in marginal changes in permeability K while mesh size increases proportionally.

Because the goal is to simulate the fluid flow through the empty space in the TPMS, the fluid domain is created by creating a rectangular domain, and subtracting the TPMS geometries. For the unit cell scale simulations with a unit cell size $\alpha = 1$ mm, the dimensions of the rectangular fluid domain that is created are 1 mm by 12 mm by 1 mm in the X, Y and Z directions respectively. Subsequently, an array of 1 by 4 by 1 unit cells of the TPMS is subtracted from this fluid domain using the difference boolean operation. Similarly, for the simulations with unit cell size $\alpha = 2$ mm, the rectangular fluid

domain that is created is 2 mm by 24 mm by 2 mm in the X, Y and Z directions respectively. An array of 1 by 4 by 1 unit cells is again subtracted from the rectangular fluid domain.

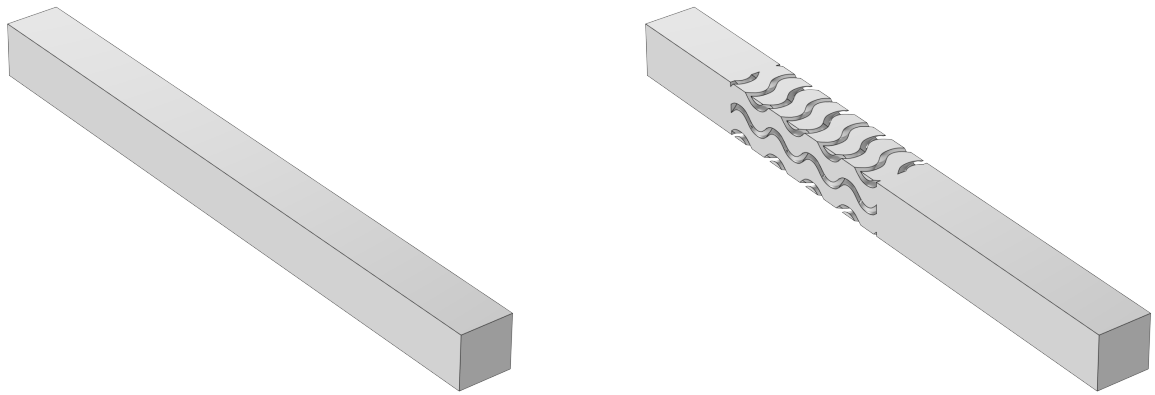

(a) Pre-boolean (b) Post-boolean

Figure 4.8: The generated fluid domain (a) prior to the boolean difference operation in which the TPMS is subtracted from the fluid domain and (b) the fluid domain after the boolean operation for a SG Sheet geometry.

Regarding the boundary conditions in the simulation, the inlet is characterized by a fully developed turbulent flow velocity profile. The outlet conditions are established at atmospheric pressure. Additionally, to replicate a virtually infinite array of unit cells in the X and Z directions, periodic flow boundary conditions are implemented on both boundaries in the XY-plane and the YZ-plane. This periodic flow condition involves utilizing the outgoing flow from one side of the fluid domain as incoming flow on the opposite side of the fluid domain. The interior boundaries resultant from the boolean subtractions of the TPMS from the fluid domain are treated as regular walls with a non-slip condition.

Using the parametric sweep function, a fluid flow with a range of mean velocities from $1\ m/s$ to $2;\ m/s$ with an interval of $0.2\ m/s$ is simulated. For each of these velocities, the pressure drop over the TPMS is evaluated. A second order polynomial is fitted to this data. The intercept of this polynomial is set to zero, because for zero velocity there cannot be a non-zero pressure drop. This polynomial fit results in two coefficients as in

$$\Delta p = -a_1 v - a_2 v^2, \tag{4.2}$$

where a_1 is the linear component of the pressure drop and a_2 is the quadratic component of the pressure drop. This expression is subsequently divided by the length Δx of the TPMS, which is four times the length of the unit cell, to arrive at the pressure gradient

$$\nabla p = \frac{\Delta p}{\Delta x} = -\frac{a_1}{\Delta x} v - \frac{a_2}{\Delta x} \rho v^2, \tag{4.3}$$

where

$$\frac{a_1}{\Delta x} = D\mu = \frac{\mu}{K} \qquad \frac{a_2}{\Delta x} = F\rho = \frac{C_F}{\sqrt{K}}\rho. \tag{4.4}$$

Subsequently, the collected data allows the modeling of the behaviour of the TPMS inserts without the need to model their exact geometry.

4.2.5 Modeling of Flow Through Porous Media

Using the parameters obtained in Section 4.2.4, a simulation of flow through a porous medium was set up. This was done using the COMSOL Multiphysics three-dimensional free and porous media flow simulations. This modeling method also uses the κ-ϵ turbulence model in the non-porous volume. These full scale simulations serve two purposes. The first set of free and porous media flow simulations have a straight tubular fluid domain as shown in Figure 4.9a. By comparing the obtained pressure drop Δp of these simulations with pressure drop Δp obtained analytically from the Darcy-Forcheimer equation, the obtained permeabilities K and Forcheimer coefficients C_F were validated. These simulations were performed at a mean flow velocity $v = 1$ and 2 m/s and for unit cell size $\alpha = 1$ and 2 mm. The pressure drop was also analytically derived at these conditions. From these the difference in pressure drop of the simulated values respective to the theoretically derived values was calculated using:

$$Diff_{\Delta P} = \frac{\Delta P_{sim.} - \Delta P_{theo.}}{\Delta P_{theo.}}. \tag{4.5}$$

This validation does not ensure physical accuracy of the model, rather it tunes the computed permeability K and the Forcheimer coefficient C_F to agree with the free and porous media flow simulations.

Secondly, a set of porous and free media flow simulations was set up with a sudden expansion as the fluid domain as shown in Figure 4.9b. These simulations serve as a tool to gather information about the ability of the TPMS inserts to reduce FIV. Using turbulent kinetic energy κ and the magnitude of vorticity $\vec{\omega}$ as analog for the magnitude of FIV, the candidate geometries were judged on their performance compared to a sudden expansion without any insert. Because the turbulent kinetic energy κ and the magnitude of vorticity $\vec{\omega}$ are a property of the fluid itself and the magnitude of FIV is dependent on the interaction of the fluid with a solid structure, their relation is by no means straight forwards and as such can only be used as a best guess for the magnitude of FIV. The average of the turbulent kinetic energy κ and the vorticity $\vec{\omega}$ was taken of the volume as indicated in Figure 4.10. This set of free and porous media flow simulations of a sudden expansion with a TPMS insert again used the set of permeabilities K and Forcheimer coefficients C_F resultant from the polynomial fit of the unit cell scale simulation data at a unit cell size $\alpha = 2$ mm This unit cell size is also used for experimental validation, which is discussed in Chapter 7.

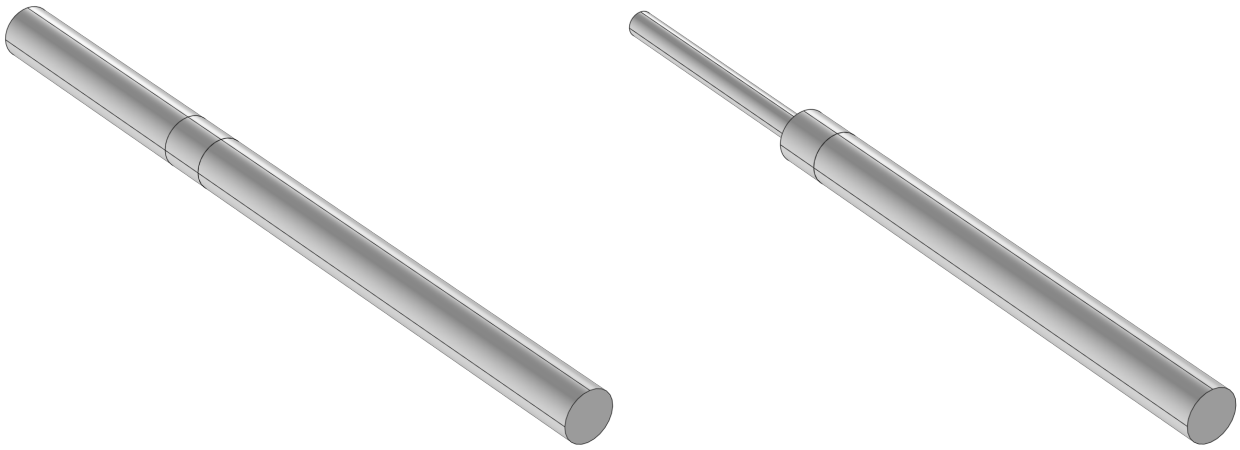

(a) Straight tube (b) Sudden expansion

Figure 4.9: The geometries of free and porous media flow simulations for (a) a straight tube and (b) a sudden expansion.

Figure 4.10: The volume (highlitghted in blue) of which the average turbulent kinetic energy κ and the average vorticity $\vec{\omega}$ will be computed.

The dimensions of the geometries were based on the system description in Section 1.2. The straight tube has a diameter of 10.2 mm. The sudden expansion has a diameter of 5.1 mm in the narrow section and 10.2 mm in the larger section. The mean flow velocities v were set to 1 m/s in the straight tube, and to 4 m/s in the narrow section of the sudden expansion geometry, and to 1 m/s in the wider section of the sudden expansion geometry. The length of the section of tube post-expansion is ten times the pipe diameter.

4.3 Experimental Validation

In order to validate the findings of the simulations, experiments were set up at the experimental facility of ASML. The purpose of these experiments was to validate the Darcy-Forcheimer model parameters for the TPMS and to gather empirical data on the FIV of fluid flow through a sudden expansion with and without a TPMS insert.

4.3.1 Design of Experimental Set-Up

Because of the difference in required feature size of the experimental set-up and the TPMS inserts, the choice was made to manufacture these separately. For the experiment, two geometrical variants of the experimental set-up were produced. The first experimental set-up aims to validate the experimental

findings of the simulations of porous inserts in straight internal flow, that is, there are no narrow or wider sections, nor orifices that obstruct the flow. The second experimental set-up consists of a section of pipe which smoothly transition from a diameter of 10.2 mm to a diameter of 5.1 mm. This narrow section of pipe is followed by a subsequent sudden expansion, with the aim of validating the results from the simulations regarding FIV.

The geometry of the parts was designed in Autodesk Fusion 360 and is shown in Figure 4.11. A more detailed technical drawing of the parts is shown in Appendix F. The pipe ends of the parts were designed to connect using Parker A-LOK® fittings. The two faces of the experimental set-up were bolted together using standard M4 hardware, and to seal the interface of the two faces, an O-ring with an outer diameter of 24 mm and a thickness of 3.1 mm was used. The design of the O-ring gland was based on guidelines by ERI [40].

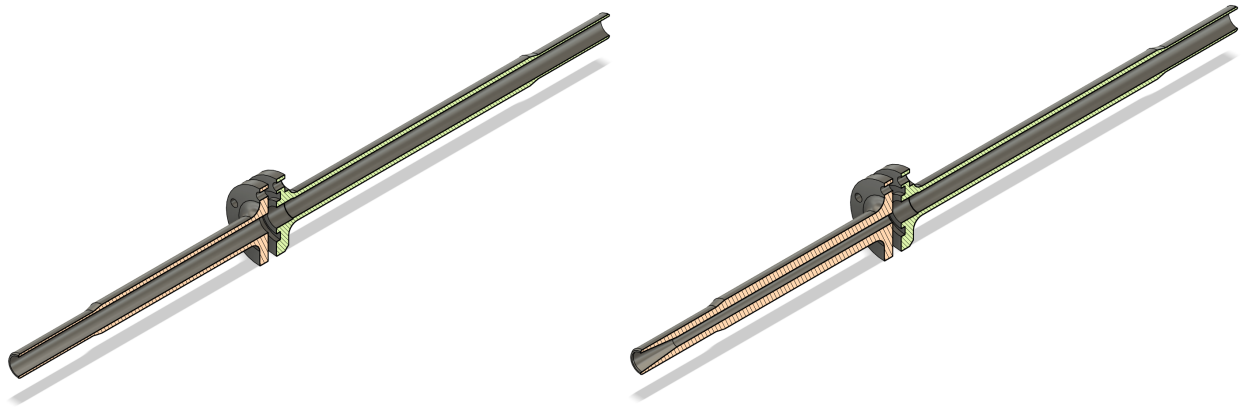

(a) Straight tube (b) Sudden expansion

Figure 4.11: Schematic sectioned overview of the two different experimental set-up designs for the (a) straight tube and the (b) sudden expansion.

These two set-ups were initially 3D printed using a Creality Ender 3 FDM from polyethylene terephthalate glycol (PETG) because of its excellent durability in moist environments. The geometry was sliced in Ultimaker Cura 5.5.0 with 100% infill and a layer height of 0.2 mm. Unfortunately, these prints showed signs of leakage when the experimental set-up was pressurized. This leakage was likely caused by micro-porosity of the material or weak layer adhesion. The parts were subsequently re-printed using a Formlabs 3+ SLA 3D printer using Formlabs' proprietary Grey resin. These prints performed much better and did not show any signs of leakage.

The CAD files for the TPMS inserts were, again, generated using MSLattice [15]. The generated CAD file of the SG Sheet and Solid inserts with a relative density $D_{rel} = 30$ % are shown in Figure 4.12 as an example.

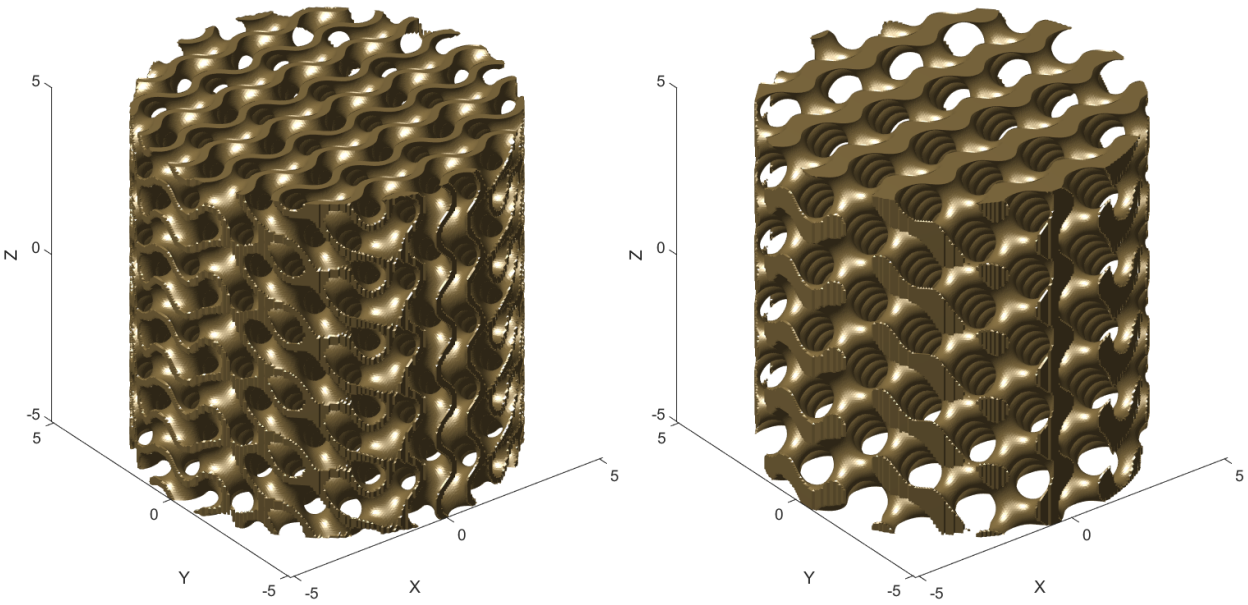

(a) SG Sheet insert (b) SG Solid Insert

Figure 4.12: Examples of the generated geometries for the (a) SG Sheet and (b) SG Solid insert.

Because these TPMS inserts have intricate geometries with feature sizes in the range of micrometers, these inserts needed to be manufactured with a highly capable manufacturing method. For this reason, the TPMS inserts were printed using a Formlabs 3+ SLA 3D printer using Formlabs' proprietary clear resin with a layer height of 0.025 mm. The clear resin is often used for fluidics applications and was therefore deemed suitable for the experiment. As shown in Appendix F, the inserts were held in place in the experimental set-up by a slightly expanded section in the tube of 11 mm as opposed to 10.2 mm. In order to obtain a suitable insert diameter, a set of dowels was printed using a Creality Ender 3 FDM 3D printer. Using these dowels and a digital caliper, an insert diameter of 10.6 mm was deemed ideal. At this insert diameter, the inserts fit snugly into the experimental set-up such that there is no path for the fluid to flow around the inserts, without risking damage to the inserts while inserting and removing them from the set-up. The length of the inserts was chosen to be 10 mm as in the Darcy-Forcheimer simulations. It is unclear whether this aspect ratio for the inserts is ideal to reduce FIV, but because of the limited time, varying this parameter, in addition to TPMS unit cell types, and relative density D_{rel} is beyond the scope of this research.

As discussed in Section 4.2.3, printing the inserts with unit cell sizes α smaller than 2 mm proved to be problematic, the choice was therefore made to print the TPMS inserts at a unit cell size of $\alpha = 2$ mm. In order to print inserts with a unit cell size $\alpha = 2$ mm, more specialized equipment is required. Using the BMF projection micro stereolithography (PμSLA) 3D printer owned by the BMBD research group a sample of the SG sheet geometry was successfully printed at a unit cell size $\alpha = 1$ mm, as shown in Figure 4.13, as a proof of concept. Unfortunately, this sample was printed before the final experiment design was completed and therefore, the dimensions were incompatible with the experimental set-up. It does show, however, that printing TPMS at small unit cell sizes is possible using advanced manufacturing techniques.

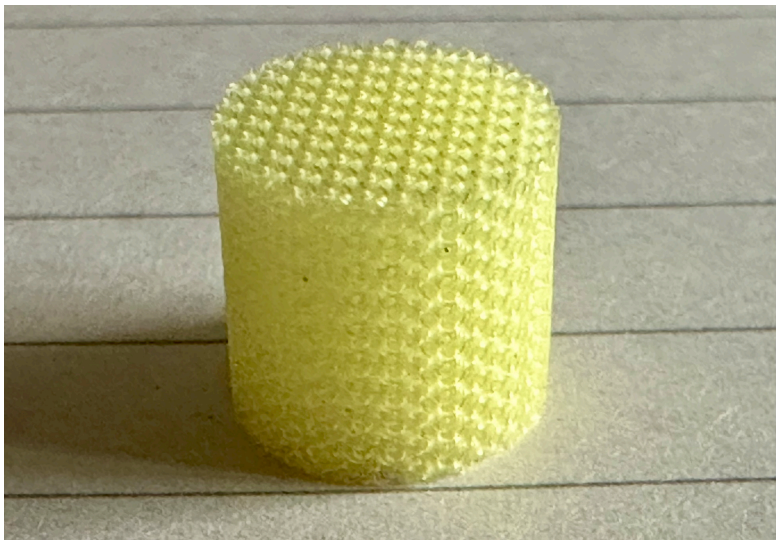

Figure 4.13: Sample insert of the SG sheet geometry at a unit cell size $\alpha = 1$ printed using a BMF PμSLA 3D printer owned by the BMBD research group.

Finally, the inserts used in the experiments were 3D printed at a relative density D_{rel} of 20, 30 and 40 %. The set of geometries with a relative density D_{rel} of 50 % were not printed, mainly because these additional inserts would not yield much additional information while testing time would be increased by an additional 33 %.

4.3.2 Assembly of Experimental Set-Up

The experimental set-up was assembled in one of the cleanrooms at the ASML headquarters in Veldhoven, The Netherlands. The set-up consisted of a variable speed water pump, connected to the 3D printed experimental set-up using proprietary vibration dampening hoses seven meters in length for both the inlet and outlet sides. In the following list, the components of the experimental set-up are listed in their respective order. A schematic overview of this experimental set-up with relevant dimensions is shown in Figure 4.14

- Proprietary FKM vibration dampening hose (FKM).
- Flexible hose (FH).
- Pressure outlet (PO1).
- Kistler 7261 piezoelectric low pressure sensor (K1).
- PCB Piezotronics 105C02 ICP pressure sensor (PCB1).
- 3D printed experimental set-up.
- PCB Piezotronics 105C02 ICP pressure sensor (PCB2).
- Kistler 7261 piezoelectric low pressure sensor (K2).
- Pressure outlet (PO2).
- Flexible hose (FH).
- Keyence clamp on flow rate sensor (FRS).

- Proprietary FKM vibration dampening hose (FKM).

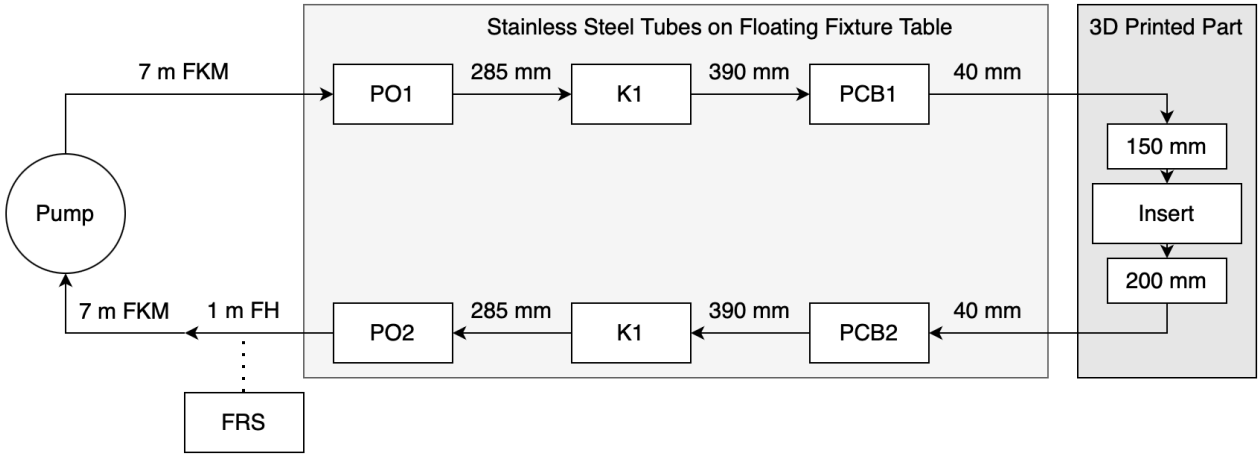

Figure 4.14: Schematic overview of the experimental set-up with relevant measurements.

The pressure outlets were used to connect a pressure sensor to determine the pressure before and after the experiment to determine the pressure drop caused by the presence of the inserts. The Kistler 7261 piezoelectric low pressure sensors were mounted in a custom housing to average out the turbulent fluid pressure fluctuations as much as possible to isolate the acoustics. The PCB Piezotronics 105C02 ICP pressure sensors are flush mounted to pick up turbulent fluid pressure fluctuations. A photograph of this experimental set-up is shown Figure 4.15. At the time of shooting, the sensors have not been connected. Additional detailed photos of the experimental set-up can be found in Appendix G. Using this set-up it was possible to gather pressure drop data which was useful to validate the Darcy-Forcheimer model. The pressure fluctuations sensors were used to assess whether the inserts have the desired influence on turbulence and FIV.

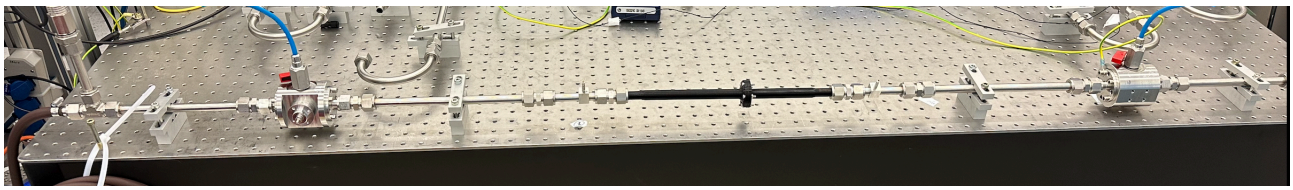

Figure 4.15: Photo of the experimental set-up consisting of pressure taps, sonic sensors and the additively manufactured experimental set-up fastened to an anti-vibration table.

4.3.3 Experimental Methods

The experiment consisted of one minute of data recording at multiple velocity levels for all inserts. Using the four sensors, a comprehensive image of the flow conditions and acoustic performance of the TPMS inserts was formed. As in the research by Kottapalli et al. [2], the results of this experiment were presented in the form of power spectral density (PSD) plots. Additionally, the magnitude of the pressure fluctuations were evaluated for the range 1-60 Hz and 60-1000 Hz. By calculating the range within which three standard-deviations up and down from the mean, or 99.7 % of the pressure fluctuations fall, the magnitude of the pressure fluctuations for the two frequency ranges could easily

be compared between the various TPMS and the no insert case. In addition to this, the pressure drop over the experiment was recorded.

Chapter 5

Unit Cell Scale Simulations

5.1 Simulations

The unit cell scale simulations were successfully completed for four TPMS for both the sheet-wise and solid-wise approach at four levels of relative density from 20 % to 50 % with a step size of 10 % for a unit cell size $\alpha = 1$ mm and 2 mm. This set of 64 simulations consists of a parametric sweep for a six levels of mean flow velocities ranging between one and two meters per second with a step size of 0.2 m/s. Figure 5.1 shows a velocity streamline plot and a surface pressure plot of the SG Sheet TPMS at a relative density $D_{rel} = 30$ %. The streamline plot displays the path that a hypothetical "fluid particle" would travel on. This in an intuitive way to visualize flow patterns, and allows for convenient identification of key flow structures, such as recirculation zones, separation points and vortex shedding. By colorizing the streamlines depending on the magnitude of their velocity, regions of high or low velocity can also be easily identified. The surface pressure plot uses a color scale to plot the pressure at any point on the surface of the fluid domain, and allows for the identification of high and low pressure spots. Because of the periodic boundary conditions in this set of simulations, these spots are unlikely to be present. In these unit cell scale simulations, their main use is identification of adverse pressure gradients.

Using an the average pressure on a cross-sectional cut plane upstream of the TPMS unit cells, the pressure drop over the TPMS elements can be computed. The full pressure drop dataset for all simulations of TPMS unit cells can be found in Appendix H. This data was subsequently processed by fitting second order polynomials to each set of pressure drop values as discussed in Section 4.2.4. After appropriately processing the data this yields the set of permeabilities K and dimensionless Forcheimer coefficient C_F shown in Table 5.1, Table 5.2, Table 5.3 and Table 5.4. Because of the poor manufacturability of the F-RD unit cells and continued issues with convergence during the unit cell scale simulations, the choice was made to eliminate both the solid and sheet variants of the F-RD unit cell from subsequent experiments.

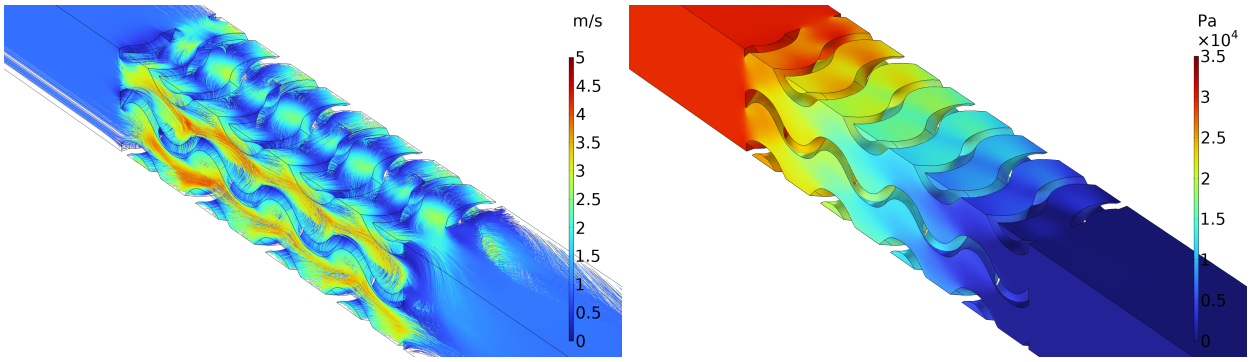

(a) Velocity streamline plot

(b) Surface pressure plot

Figure 5.1: (a) Velocity streamline plot and (b) surface pressure plot of the unit cell scale simulation of the SG Sheet unit cell with unit cell size $\alpha = 1\ mm$, velocity $v = 2\ ms^{-1}$ and relative density $D_{rel} = 30\ \%$.

Table 5.1: Darcy-Forcheimer parameters resultant from the unit cell scale CFD simulations of the SP TPMS.

$\alpha = 1\ mm$	SP Sheet			$\alpha = 2\ mm$	SP Sheet	
D_{rel}	K	C_F		D_{rel}	K	C_F
20 %	4,81E-10	0,108		20 %	1,77E-09	0,100
30 %	2,82E-10	0,200		30 %	9,50E-10	0,183
40 %	1,28E-10	0,462		40 %	2,94E-10	0,330
50 %	1,84E-11	1,261		50 %	7,53E-11	1,263
$\alpha = 1\ mm$	SP Solid			$\alpha = 2\ mm$	SP Solid	
D_{rel}	K	C_F		D_{rel}	K	C_F
20 %	-	-		20 %	-	-
30 %	2,24E-09	0,054		30 %	1,02E-08	0,059
40 %	1,18E-09	0,090		40 %	4,73E-09	0,088
50 %	6,26E-10	0,141		50 %	2,00E-09	0,123

Table 5.2: Darcy-Forcheimer parameters resultant from the unit cell scale CFD simulations of the SD TPMS.

$\alpha = 1\ mm$	SD Sheet			$\alpha = 2\ mm$	SD Sheet	
D_{rel}	K	C_F		D_{rel}	K	C_F
20 %	2,82E-10	0,054		20 %	5,06E-10	0,068
30 %	1,99E-10	0,068		30 %	3,59E-10	0,087
40 %	1,27E-10	0,088		40 %	2,31E-10	0,114
50 %	8,23E-11	0,114		50 %	1,50E-10	0,147
$\alpha = 1\ mm$	SD Solid			$\alpha = 2\ mm$	SD Solid	
D_{rel}	K	C_F		D_{rel}	K	C_F
20 %	9,21E-10	0,039		20 %	1,40E-09	0,042
30 %	5,56E-10	0,053		30 %	8,05E-10	0,055
40 %	3,21E-10	0,067		40 %	5,01E-10	0,075
50 %	2,32E-10	0,077		50 %	3,70E-10	0,088

Table 5.3: Darcy-Forcheimer parameters resultant from the unit cell scale CFD simulations of the SG TPMS.

$\alpha = 1\ mm$	SG Sheet			$\alpha = 2\ mm$	SG Sheet	
D_{rel}	K	C_F		D_{rel}	K	C_F
20 %	3,86E-10	0,052		20 %	1,46E-09	0,047
30 %	2,65E-10	0,062		30 %	9,37E-10	0,054
40 %	1,87E-10	0,075		40 %	6,10E-10	0,061
50 %	1,18E-10	0,093		50 %	3,78E-10	0,074
$\alpha = 1\ mm$	SG Solid			$\alpha = 2\ mm$	SG Solid	
D_{rel}	K	C_F		D_{rel}	K	C_F
20 %	1,40E-09	0,029		20 %	5,27E-09	0,027
30 %	8,44E-10	0,048		30 %	2,97E-09	0,043
40 %	4,93E-10	0,067		40 %	1,63E-09	0,057
50 %	2,86E-10	0,093		50 %	9,21E-10	0,078

Table 5.4: Darcy-Forcheimer parameters resultant from the unit cell scale CFD simulations of the IW-P TPMS.

$\alpha = 1\ mm$	IW-P Sheet			$\alpha = 2\ mm$	IW-P Sheet	
D_{rel}	K	C_F		D_{rel}	K	C_F
20 %	3,78E-10	0,061		20 %	1,43E-09	0,058
30 %	2,37E-10	0,073		30 %	9,11E-10	0,071
40 %	1,56E-10	0,090		40 %	5,67E-10	0,083
50 %	9,05E-11	0,113		50 %	3,36E-10	0,105
$\alpha = 1\ mm$	IW-P Solid			$\alpha = 2\ mm$	IW-P Solid	
D_{rel}	K	C_F		D_{rel}	K	C_F
20 %	1,28E-09	0,026		20 %	5,11E-09	0,026
30 %	8,23E-10	0,040		30 %	5,59E-08	0,224
40 %	4,90E-10	0,050		40 %	-1,77E-09	NaN
50 %	2,75E-10	0,076		50 %	1,88E-09	0,112

The $R_{squared}$, an important metric in the evaluation of polynomial fitting, showed that the second order polynomial fit is an adequate model for the prediction of pressure drop as a function of velocity. The $R_{squared}$ is 99.9 % or higher for every set of simulations, meaning that 99.9 % of the variability in the dependent data is accounted for by the model. However, as can be seen in the data in Table H.4, the simulations for the IW-P Solid geometry at a unit cell size $\alpha = 2$ mm, the results of the polynomial fit to the pressure data resulted in a fit where permeability K is negative for a relative density $D_{rel} = 40$ %. A negative permeability is physically meaningless, because this would result in a negative pressure gradient. This subsequently also invalidates the dimensionless Forcheimer coefficient C_F as it needs to compute the square root of a negative number. This phenomenon persisted after running another iteration of the simulation with a "normal" mesh as defined in Section 4.2.2. The model for the IW-P Sheet insert with a unit cell size $\alpha = 2$ was subsequently excluded from the Darcy-Forcheimer simulations.

5.2 Comparison to Similar Studies

Comparing permeability K and dimensionless Forcheimer coefficient C_F obtained through simulations with the results of a study by Rathore et al. [38], where a similar CFD simulation was performed at a unit cell size $\alpha = 1$ mm and a relative density $D_{rel} = 68$ % of the SP, SD, SG and IW-P solid TPMS, some interesting remarks can be made. This study, however, is performed at a vastly different mean flow velocity. Rathore et al. [38] performed the simulations at mean flow rates between $2.5 \cdot 10^{-6}$ and $2.5 \cdot 10^{-2}$ with steps of order of magnitude, as opposed to between 1 and 2 m/s in the current work. To assess the agreement between the simulations made by Rathore et al. [38] and in the current work, simulations were set up using the same relative density $D_{rel} = 68$ %, and using a parametric sweep of velocities at $2.5E-6$ m/s, $2.5E-5$ m/s, $2.5E-4$ m/s, $2.5E-3$ m/s and $2.5E-2$ m/s. The simulations were set up using a solver for laminar flow in COMSOL Multiphysics. The resultant permeabilities K and dimensionless Forcheimer coefficients C_F are show in Table 5.5.

Table 5.5: Comparison of the permeability K and dimensionless Forcheimer coefficient C_F in the work of Rathore et al. [38] and in the current work (c.w.).

TPMS Type	D_{rel}	K [38]	C_F [38]	K c.w.	C_F c.w.
SP	68 %	$5.19 \cdot 10^{-10}$	0.525	$5.54 \cdot 10^{-10}$	2.412
SD	68 %	$4.34 \cdot 10^{-10}$	0.496	$3.99 \cdot 10^{-10}$	0.475
SG	68 %	$7.89 \cdot 10^{-10}$	1.025	$7.28 \cdot 10^{-10}$	0.782
IW-P	68 %	$3.05 \cdot 10^{-10}$	1.173	$3.12 \cdot 10^{-10}$	0.918

A plot comparing the pressure gradient as a function of the mean flow velocity is shown in Figure 5.2. The agreement between the two studies is strong. Considering that the domain in the study by Rathore et al. [38] is characterized by closed channel flow through an array of 5 by 5 by 5 unit cells of the respective TPMS, while the current work is characterized by flow through a 1 by 1 by 4 array of the respective TPMS with periodic boundary conditions. The fact that despite these differences in modeling approach, the values for K and C_F are close adds credibility to the used methodology of the current work.

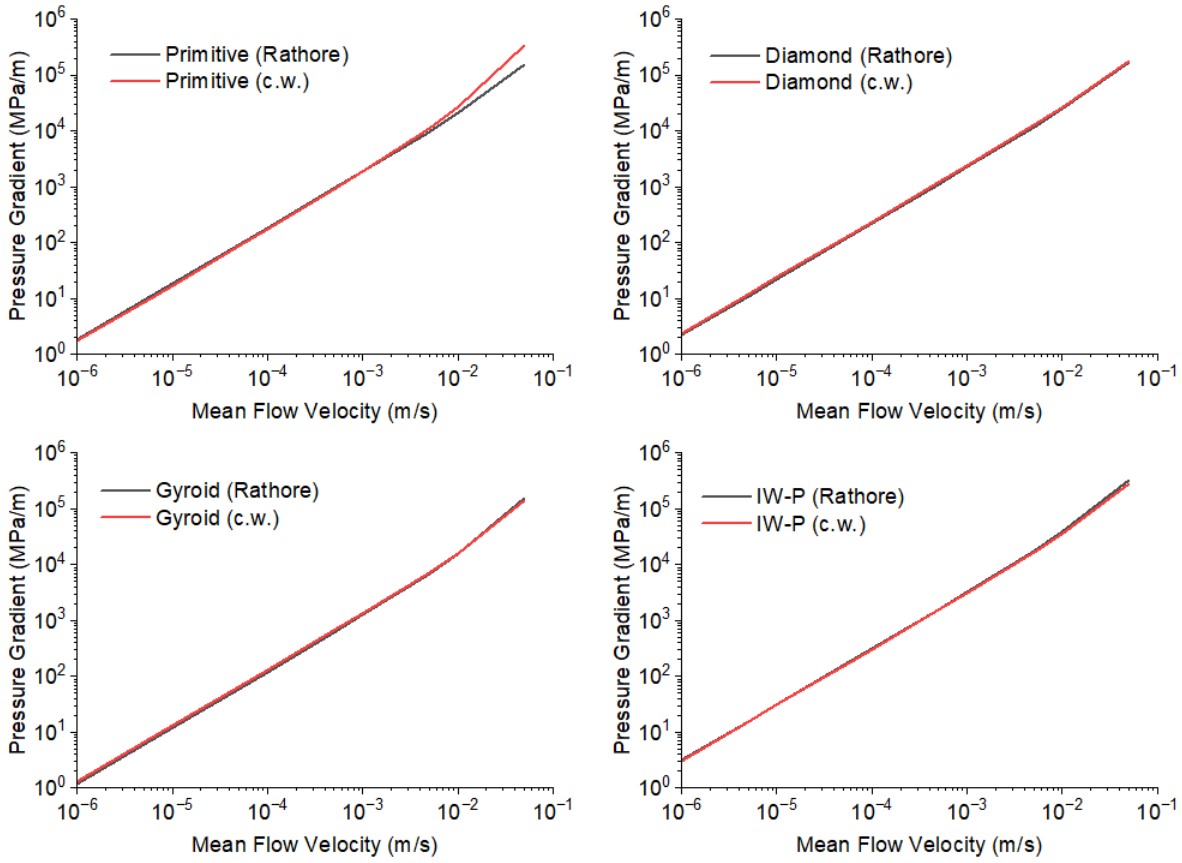

Figure 5.2: Log-log plot of the pressure gradient as a function of mean flow velocity comparing the results of Rathore et al. [38] with the results of the current work.

Chapter 6

Darcy-Forcheimer Model Simulations

6.1 Validation of the Darcy-Forcheimer Model

Using the results of the unit cell scale simulations, a Darcy-Forcheimer porous media flow model was developed. The Darcy-Forcheimer simulations were performed for both fluid flow through a straight tube with a TPMS insert, and for fluid flow through a sudden expansion with a TPMS insert. The former to validate that the Darcy-Forcheimer model is in agreement with the analytically derived pressure drops from the Darcy-Forcheimer equation. The latter to assess the inserts' ability to mitigate FIV.

The Darcy-Forcheimer parameters obtained in Chapter 5 are used as parameters for the free and porous media flow simulations discussed in Section 4.2.5. A box plot showing the difference in pressure drop of the simulations respective to the analytically derived values is shown in Figure 6.1. The full dataset on which this box plot is based can be found in Appendix I. The agreement between the simulated pressure drop and the analytically derived pressure drop is acceptable, with a mean percentage change with respect to the theoretical pressure drop between 0 and 10 %, although in the most extreme case the pressure drop resultant from the simulation is 30.2 % higher than the pressure drop that is derived analytically for the SP Solid TPMS. The reason why some of the simulation results deviate significantly from the analytically derived pressure drops is unknown.

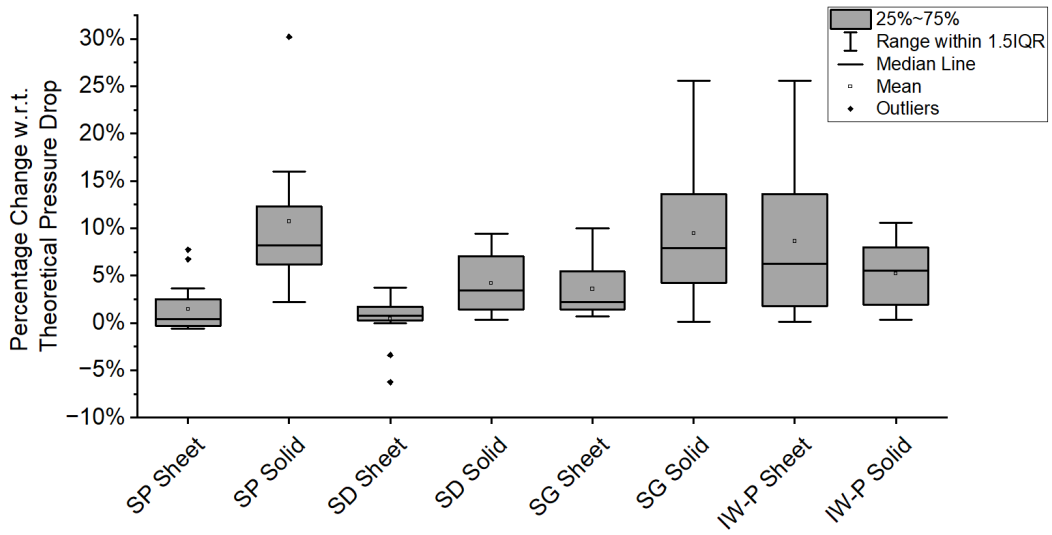

Figure 6.1: Box plot displaying the difference in pressure drop of the simulated values respective to the analytically derived values for each distinct TPMS geometry

6.2 Modeling of Flow Through a Sudden Expansion

The second set of Darcy-Forcheimer simulations as discussed in Section 4.2.5 is focused on assessing the the ability of the TPMS inserts to diffuse turbulence. In this section, a comparison is made between the baseline case without an insert, and the case where a SG Sheet insert is used with a relative density $D_{rel} = 30$ %, and the unit cell size $\alpha = 2$ mm. This TPMS was chosen arbitrarily, because the data for all TPMS are quite close in terms of performance, such that the respective plots are representative for the performance of the other TPMS.

As shown in Figure 6.2, the flow in the baseline case is characterized by a high velocity fluid jet originating in the narrow tube section when entering the expansion. Furthermore, as shown in Figure 6.3, in the baseline case, the characteristic recirculation zones responsible for VIV as discussed in Section 2.1 are present. In the case of the TPMS insert this high velocity jet is and the recirculation zones are absent, because the incoming fluid is diffused uniformly throughout the porous structure of the TPMS insert. Figure 6.4 clearly illustrates the main drawback of TPMS inserts as turbulence diffuser. In the baseline case, the pressure drop that occurs as a result of the sudden expansion is negligibly small when compared to the pressure drop that is cause by the TPMS insert.

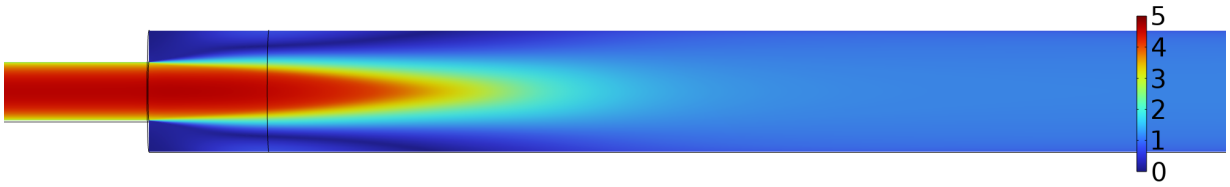

(a) Baseline

(b) SG Sheet, $D_{rel} = 30$ %, $\alpha = 1$ mm

Figure 6.2: Velocity plot for (a) the baseline case without any insert and (b) of the SG Sheet insert where relative density $D_{rel} = 30$ % and unit cell size $\alpha = 2$ mm.

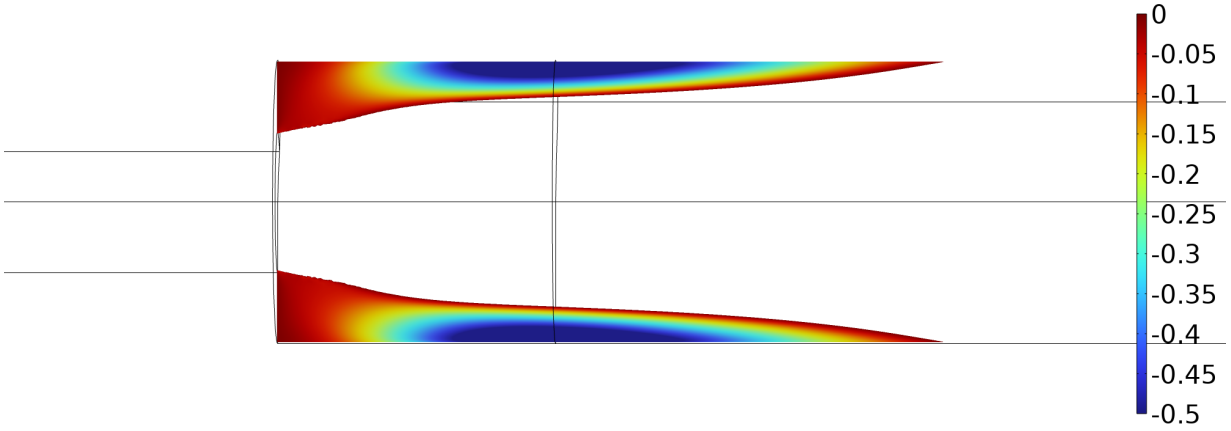

Figure 6.3: Velocity plot for the negative component of the velocity in the flow direction, indicating the presence of recirculation zones for the baseline simulations.

(a) Baseline

(b) SG Sheet, $D_{rel} = 30$ %, $\alpha = 1$ mm

Figure 6.4: Pressure plot for (a) the baseline case without any insert and (b) of the SG Sheet insert where relative density $D_{rel} = 30$ % and unit cell size $\alpha = 2$ mm.

When comparing the turbulent kinetic energy κ for the baseline case and for the SG Sheet insert, it is clear that the insert is able to significantly reduce the turbulent kinetic energy that is generated by the sudden expansion. This effect seems to propagate a significant amount along the length of the flow path, such that the turbulent kinetic energy κ is still significantly lower at the outlet of the simulated fluid domain.

(a) Baseline

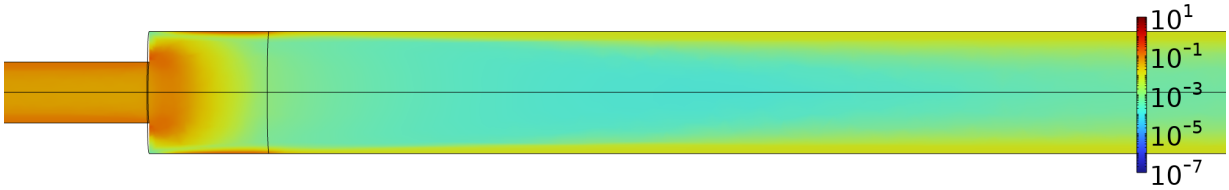

(b) SG Sheet, $D_{rel} = 30$ %, $\alpha = 1$ mm

Figure 6.5: Logarithmic turbulent kinetic energy plot for (a) the baseline case without any insert and (b) of the SG Sheet insert where relative density $D_{rel} = 30$ % and unit cell size $\alpha = 2$ mm.

Comparing the vorticity $\vec{\omega}$ for the baseline case and the SG Sheet insert, the same phenomenon is observed as for the turbulent kinetic energy κ. The TPMS insert significantly reduces the vorticity

$\vec{\omega}$ that is generated by the sudden expansion. As the flow continues along its path after the sudden expansion, however, the vorticity profile for the baseline case and the SG Sheet insert both seem to revert to a fully developed turbulent flow profile.

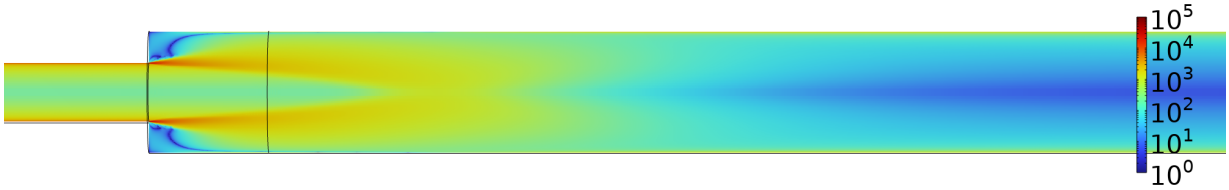

(a) Baseline

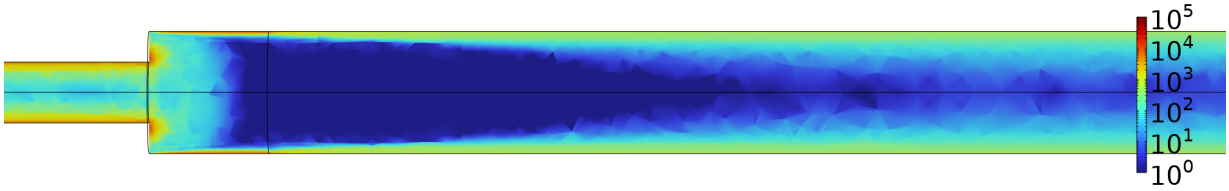

(b) SG Sheet, $D_{rel} = 30$ %, $\alpha = 1$ mm

Figure 6.6: Logarithmic vorticity plot for (a) the baseline case without any insert and (b) of the SG Sheet insert where relative density $D_{rel} = 30$ % and unit cell size $\alpha = 2$ mm.

To succinctly quantify these findings, the average turbulent kinetic energy κ and the average vorticity $\vec{\omega}$ are computed for the volume after the insert as discussed in Section 4.2.5 and shown in Figure 6.7 and Figure 6.8 respectively.

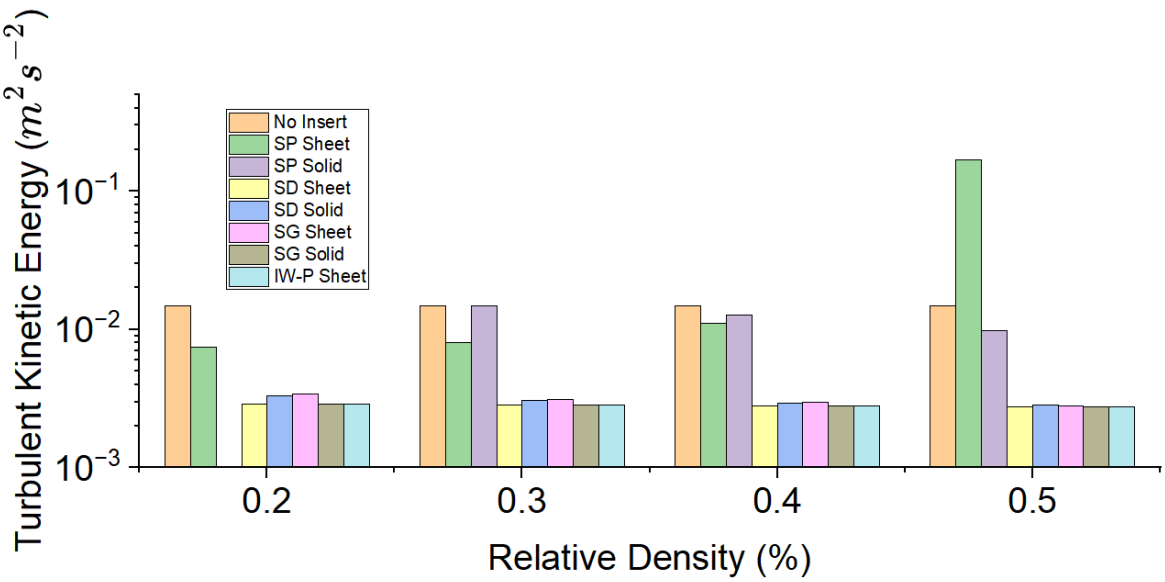

Figure 6.7: Logarithmic column plot of the average turbulent kinetic energy κ for the no insert case and for each of the distinct TPMS geometries at every tested relative density D_{rel} and unit cell size $\alpha = 2$ mm.

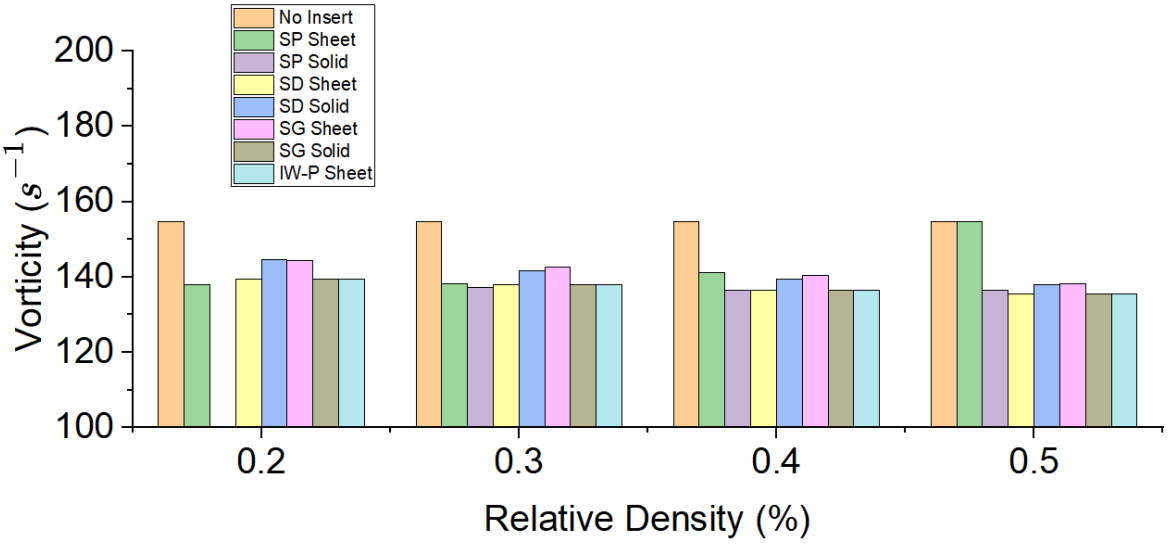

Figure 6.8: Column plot of the average vorticity $\vec{\omega}$ for the no insert case and for each of the distinct TPMS geometries at every tested relative density D_{rel} and unit cell size $\alpha = 2$ mm.

When looking at the average turbulent kinetic energy κ and the average vorticity $\vec{\omega}$ after the sudden expansion as shown in Figure 6.7 and Figure 6.8 respectively, the TPMS significantly outperform

the no insert case, with the exception of the SP Sheet insert at a relative density $D_{rel} = 50$ %. When examining this specific unit cell more closely and comparing it to the SP Sheet unit cell at a relative density $D_{rel} = 40$ % and 60 % as shown in Figure 6.9, it becomes clear why this unit cell performs poorly at these higher relative densities. This is also reflected by the permeability k and dimensionless Forcheimer coefficient C_F as shown in Table 5.1. This specific unit cell is especially restrictive because of how the relative density D_{rel} influences the pore size of the unit cell. At a relative density $D_{rel} = 60$ %, the SP Sheet geometry is no longer open-cell porous, and as such would theoretically have zero permeability.

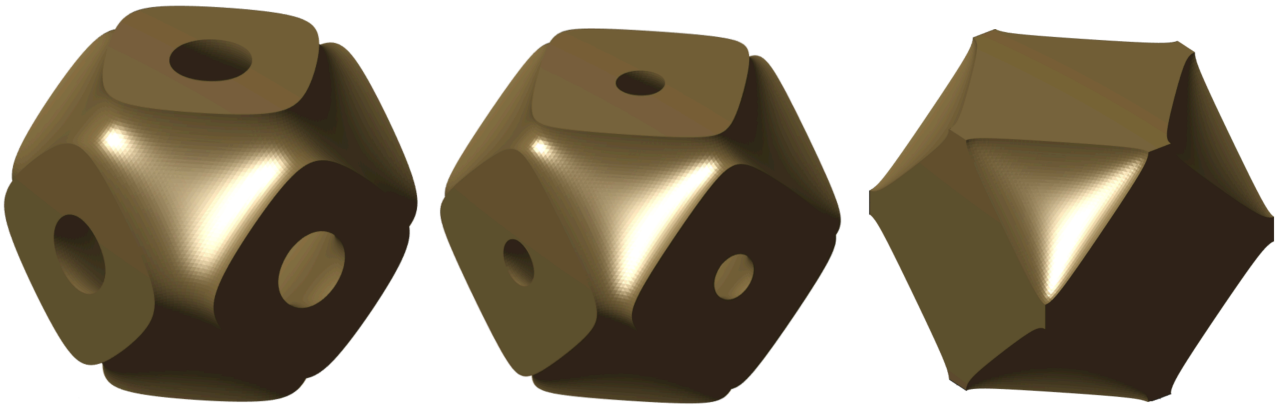

(a) (b) (c)

Figure 6.9: The unit cell of the SP Sheet geometry at a (a) relative density $D_{rel} = 40$ %, (b) relative density $D_{rel} = 50$ % and (c) relative density $D_{rel} = 60$ %.

Similarly, the average vorticity $\vec{\omega}$ is also significantly lower in most cases with a TPMS insert, with the exception of the SP Sheet at a relative density $D_{rel} = 50$ %. This poor performance is likely also explained by the small pore size of the SP Sheet at a relative density $D_{rel} = 50$ %.

The relative reduction of the average turbulent kinetic energy κ and the average vorticity $\vec{\omega}$ are displayed in Table 6.1. The average turbulent kinetic energy κ and the average vorticity $\vec{\omega}$ of the two best performing TPMS are split per relative density D_{rel} in Table 6.2.

Table 6.1: The relative reduction of the average turbulent kinetic energy κ and the average vorticity $\vec{\omega}$ compared to the simulation of a sudden expansion without an insert.

TPMS Type	Turbulent Kinetic Energy κ	Vorticity $\vec{\omega}$
SP Sheet	-228.8 %	7.5 %
SP Solid	15.8 %	11.6 %
SD Sheet	80.9 %	11.2 %
SD Solid	79.4 %	8.9 %
SG Sheet	79.1 %	8.6 %
SG Solid	80.9 %	11.2 %
IW-P Sheet	80.9 %	11.2 %

Table 6.2: The relative reduction of the average turbulent kinetic energy κ and the average vorticity $\vec{\omega}$ compared to the simulation of a sudden expansion without an insert for the SG Solid and IW-P Sheet TPMS specified per relative density D_{rel}.

TPMS Type	Relative Density D_{rel}	Turbulent Kinetic Energy κ	Vorticity $\vec{\omega}$
SG Solid	20 %	80.3 %	9.8 %
	30 %	80.9 %	10.8 %
	40 %	81.2 %	11.7 %
	50 %	81.2 %	12.4 %
IW-P Sheet	20 %	80.3 %	9.8 %
	30 %	80.9 %	10.8 %
	40 %	81.2 %	11.7 %
	50 %	81.2 %	12.4 %

As shown in Table 6.2, increases in relative density D_{rel}, only marginally reduces the turbulent kinetic energy κ and vorticity $\vec{\omega}$.

Chapter 7

Experimental Validation

In the experimental validation, as described in Section 4.3, two variations of experiments are performed. This set of the experiments is discussed in Section 7.1. This set of the experiments is discussed in Section 7.2.

7.1 Flow Through a TPMS Insert in a Straight Pipe

The purpose of the first experiment is to validate the Darcy-Forcheimer model for the pressure drop over the TPMS inserts. Four different TPMS inserts were placed in the flow path. The inserts that were tested are the SD Sheet at a relative density of 20 and 30 % and the SG Sheet at a relative density of 20 and 30 %. The pressure gradient as a function of relative density is shown in Figure 7.1 for the SD Sheet and SG Sheet inserts.

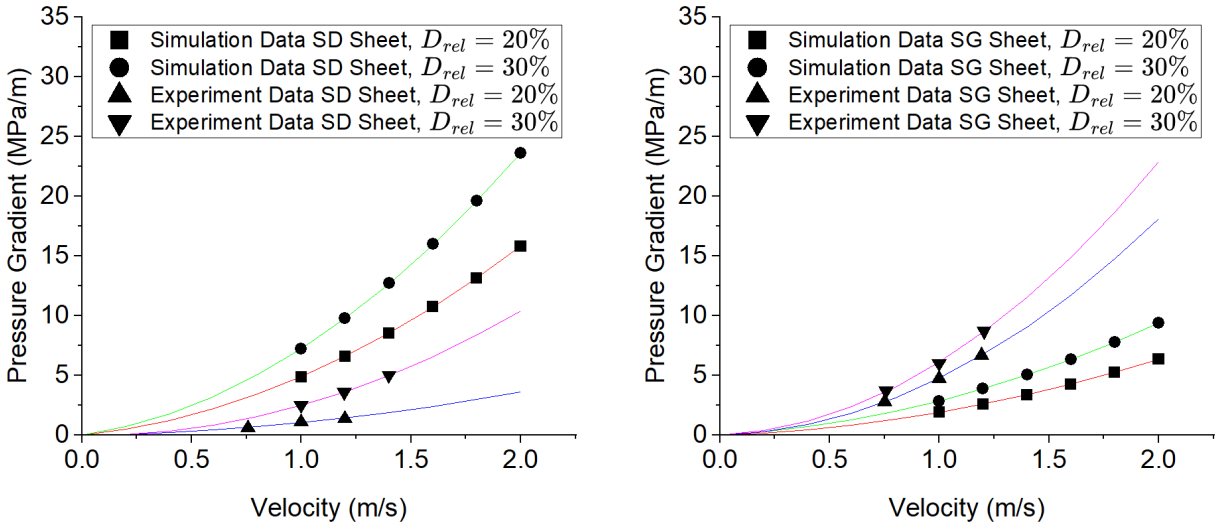

(a) (b)

Figure 7.1: The pressure gradient as a function of mean flow velocity for the (a) SD Sheet and (b) SG Sheet at a relative density of 20 and 30 % based on simulation data and experimental data.

There is a large discrepancy between the pressure gradient as a function of velocity resultant from the experimental data as compared to the simulated data. In the case of the SD Sheet insert, the experiment yielded significantly lower pressure drops than expected. In the case of the SG Sheet insert, the experiment yielded significantly larger pressure drops than expected.

On the modeling side, the assumptions and simplifications that are made, boundary conditions, turbulence modeling and mesh quality can all significantly contribute to divergence between simulation and experiment. Starting with the unit cell scale simulations, the periodic boundary condition that is used to model an infinitely large array of TPMS unit cells is a simplification which can introduce error. As the unit cell size approaches zero, the number of unit cells in an insert approaches infinity. Because the inserts contain a finite amount of unit cells, at the outer edges of the inserts an interaction with the pipe walls exists in reality which is not accounted for in the simulations. Because of this effect, the permeability K and dimensionless Forcheimer coefficient C_F derived from the unit cell scale simulations are potentially inaccurate. Additionally, assumptions about the as fluid temperature and fluid composition have an effect on the the density ρ and dynamic viscosity μ of the fluid. Differences between the assumptions and the actual values at the day of the experiment can also introduce error.

The turbulence modeling method that is used is, as discussed in Section 3.5.2, the RANS $\kappa - \epsilon$ approach. The $\kappa - \epsilon$ turbulence model is known to be numerically robust, but it can yield inaccurate results in adverse pressure gradients and situations where there is a lot of interaction with walls. A significant adverse pressure gradient is an inherent characteristic of turbulent internal flow. The adverse pressure gradient can clearly be observed in Figure 5.1. Because of the large surface area of the TPMS's, there is also a relatively large amount of interaction between the fluid and the TPMS compared to unobstructed internal flows. An attempt was made to produce a comparable Darcy-Forcheimer model using the SST turbulence modeling, a combination of the $\kappa-\epsilon$ and $\kappa-\omega$ turbulence models, but due to a lack of time, and problems with convergence this was beyond the scope of the current research.

On the experimental side, because of the limited amount of data that was gathered, it is difficult to assess the likelihood that the measurements for the experiment where no expansion was present are accurate. When dissecting the pressure drop for the experiment with a sudden expansion as shown in Figure 7.2, it becomes clear that the pressure drop data may not be accurate. When comparing the SD Sheet pressure data at a mean flow velocity $v = 1$ m/s, the pressure drop is 73.5 KPa and 71.0 KPa for the respective relative densities $D_{rel} = 20$ % and 30 %. Similarly, for the SG Sheet geometry, the pressure drop is 110 KPa and 112 KPa for the relative densities $D_{rel} = 20$ % and 30 %. When looking at the simulated pressure drops, a 47.7 % and 48.5 % increase in pressure drop is observed going from $D_{rel} = 20$ % to 30 % for the SD Sheet and SG Sheet respectively. This is consistent with the effect one would expect from an increase in relative density because of the effect it has on pore size and channel length on a unit cell scale level. In hindsight, it would have been useful to perform some experiments earlier in the project, such that the source of the divergence between experiment and simulation could have been found. Based on the currently available data, no conclusive statements can be made about the degree to which the model that was produced based on simulation data is an accurate representation of reality.

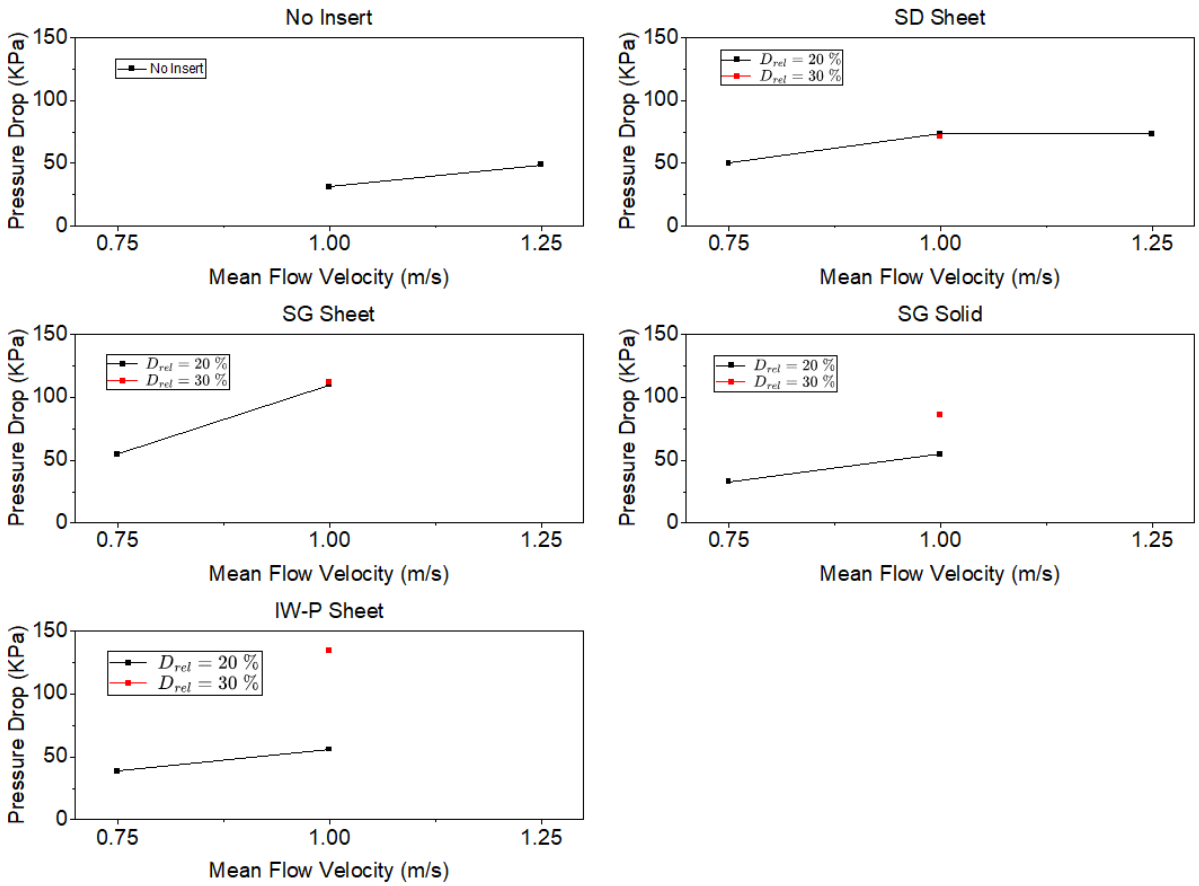

Figure 7.2: Scatter and line plot of the pressure drop data of the experiments with sudden expansion divided by TPMS type.

7.2 Experimental Acoustics and Fluid Dynamics Performance

The purpose of the second set of experiments is to evaluate the ability of the TPMS inserts to reduce the presence of FIV. The performance in terms of the ability of the TPMS inserts to reduce FIV and turbulent fluid pressure fluctuations are captured by the PSD plots of the acoustic pressure fluctuations in Figure 7.3 and Figure 7.4 and the turbulent fluid pressure fluctuations in Figure 7.5 and Figure 7.6. At frequencies between 1 and 10 Hz, the presence of a TPMS insert seems to have a detrimental effect on the magnitude of both the acoustic pressure fluctuations and the turbulent fluid pressure fluctuations. In the range of 10 to 100 Hz, some of the inserts seem to decrease the acoustic and turbulent fluid pressure fluctuations both before and after the insert compared to the no insert case. From 100 Hz onward, the no insert case seems to be the best performer with some small regions where some inserts seem to perform better.

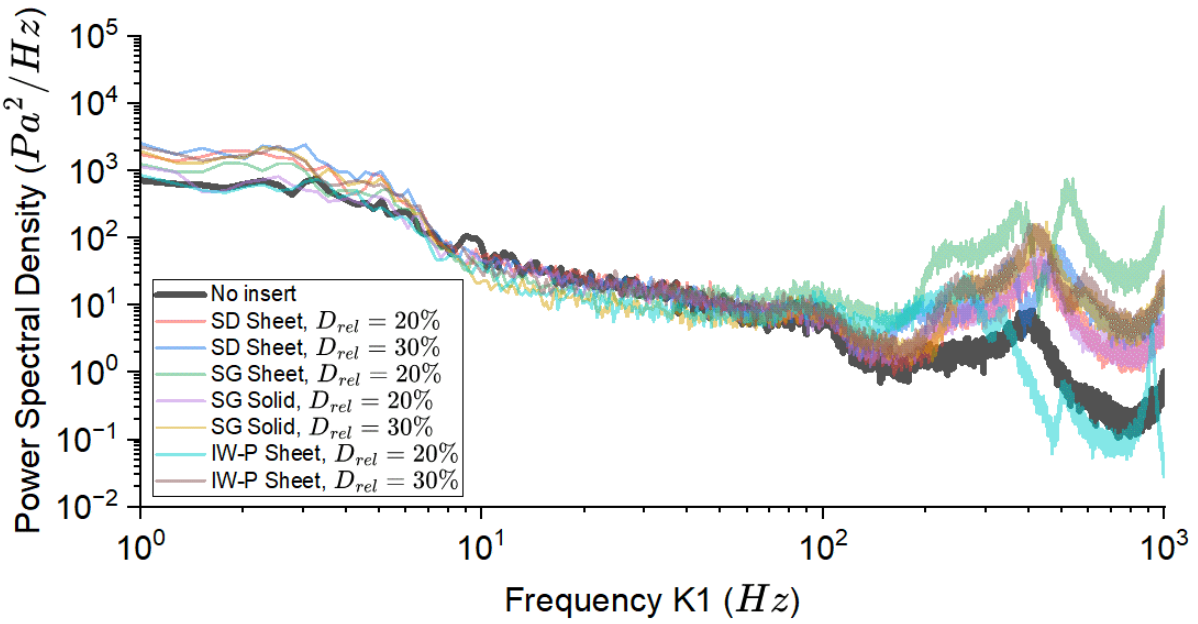

Figure 7.3: PSD plot of the acoustic pressure fluctuations at sensor location K1 situated upstream of the 3D printed part of the experimental set-up

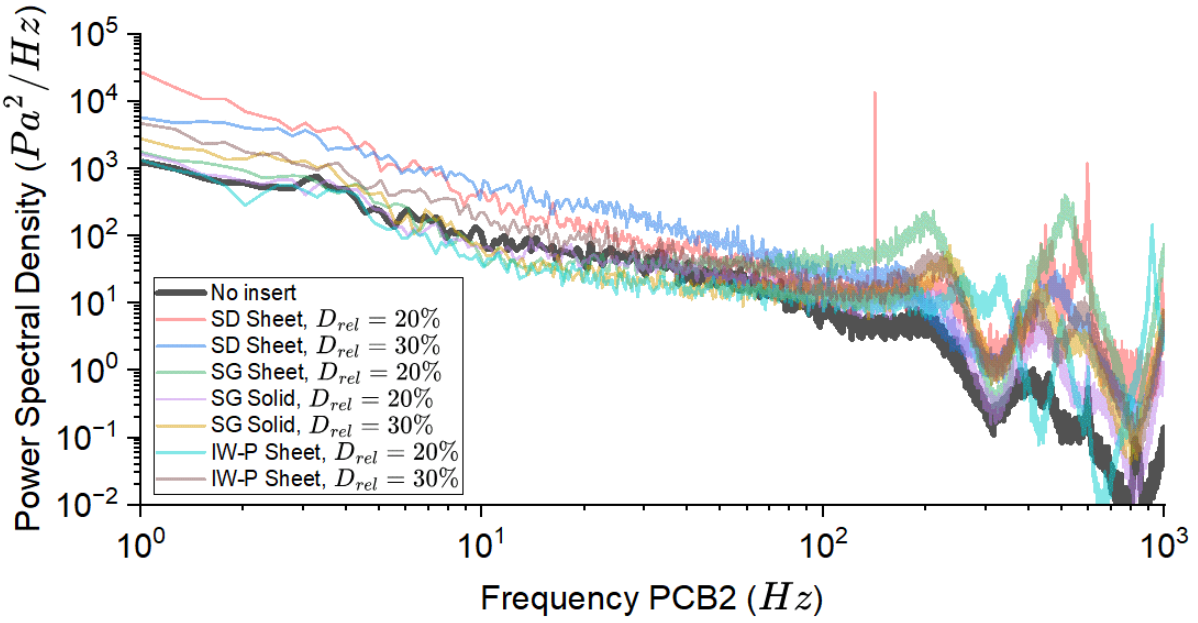

Figure 7.4: PSD plot of the acoustic pressure fluctuations at sensor location K2 situated downstream of the 3D printed part of the experimental set-up

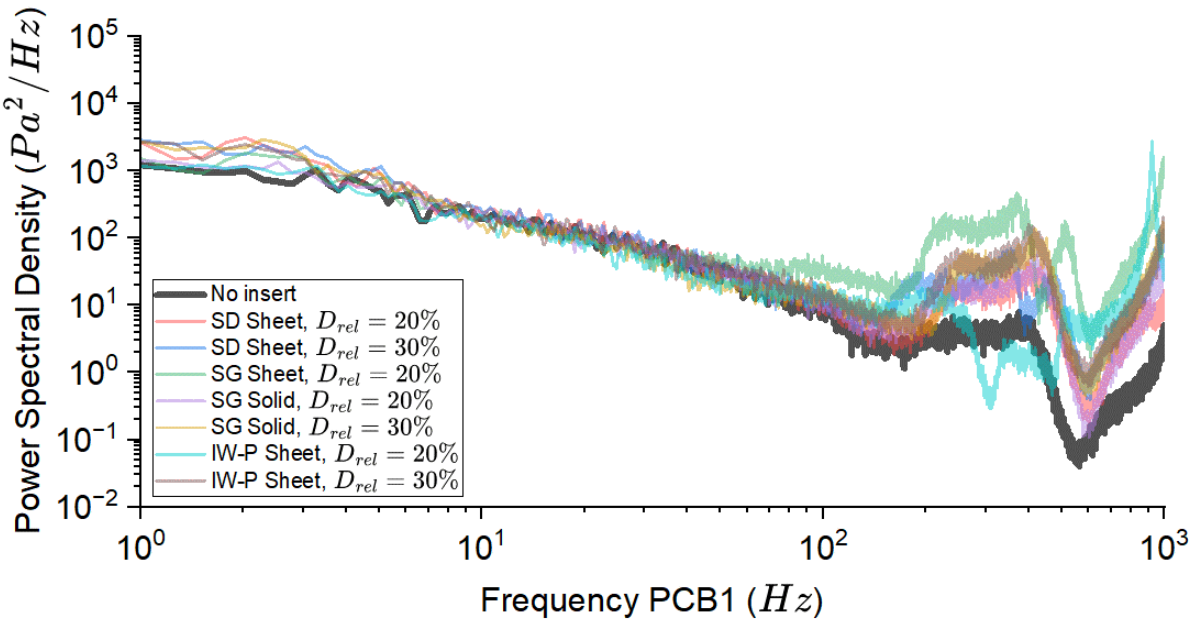

Figure 7.5: PSD plot of the turbulent fluid pressure fluctuations at sensor location PCB1 situated upstream of the 3D printed part of the experimental set-up

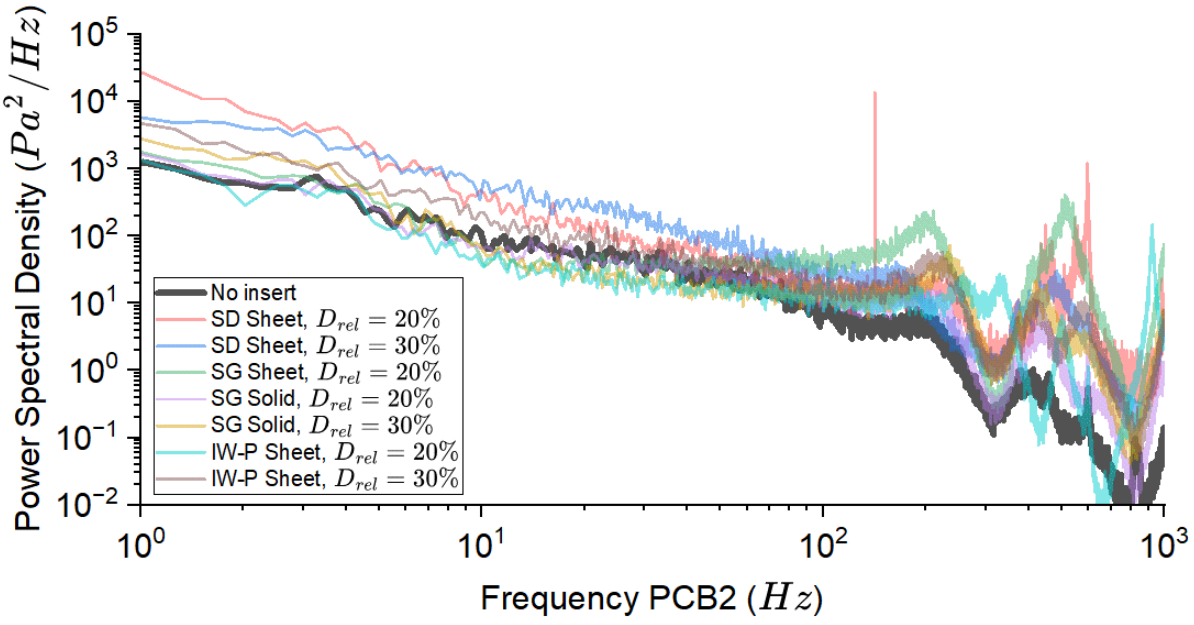

Figure 7.6: PSD plot of the turbulent fluid pressure fluctuations at sensor location PCB2 situated downstream of the 3D printed part of the experimental set-up

To quantify the performance of the TPMS inserts in terms of the reduction in acoustic pressure

fluctuations and turbulent fluid pressure fluctuations, Figure 7.7 displays the 3σ range for the no insert case and the TPMS inserts for the frequency range from 1 to 60 Hz and from 60 to 1000 Hz. In the higher frequency range, the no insert case is the best performer for both the acoustic pressure fluctuations and the turbulent fluid pressure fluctuations upstream and downstream from the sudden expansion. For the lower frequency range, the IW-P Sheet at a relative density $D_{rel} = 20$ % is consistently the best performer for both the acoustic pressure fluctuations and the turbulent fluid pressure fluctuations upstream and downstream from the sudden expansion, although by a small margin. Notably, the SG Sheet at a relative density $D_{rel} = 20$ % performs on par with the no inset case for the lower frequency range. The other TPMS inserts consistently perform worse than the no insert case.

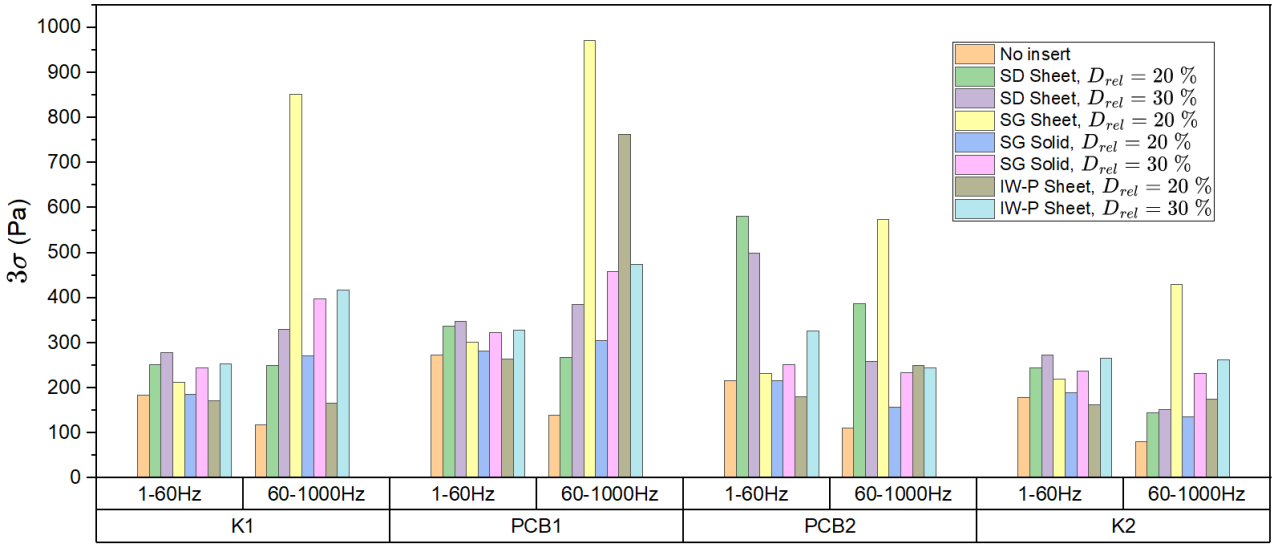

Figure 7.7: Column plot of 3σ pressure for the no insert case and for the TPMS inserts grouped by frequency range and sensor.

Comparing the results of the simulations with the results of the experiments it is obvious that the expected reduction in turbulent kinetic energy κ and the vorticity $\vec{\omega}$ does not translate to significant reductions in terms of the magnitude of acoustic pressure fluctuations and turbulent fluid pressure fluctuations. While in both the simulations and the experimental data, the IW-P Sheet and the SG Solid are among the better performing TPMS, the performance of the TPMS inserts in the experiment is generally underwhelming.

One of the factors that may potentially contribute to this poor performance is the geometric difference between the simulation set-up and the experimental set-up. For the simulations, data collection can occur at any arbitrary location in the fluid domain, while in real-world experiments, the locations in which data can be gathered is limited by the ability to position sensors. In the simulations, the turbulent kinetic energy κ and vorticity $\vec{\omega}$ are computed for the entire fluid domain after the insert, while in the experimental set-up the sensors PCB1 and PCB2 are located 190 mm and 240 mm away from the insert respectively. For sensors K1 and K2 the distance to the insert is 580 mm and 630 mm respectively. The fluid domain of the simulations ends 102 mm or ten times the tube diameter after the insert. When approaching this from flow development theory, Equation 3.33 dictates that at Reynolds number $Re \approx 10000$ the length after which the flow is fully developed, for a tube with diameter 10.2 mm, is 138.6 mm. This implies that the effect of the insert on the flow has already been neutralized

by the time the flow reaches sensor PCB2. For further research into the use of TPMS inserts as flow altering devices, this is an important factor to consider.

Furthermore, another factor that may contribute to the poor agreement between simulation and experiment is the simplified Darcy-Forcheimer model for flow through TPMS inserts. While for exceedingly small unit cell sizes, the TPMS inserts behave more and more like a general porous medium, it is unknown what the effect is of the geometrical features of the TPMS inserts at larger unit cell sizes. To illustrate this concept, consider that the feature size of the swirls exiting the TPMS insert, as shown in Figure 7.8 are directly proportional to the unit cell size α. At a unit cell size $\alpha = 2$ mm, the feature size of these swirls is in the range of millimeters as well. But because of the non-linear nature of fluid dynamics problems, no conclusive statements can be made about the potential performance of TPMS inserts at different unit cell sizes.

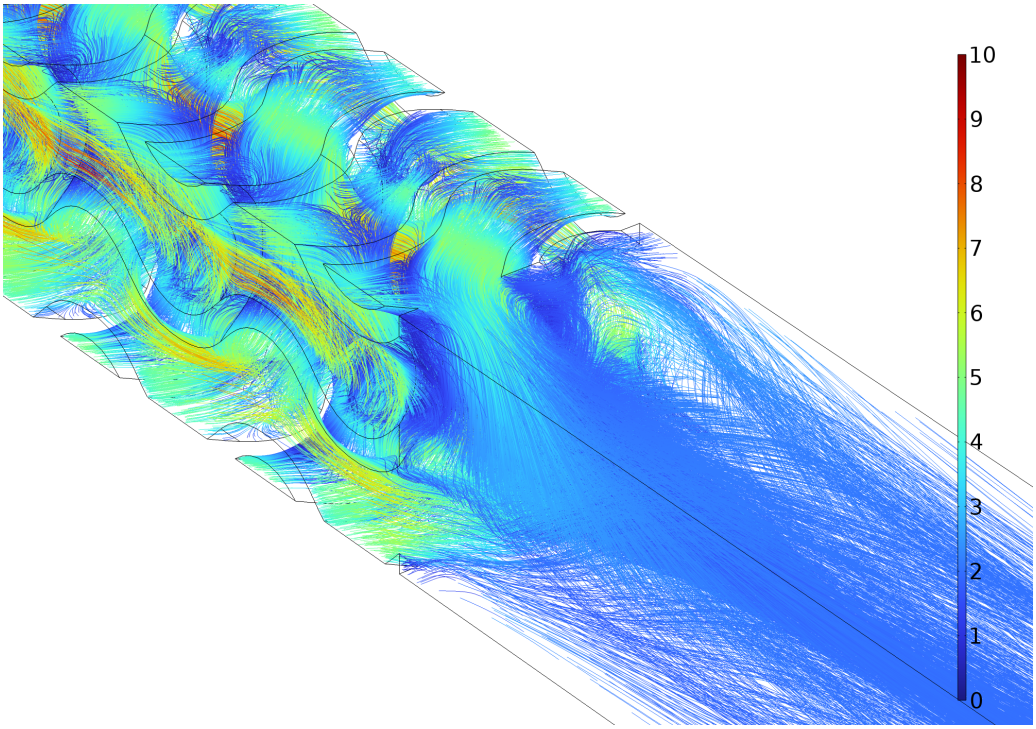

Figure 7.8: Streamline velocity plot of the unit cell scale simulation of the SG Sheet geometry at a relative density $D_{rel} = 30$ %.

Chapter 8

Conclusions and Outlook

8.1 Conclusions

The aim of this research project was to reduce the presence of flow induced vibrations (FIV) in high-tech industrial applications by leveraging metamaterials concepts. A class of metamaterials known as triply periodic minimal surfaces (TPMS) was chosen because of their inherent properties and excellent configurability.

Recognizing the computational challenges posed by the simulation of fluid flow through a large three-dimensional array of TPMS unit cells, a model based on the Darcy-Forcheimer equation was proposed. Unit cell scale simulations were conducted to derive the relevant parameters for the Darcy-Forcheimer model. Larger scale simulations were subsequently performed to evaluate the performance of TPMS inserts for the mitigation of FIV originating from sudden expansions.

The simulations revealed that TPMS are excellent candidate geometries for the mitigation of FIV, as a reduction of around 81% in terms of turbulent kinetic energy κ and a reduction of 12.5 % in terms of vorticity $\vec{\omega}$ were observed.

To validate the findings of the CFD simulations, two sets of experiments were set up. The first set of experiments focused on validating the Darcy-Forcheimer model for flow through porous media by placing a TPMS insert in a straight tube and determining the pressure drop over caused by the insert. The second set of experiments focused on the investigation of the TPMS inserts' ability to reduce the presence of FIV.

The data for the first set of experiments was contradictory, where one of the geometries yielded a significantly higher pressure drop than expected, while the other geometry yielded a significantly lower pressure drop than expected. In order to conclusively validate the Darcy-Forcheimer model, further investigation would be necessary.

In the second set of experiments, the recorded hydrodynamic pressure fluctuations and acoustic pressure fluctuations showed that the TPMS inserts did not significantly alter the presence of FIV as would have been expected from the simulations.

In light of these findings, it is evident that the journey toward comprehensively understanding the the interaction between TPMS and FIV is still ongoing. The complexities uncovered in this study open new avenues for exploring the relationship between metamaterials and fluid dynamics, paving the way for innovative solutions in the realm of FIV mitigation in high-tech industrial applications.

8.2 Outlook

The present work has provided crucial insights into the potential of TPMS for mitigation of FIV in high-tech industrial applications. However, several avenues for future exploration and refinement emerge from the study.

Refinement of the Darcy-Forcheimer Model

The contradictory results observed in the experiments validating the Darcy-Forcheimer model underscore the need for a more comprehensive understanding. Future research should focus on refining the model and addressing factors that may contribute to the unexpected pressure drop variations, ensuring its robustness and accuracy.

Optimization of TPMS Configurations

Exploring a broader range of TPMS configurations, geometries and gradings, as demonstrated in Figure 8.1, could enhance our understanding of the structures that exhibit optimal FIV mitigation. Systematic experimentation and computational parametric studies will contribute to identifying TPMS designs that are most effective.

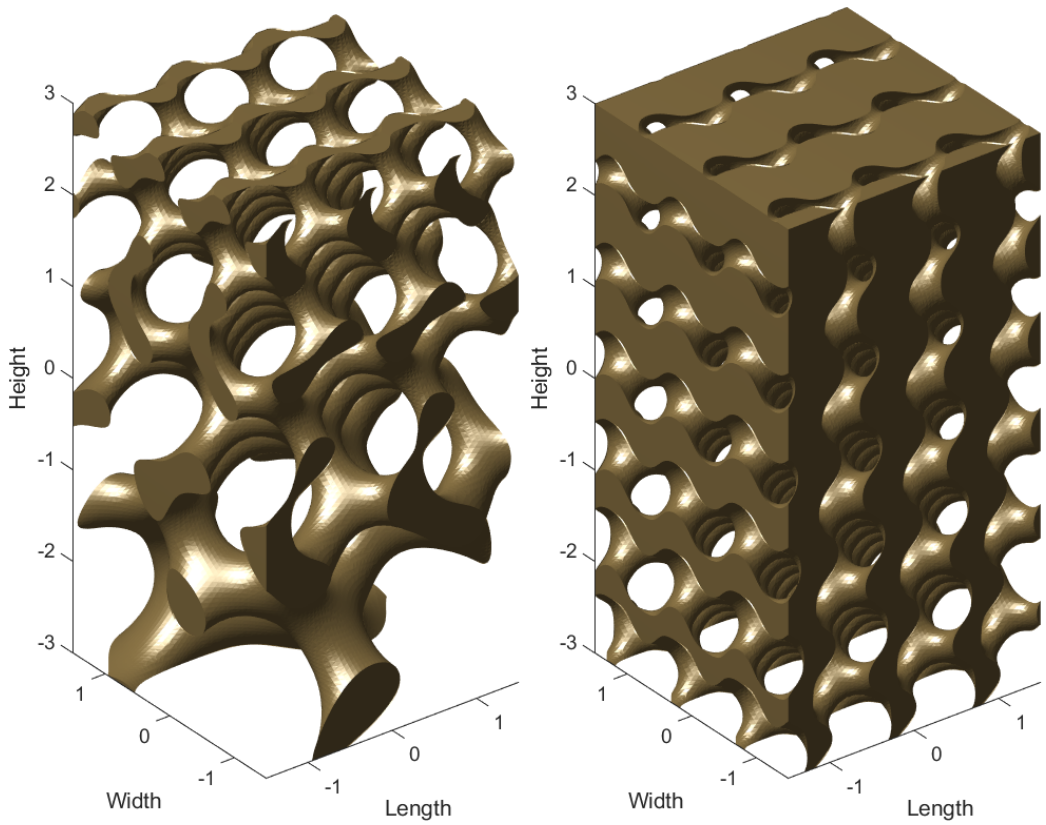

Figure 8.1: Examples of (a) cell size graded and (b) density graded SG Solid TPMS geometry.

Multi-Physics Simulations

Integrating multi-physics simulations that consider fluid-structure interactions and acoustic characteristics can provide a more holistic understanding of the complex interplay between TPMS structures and FIV. This approach will contribute to refining predictive models and bridging the gap between simulations and experiments.

In conclusion, the outlook for TPMS in FIV mitigation holds significant potential for advancing both scientific understanding and practical applications. Addressing the outlined challenges and pursuing avenues for further research will contribute to the development of robust, reliable, and scalable solutions for minimizing the impact of FIV in high-tech industrial settings.

Bibliography

[1] M.T. Pittard, R.P. Evans, R.D. Maynes, and J.D. Blotter. Experimental and numerical investigation of turbulent flow induced pipe vibration in fully developed flow. *Review of Scientific Instruments*, 75(7):2393–2401, 2004. doi: 10.1063/1.1763256.

[2] S. Kottapalli, R. van de Meerendonk, N. Waterson, G Nakiboglu, A. Hirschberg, and D.M.J. Smeulders. Analytical modelling and experimental validation of compliance-based low-frequency resonators for water circuits. *Acta Acust.*, 6:56, 2022. doi: 10.1051/aacus/2022050.

[3] R.D. Blevins. *Flow-induced vibration*. Van Nostrand Reinhold New York, New York, 1st edition, 1977. ISBN 0442206518; 9780442206512.

[4] T. Nakamura, N.W. Mureithi, and M.A. Langthjem. *Flow-induced vibrations: Classifications and lessons from practical experiences*. Academic Press, 2016.

[5] D. Scarselli, J. Kühnen, and B. Hof. Relaminarising pipe flow by wall movement. *Journal of Fluid Mechanics*, 867:934–948, 2019. doi: 10.1017/jfm.2019.191.

[6] J. Kühnen, D. Scarselli, M. Schaner, and B. Hof. Relaminarization by steady modification of the streamwise velocity profile in a pipe. *Flow, Turbulence and Combustion*, 100(4):919–943, Jun 2018. ISSN 1573-1987. doi: 10.1007/s10494-018-9896-4.

[7] M. Kotsonis. Diagnostics for characterisation of plasma actuators. *Measurement Science and Technology*, 26(9):092001, aug 2015. doi: 10.1088/0957-0233/26/9/092001.

[8] T.C. Corke, C.L. Enloe, and S.P. Wilkinson. Dielectric barrier discharge plasma actuators for flow control. *Annual Review of Fluid Mechanics*, 42(1):505–529, 2010. doi: 10.1146/annurev-fluid-121108-145550.

[9] J. Gregory and M. Tomac. A review of fluidic oscillator development and application for flow control. *43rd Fluid Dynamics Conference*, 06 2013. doi: 10.2514/6.2013-2474.

[10] H. Li, T. Kondoh, P. Jolivet, K. Furuta, T. Yamada, B. Zhu, K. Izui, and S. Nishiwaki. Three-dimensional topology optimization of a fluid–structure system using body-fitted mesh adaption based on the level-set method. *Applied Mathematical Modelling*, 101:276–308, 2022. ISSN 0307-904X. doi: 10.1016/j.apm.2021.08.021.

[11] Bo Nordell. Highly turbulent flow laminarized by hairy pipe walls. *International Journal of Mechanical Engineering and Applications*, 3:63, 2015. doi: 10.11648/j.ijmea.20150304.13.

[12] K.B. Golovin, J.W. Gose, M. Perlin, S.L. Ceccio, and A. Tuteja. Bioinspired surfaces for turbulent drag reduction. *Philosophical Transactions of the Royal Society A: Mathematical, Physical and Engineering Sciences*, 374(2073):20160189, 2016. doi: 10.1098/rsta.2016.0189.

[13] A. Rios-Rodriquez, C. Palacios-Morales, E. Bernal, G. Ascanio, and J. Aguayo-Vallejo. Effect of hydrophobic coating on hagen-poiseuille flows. *Journal of Applied Fluid Mechanics*, 9:1035–1040, 05 2016. doi: 10.18869/acadpub.jafm.68.228.24586.

[14] E.C. Chan and F.S. Lien. Permeability effects of turbulent flow through a porous insert in a backward-facing-step channel. *Transport in Porous Media*, 59(1):47–71, Apr 2005. ISSN 1573-1634. doi: 10.1007/s11242-004-1120-4.

[15] O. Al-Ketan and R.K. Abu Al-Rub. Multifunctional mechanical metamaterials based on triply periodic minimal surface lattices. *ADVANCED ENGINEERING MATERIALS*, 21(10), 2019. doi: 10.1002/adem.201900524.

[16] Y Jung and S Torquato. Fluid permeabilities of triply periodic minimal surfaces. *PHYSICAL REVIEW E*, 72(5, 2), 2005. doi: 10.1103/PhysRevE.72.056319.

[17] M.P. do Carmo. *Differential geometry of curves and surfaces.* Prentice Hall, 1976. ISBN 978-0-13-212589-5.

[18] J. Feng, J. Fu, X. Yao, and Y. He. Triply periodic minimal surface (TPMS) porous structures: from multi-scale design, precise additive manufacturing to multidisciplinary applications. *International Journal of Extreme Manufacturing*, 4(2):022001, June 2022. doi: 10.1088/2631-7990/ac5be6.

[19] L. Yuan, S. Ding, and C. Wen. Additive manufacturing technology for porous metal implant applications and triple minimal surface structures: A review. *BIOACTIVE MATERIALS*, 4:56–70, 2019. doi: 10.1016/j.bioactmat.2018.12.003.

[20] O. Al-Ketan and R.K. Abu Al-Rub. Mslattice: A free software for generating uniform and graded lattices based on triply periodic minimal surfaces. *Material Design & Processing Communications*, 3(6):e205, 2021. doi: 10.1002/mdp2.205. e205 MDPC-2020-042.R1.

[21] Z. Dong and X. Zhao. Application of tpms structure in bone regeneration. *Engineered Regeneration*, 2:154–162, 2021. ISSN 2666-1381. doi: 10.1016/j.engreg.2021.09.004.

[22] C. Yan, L. Hao, A. Hussein, and P. Young. Ti-6al-4v triply periodic minimal surface structures for bone implants fabricated via selective laser melting. *J Mech Behav Biomed Mater*, 51:61–73, jul 2015.

[23] C. Karuna, T. Poltue, S. Khrueaduangkham, and P. Promoppatum. Mechanical and fluid characteristics of triply periodic minimal surface bone scaffolds under various functionally graded strategies. *Journal of Computational Design and Engineering*, 9(4):1258–1278, 06 2022. ISSN 2288-5048. doi: 10.1093/jcde/qwac052.

[24] A.M. Genç, C. Vatansever, M. Koçak, and Z.H. Karadeniz. Investigation of additively manufactured triply periodic minimal surfaces as an air-to-air heat exchanger. *CLIMA 2022 conference*, May 2022. doi: 10.34641/clima.2022.172.

[25] W. Li, G. Yu, and Z. Yu. Bioinspired heat exchangers based on triply periodic minimal surfaces for supercritical co2 cycles. *Applied Thermal Engineering*, 179:115686, 2020. ISSN 1359-4311. doi: 10.1016/j.applthermaleng.2020.115686.

[26] B.R. Munson, D.F. Young, T.H. Okiishi, and W.W. Huebsch. *Fundamentals of Fluid Mechanics*. Wiley, 6th edition, 2009. ISBN 9780470418253.

[27] F. Irgens. *Continuum mechanics*. Springer, 2008. ISBN 9783540742975.

[28] S. Shelley, R. Sambles, A. Hibbins, and S. Horsley. *The control of fluid flow using metamaterial concepts*. PhD thesis, University of Exeter, 2018.

[29] L.D. Landau and E.M. Lifshitz. *Fluid Mechanics*. Butterworth-Heinemann, 2nd edition, 1987. ISBN 0750627670.

[30] K. Avila, D. Moxey, A. de Lozar, M. Avila, D. Barkley, and B. Hof. The onset of turbulence in pipe flow. *Science*, 333(6039):192–196, 2011. doi: 10.1126/science.1203223.

[31] E. Fonda and K.R. Sreenivasan. Unmixing demonstration with a twist: A photochromic taylor-couette device. *American Journal of Physics*, 85(10):796–800, 2017. doi: 10.1119/1.4996901.

[32] A. Kalpakli Vester, R. Örlü, and P.H. Alfredsson. Turbulent Flows in Curved Pipes: Recent Advances in Experiments and Simulations. *Applied Mechanics Reviews*, 68(5):050802, 09 2016. ISSN 0003-6900. doi: 10.1115/1.4034135.

[33] Y.A. Çengel and J.M. Cimbala. *Fluid mechanics : fundamentals and applications*. McGraw-Hill Education New York, NY, New York, NY, 4th edition, 2018. ISBN 9781259696534; 1259696537; 9781259921902; 1259921905.

[34] T.L. Bergman, A.S. Lavine, F.P. Incropera, and D.P. Dewitt. *Introduction to heat transfer*. Wiley Hoboken, NJ, Hoboken, NJ, 5th edition, 2011. ISBN 9780470501962; 0470501960.

[35] B.E. Launder and D.B. Spalding. The numerical computation of turbulent flows. *Computer Methods in Applied Mechanics and Engineering*, 3(2):269–289, 1974. ISSN 0045-7825. doi: 10.1016/0045-7825(74)90029-2.

[36] Comsol documentation, 2023. URL `https://doc.comsol.com/6.2/docserver/#!/com.comsol.help.comsol/helpdesk/helpdesk.html`.

[37] R. Asbai-Ghoudan, S. Ruiz de Galarreta, and N. Rodriguez-Florez. Analytical model for the prediction of permeability of triply periodic minimal surfaces. *Journal of the Mechanical Behavior of Biomedical Materials*, 124:104804, 2021. ISSN 1751-6161. doi: 10.1016/j.jmbbm.2021.104804.

[38] S.S. Rathore, B. Mehta, P. Kumar, and M. Asfer. Flow characterization in triply periodic minimal surface (tpms)-based porous geometries: Part 1—hydrodynamics. *Transport in Porous Media*, 146(3):669–701, Feb 2023. ISSN 1573-1634. doi: 10.1007/s11242-022-01880-7.

[39] P. Kundu, V. Kumar, and I.M. Mishra. Experimental and numerical investigation of fluid flow hydrodynamics in porous media: Characterization of pre-darcy, darcy and non-darcy flow regimes. *Powder Technology*, 303:278–291, 2016. ISSN 0032-5910. doi: 10.1016/j.powtec.2016.09.037.

[40] 2023. URL https://o-ring.info/en/technical%20manual/eriks%20-%20technical%20manual%20-%20o-ring%20gland%20design%20information.pdf.

A Prerequisites to the Derivation of Navier-Stokes

A.1 Material Derivative

The Eulerian derivative is defined as the rate of change of a quantity (e.g. velocity, pressure or temperature) at a fixed position in space. The Lagrangian or material derivative is defined as the rate of change of a quantity in a reference frame that follows a small volume of fluid. The concerning quantity, which could be e.g. pressure, velocity or temperature is henceforth labeled as $\boldsymbol{f}$. Consider a fluid particle moving along a path in a fluid. In general, the velocity of the particle is a function of time and its position in space. Suppose that the particle p is located at position x at time t and a short while later it has moved to position $x + \partial x$ at time $t + \partial t$. The change in quantity $\boldsymbol{f}[x_1(t), x_2(t), x_3(t), t]$ is defined as

$$\partial \boldsymbol{f} = \boldsymbol{f}(x + \partial x, t + \partial t) - \boldsymbol{f}(x, t). \tag{A.1}$$

In order to arrive at the rate of change with respect to time of quantity $\boldsymbol{f}$, one must divide by ∂t and take the limit as $\partial t \to 0$

$$\frac{D\boldsymbol{f}}{Dt} = \lim_{\partial t \to 0} \frac{\boldsymbol{f}(x + \partial x, t + \partial t) - \boldsymbol{f}(x, t)}{\partial t}, \tag{A.2}$$

where $\frac{D}{Dt}$ is the material derivative operator. Expanding this out to the three-dimensional case, it becomes

$$\frac{D\boldsymbol{f}}{Dt} = \frac{\partial x_1}{\partial t}\frac{\partial \boldsymbol{f}}{\partial x_1} + \frac{\partial x_2}{\partial t}\frac{\partial \boldsymbol{f}}{\partial x_2} + \frac{\partial x_3}{\partial t}\frac{\partial \boldsymbol{f}}{\partial x_3} + \frac{\partial \boldsymbol{f}}{\partial t}, \tag{A.3}$$

where one can notice that $\frac{\partial x_1}{\partial t}$, $\frac{\partial x_2}{\partial t}$ and $\frac{\partial z}{\partial t}$ are simply the fluid velocity for the three-dimensional case defined as v_1, v_2 and v_3 respectively. Simplifying the equation to

$$\frac{D\boldsymbol{f}}{Dt} = v_1\frac{\partial \boldsymbol{f}}{\partial x_1} + v_2\frac{\partial \boldsymbol{f}}{\partial x_2} + v_3\frac{\partial \boldsymbol{f}}{\partial x_3} + \frac{\partial \boldsymbol{f}}{\partial t}. \tag{A.4}$$

Which is simplified to

$$\frac{D\boldsymbol{f}}{Dt} = \frac{\partial \boldsymbol{f}}{\partial t} + (\boldsymbol{v} \cdot \nabla)\boldsymbol{f}, \tag{A.5}$$

where ∇ is the gradient operator $\frac{\partial}{\partial x_1} + \frac{\partial}{\partial x_2} + \frac{\partial}{\partial x_3}$ and $(\boldsymbol{v} \cdot \nabla)$ is the dot product of the velocity vector $\boldsymbol{v}$ and the gradient operator ∇. The material derivative is a useful quantity in the analysis of fluid parameters, not just for the intuitive case of velocities and accelerations, but also for e.g. temperature and pressure and their respective rates of change with respect to time and location in three-dimensional space.

A.2 Cauchy's Stress Tensor

Consider a small volume of fluid which exerts a force to its surrounding area, normal to the surface of the volume. The force that is exerted by the volume can be written as

$$\boldsymbol{F} = t\boldsymbol{n}S = \boldsymbol{t}S, \tag{A.6}$$

where $\boldsymbol{t}$ is the force per unit area, or stress and S is the surface area of the volume. In the case of an infinitesimally small volume, we define the force $\partial \boldsymbol{F} = \boldsymbol{t}\partial S$. The force, however, does not have to be normal to the surface of the volume such that $\boldsymbol{t} \neq t\boldsymbol{n}$. It is therefore useful to define a stress tensor σ which allows for the presence of both normal forces and shear forces

$$\sigma = \begin{bmatrix} \sigma_{11} & \sigma_{12} & \sigma_{13} \\ \sigma_{21} & \sigma_{22} & \sigma_{23} \\ \sigma_{31} & \sigma_{32} & \sigma_{33} \end{bmatrix}, \tag{A.7}$$

where the the *i-th* component of σ_{ij} represents the stress on the surface which is normal to the *j-th* component of σ_{ij}. Subsequently, σ_{11}, σ_{22} and σ_{33} represent the normal forces exerted by the volume, and σ_{12}, σ_{13}, σ_{21}, σ_{23}, σ_{31} and σ_{32} represent the shear forces exerted by the volume as shown in Figure A.1.

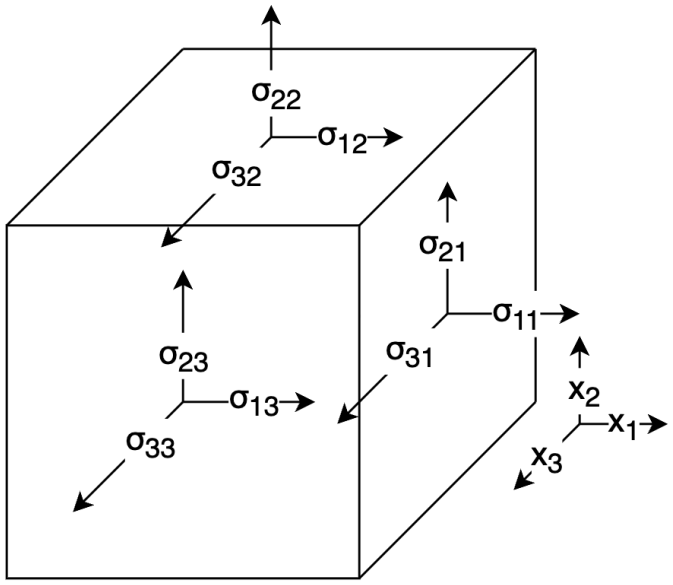

Figure A.1: Schematic overview of the stress tensor σ in Equation A.7

Subsequently, the total stress in the *i-th* direction is given by

$$t_i = \sum_j \sigma_{ij} n_j, \tag{A.8}$$

where n_j is a unit vector with direction *j*. Integrating, in order to obtain the total force in direction *j* results in

$$\int_S t_i dS = \int_S \sigma_{ij} n_j dS, \tag{A.9}$$

where $\int_S t_i dS$ is simply $\partial \boldsymbol{F}$. Using the divergence theorem, which states that the surface integral of a vector field over a closed surface is equal to the volume integral of the divergence over the region inside the surface, this becomes

$$\partial \boldsymbol{F} = \int_V \frac{\partial \sigma_{ij}}{\partial x_i} dV. \tag{A.10}$$

Under the assumption of a small volume V, the expression $\frac{\partial \sigma_{ij}}{\partial x_i}$ can be regarded as a constant resulting in

$$\partial \boldsymbol{F} = \frac{\partial \sigma_{ij}}{\partial x_i} V. \tag{A.11}$$

B Derivation Reynolds Number

In order to derive the Reynolds number from the Navier-Stokes equation in Equation 3.19, one must define the parameters characteristic length L and velocity U. From these, the following dimensionless parameters can be defined:

$$\hat{x} = \frac{x}{L} \qquad \hat{\boldsymbol{v}} = \frac{\boldsymbol{v}}{U} \qquad \tau = \frac{tU}{L} \qquad P = \frac{pL}{\mu U}. \tag{B.1}$$

Under the assumption that the body forces are zero, substituting these parameters in the Navier-Stokes equation results in:

$$\rho \left(\frac{U^2}{L} \frac{\partial}{\partial \tau} \hat{v}_i + \frac{U^2}{L} \left(\hat{v}_i \cdot \frac{\partial}{\partial \hat{x}_i} \right) \hat{v}_i \right) = -\frac{\mu U}{L^2} \frac{\partial}{\partial \hat{x}_i} P + \frac{\mu U}{L^2} \frac{\partial^2}{\partial \hat{x}_i^2} \hat{v}_i \tag{B.2}$$

From this, we divide by $\frac{\rho U^2}{L}$ to arrive at the dimensionless form of the Navier-Stokes equation:

$$\frac{\partial}{\partial \tau} \hat{v}_i + \left(\hat{v}_i \cdot \frac{\partial}{\partial \hat{x}_i} \right) \hat{v}_i = \frac{\mu}{\rho U L} \left(-\frac{\partial}{\partial \hat{x}_i} P + \frac{\partial^2}{\partial \hat{x}_i^2} \hat{v}_i \right). \tag{B.3}$$

The Reynolds number is defined as:

$$Re = \frac{\mu U L}{\rho}. \tag{B.4}$$

C TPMS Lattices

This appendix contains a schematic overview of the TPMS unit cells for both the solid-wise and sheet-wise geometries in Figure C.1 and Figure C.2 respectively. Additionally, Figure C.3 and Figure C.4 contain three by three by three constructed lattices for both the solid-wise and sheet-wise TPMS.

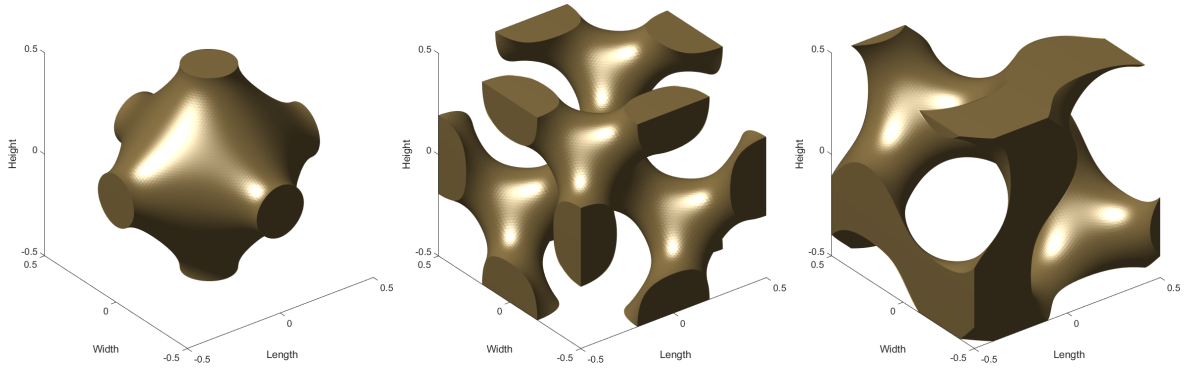

(a) Schwarz Primitive (SP) (b) Schwarz Diamond (SD) (c) Schoen Gyroid (SG)

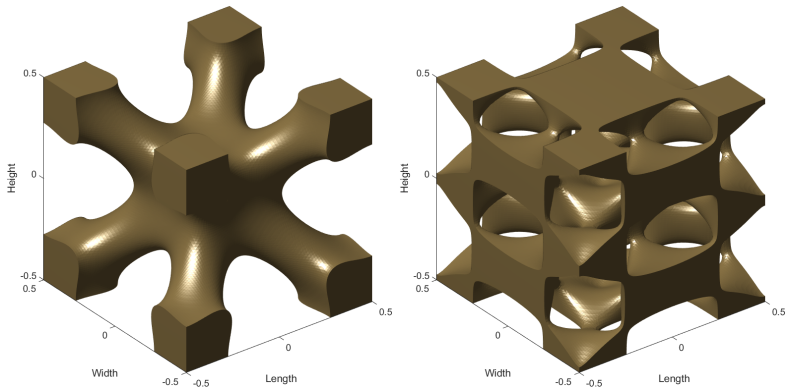

(d) Schoen I-Graph and Wrapped Package (IW-P) (e) Schoen F-Rhombic Dodecahedra (F-RD)

Figure C.1: Lattices consisting of nine unit cells, constructed from common sheet-wise TPMS with a relative density of 30%.

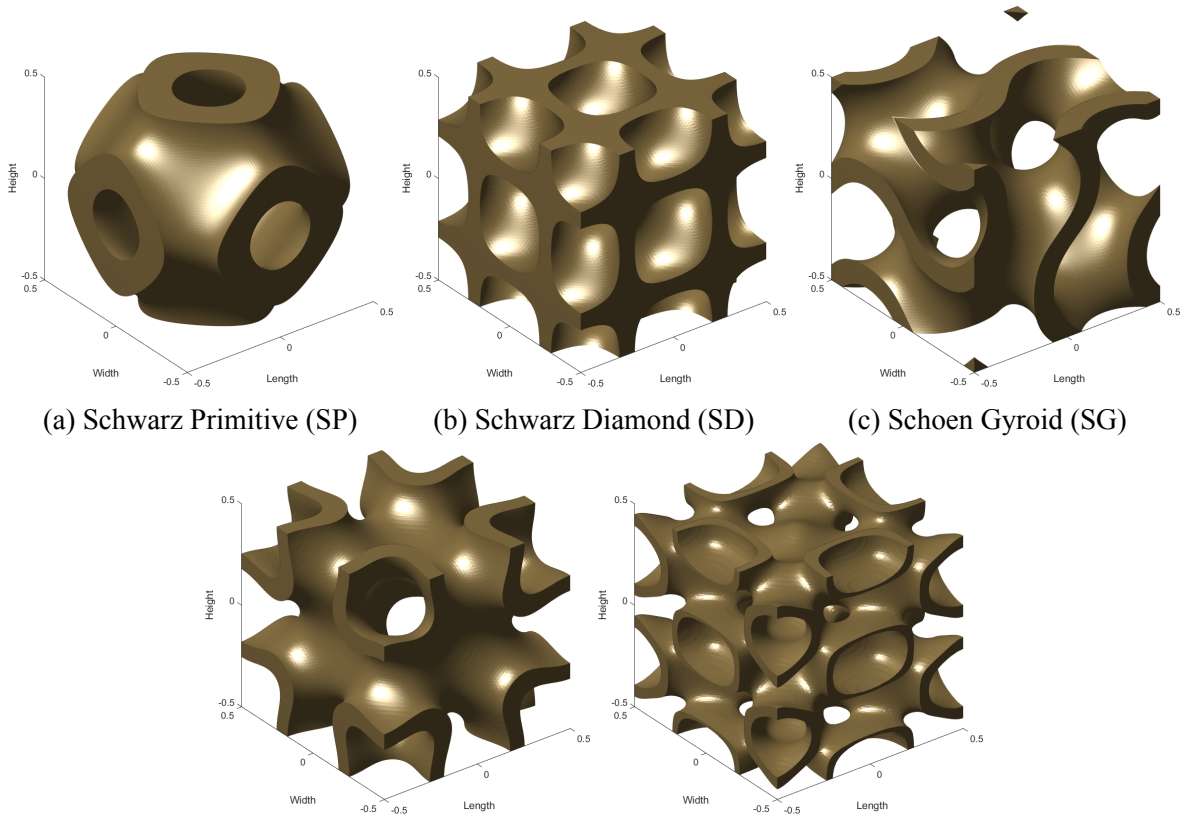

(a) Schwarz Primitive (SP) (b) Schwarz Diamond (SD) (c) Schoen Gyroid (SG)

(d) Schoen I-Graph and Wrapped Package (IW-P) (e) Schoen F-Rhombic Dodecahedra (F-RD)

Figure C.2: The unit cells of five of the commonly used sheet-wise TPMS lattices with a relative density of 30%.

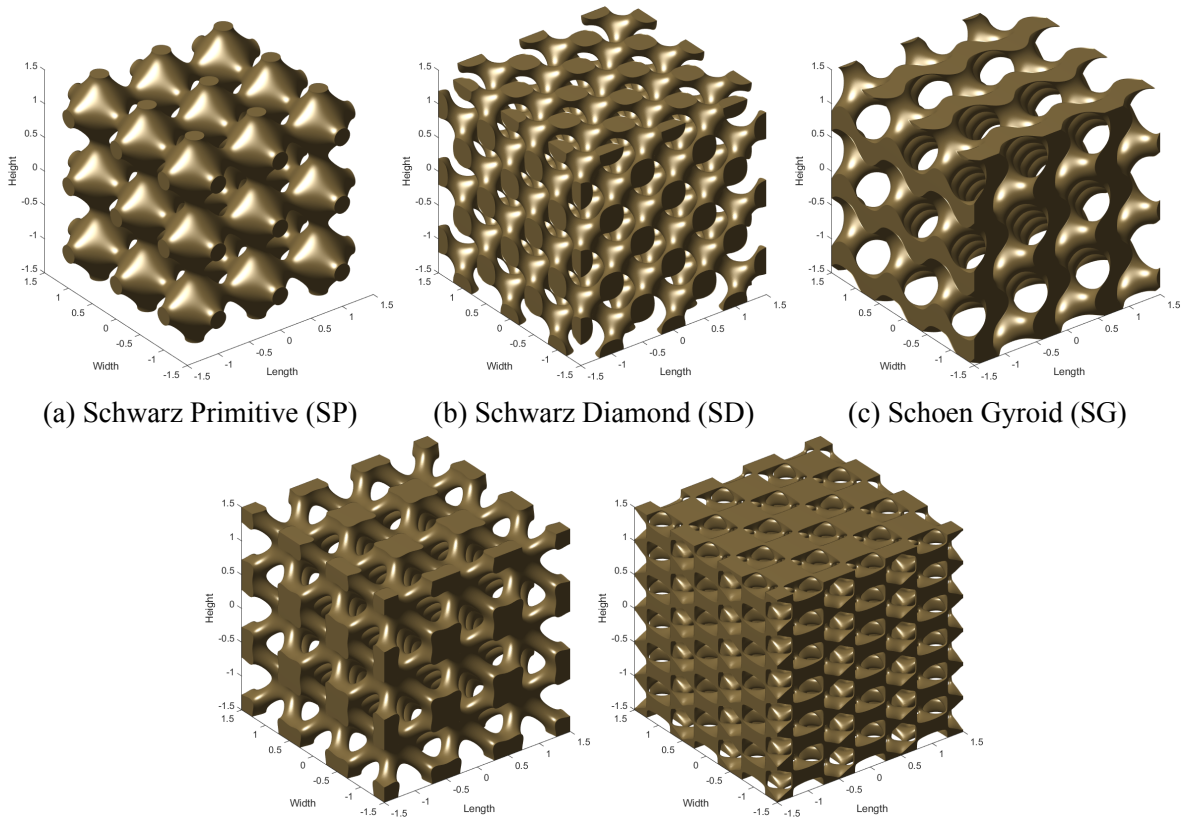

(a) Schwarz Primitive (SP) (b) Schwarz Diamond (SD) (c) Schoen Gyroid (SG)

(d) Schoen I-Graph and Wrapped Package (IW-P) (e) Schoen F-Rhombic Dodecahedra (F-RD)

Figure C.3: Lattices consisting of nine unit cells, constructed from common solid-wise TPMS with a relative density of 30%.

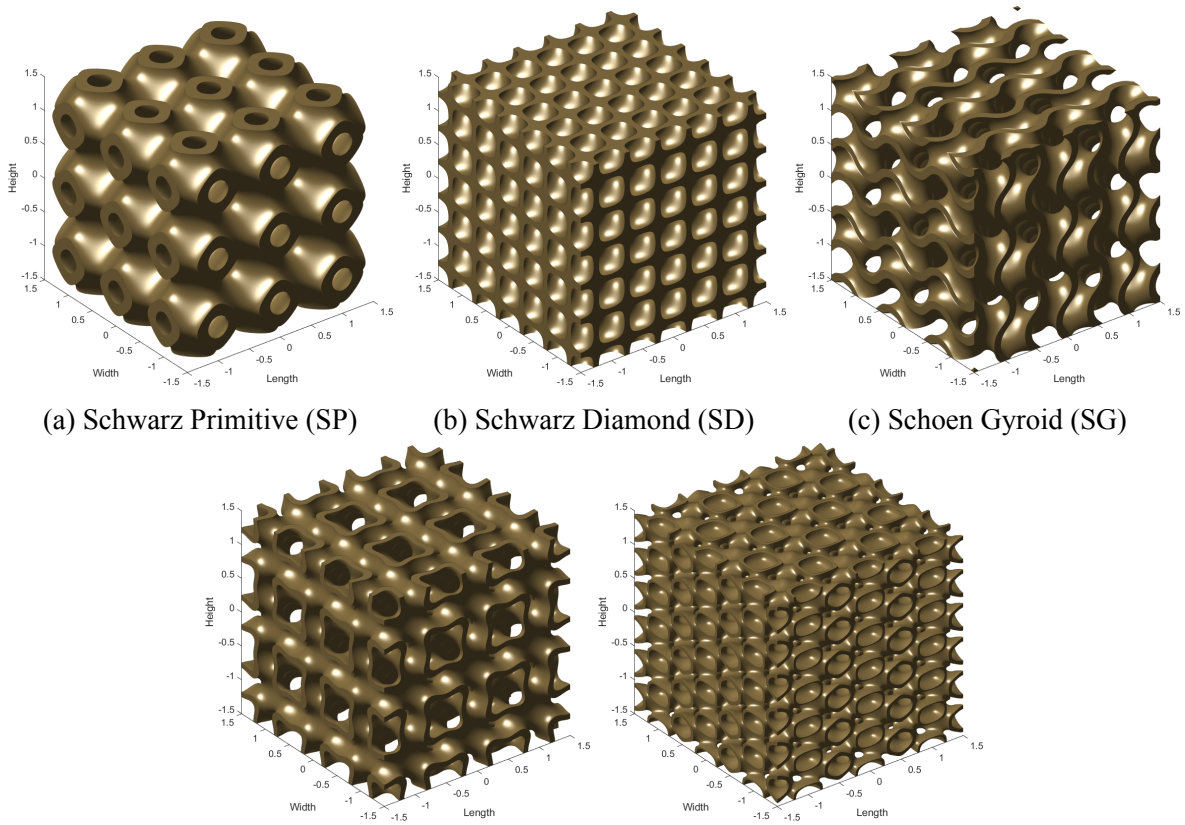

(a) Schwarz Primitive (SP) (b) Schwarz Diamond (SD) (c) Schoen Gyroid (SG)

(d) Schoen I-Graph and Wrapped Package (IW-P) (e) Schoen F-Rhombic Dodecahedra (F-RD)

Figure C.4: Lattices consisting of nine unit cells, constructed from common sheet-wise TPMS with a relative density of 30%.

D Evaluation of Other CFD Packages

Below is a short evaluation of other CFD software packages. For the reasons listed below, and the author's and project supervisor's familiarity with COMSOL Multifphysics, the choice was made to stick with COMSOL.

D.1 OpenFOAM

OpenFOAM, while having a steep learning curve proved to be a capable CFD software package. The most straight forward method for performing a CFD study in OpenFOAM is adapting one of the included tutorials. Using these tutorials, a simulation was made of a sudden expansion without and with a porous insert as shown in Figure D.1 and Figure D.2 respectively.

(a) Velocity plot

(b) Pressure plot

Figure D.1: Velocity and pressure plot for a sudden expansion without porous insert.

(a) Velocity plot

(b) Pressure plot

Figure D.2: Velocity and pressure plot a sudden expansion with a porous insert, 10 mm in length and a permeability K of $1 \cdot 10^{-9}$.

The porous insert has a significant effect on the fluid flow. One can observe that the porous insert causes a the formation of a significant pressure drop over the length of the insert. The results from this test showed promising results with regards to the simulation of porous media. Unfortunately, the unit cell-scale simulations were more difficult to implement. Several attempts were made to adapt an OpenFOAM tutorial in order to simulate the behaviour of fluid flow through unit cells. None of these attempts resulted in promising results. Subsequently, the choice was made to discontinue the evaluation of OpenFOAM.

D.2 Ansys Fluent

Ansys Fluent is a CFD software package that is widely used in industry as well as research. One of the articles that inspired this research also used Ansys Fluent for unit cell-scale simulations, which is why the choice was made to evaluate it. Unfortunately, the UG does not currently have licenses for Ansys Fluent, which is why the free student license was used. Unfortunately, this immediately proved to be problematic, as the free student license is limited in the number of mesh elements that can be used. At the maximum number of mesh elements, in none of the attempts to simulate simple systems would the model converge. Subsequently, the choice was made to discontinue the evaluation of Ansys Fluent.

E Images of FDM Unit Cells

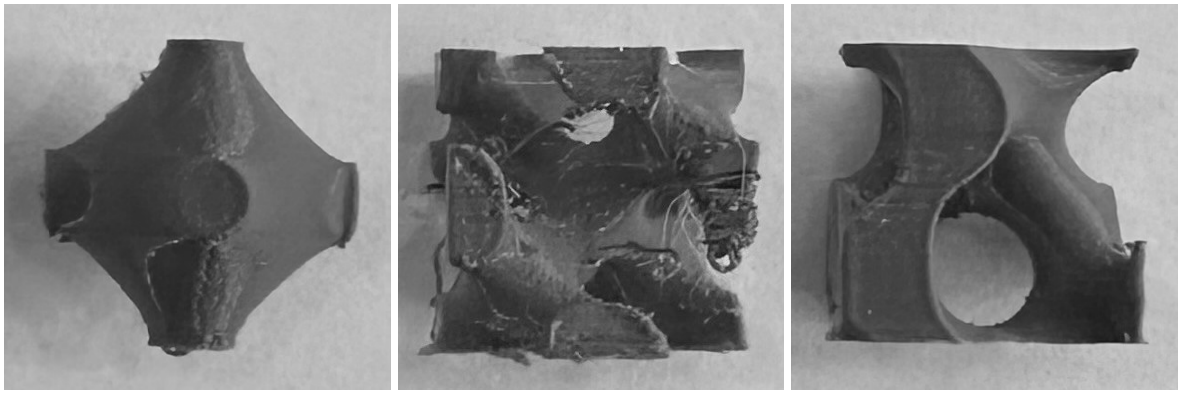

(a) SP Solid (b) SD Solid (c) SG Solid

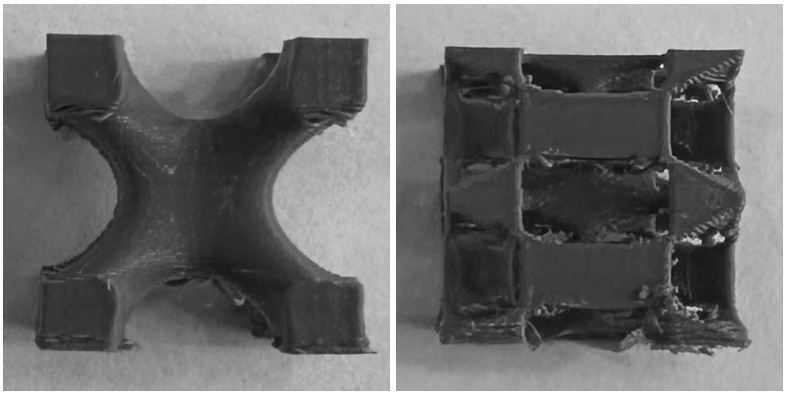

(d) IW-P Solid (e) F-RD Sheet

Figure E.1: FDM 2cm unit cell prints for the (a) SD Solid, (b) SD Solid, (c) SG Solid, (d) IW-P Solid and the (e) F-RD Solid.

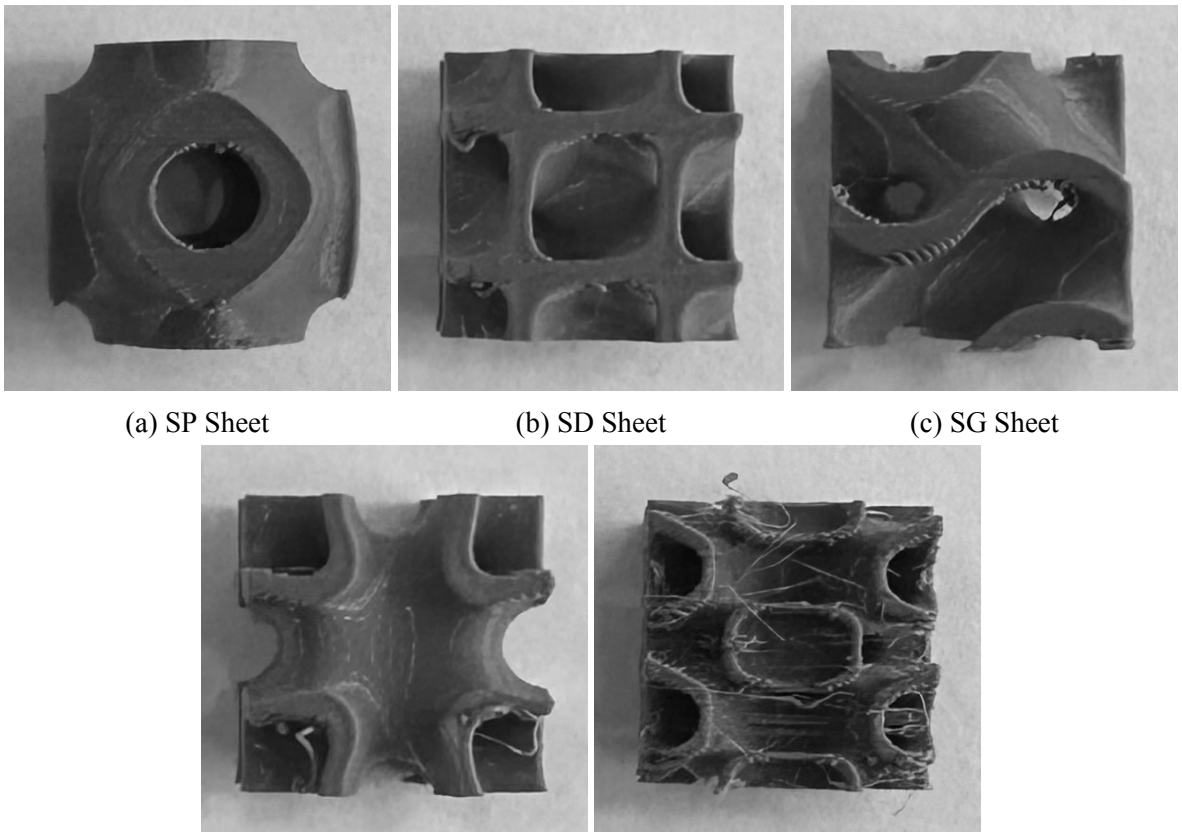

(a) SP Sheet (b) SD Sheet (c) SG Sheet

(d) IW-P Sheet (e) F-RD Sheet

Figure E.2: FDM 2cm unit cell prints for the (a) SD Sheet, (b) SD Sheet, (c) SG Sheet, (d) IW-P Sheet and the (e) F-RD Sheet.

F Technical Drawings of the Experimental Set-Up

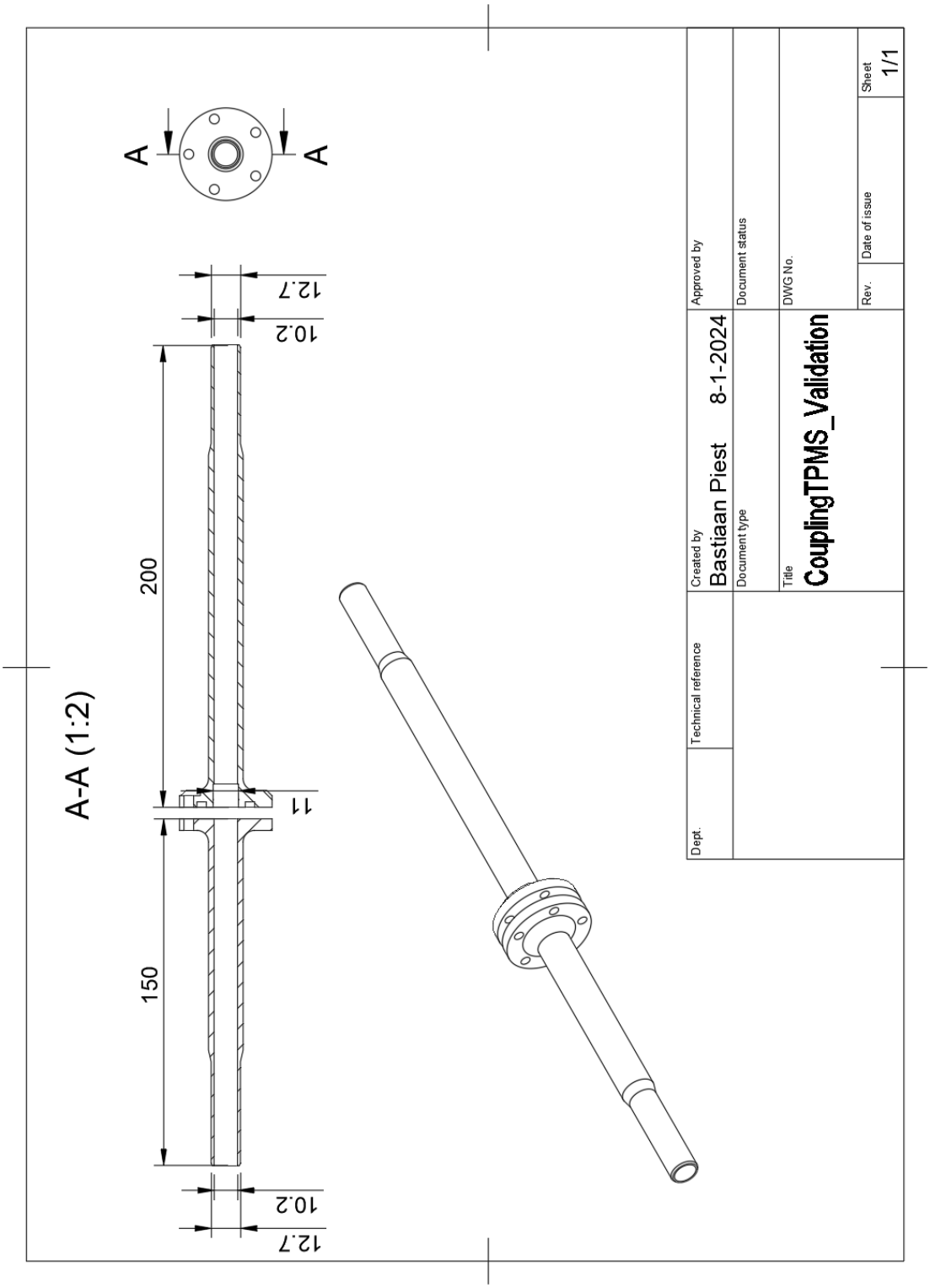

Figure F.1: Technical drawing of the straight tube experimental set-up with some important dimensions.

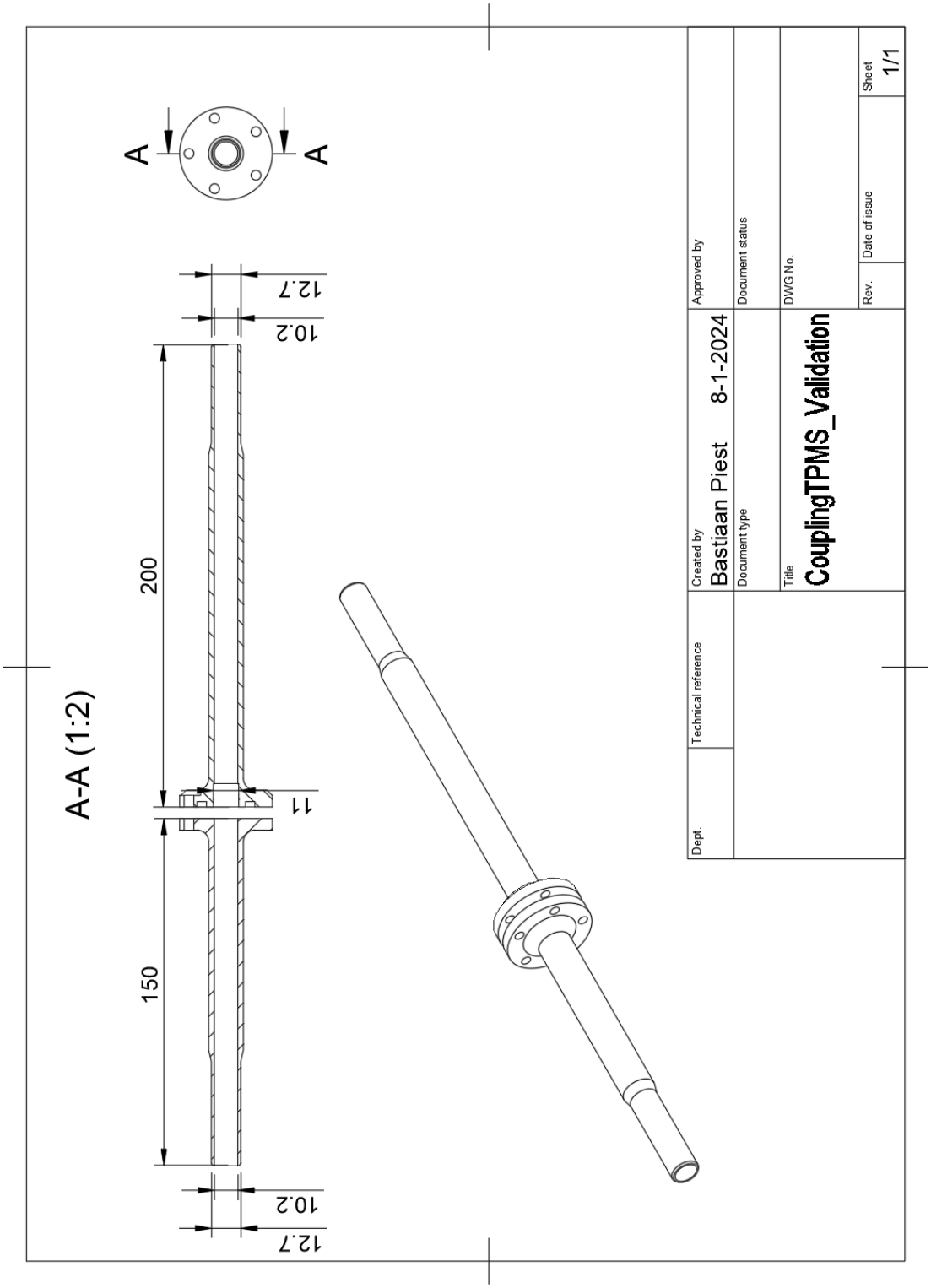

Figure F.2: Technical drawing of the sudden expansion experimental set-up with some important dimensions.

G Detailed Photos of the Experimental Set-Up

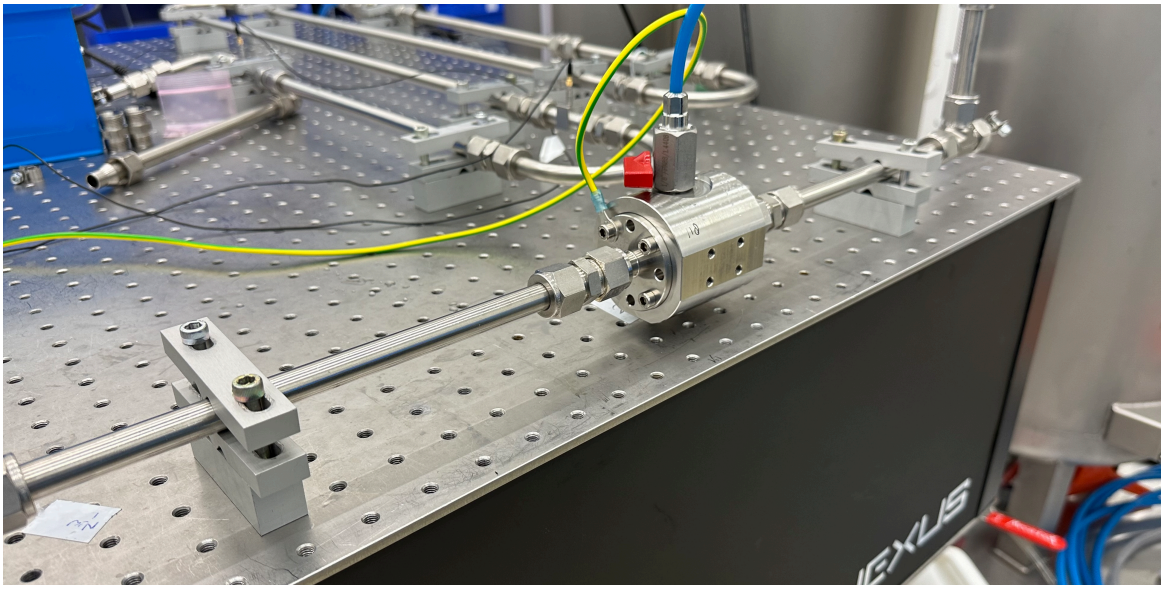

Figure G.1: Photo of the pressure tap and the Kistler 7261 piezoelectric low pressure sensor (K1) on the inlet side of the experiment.

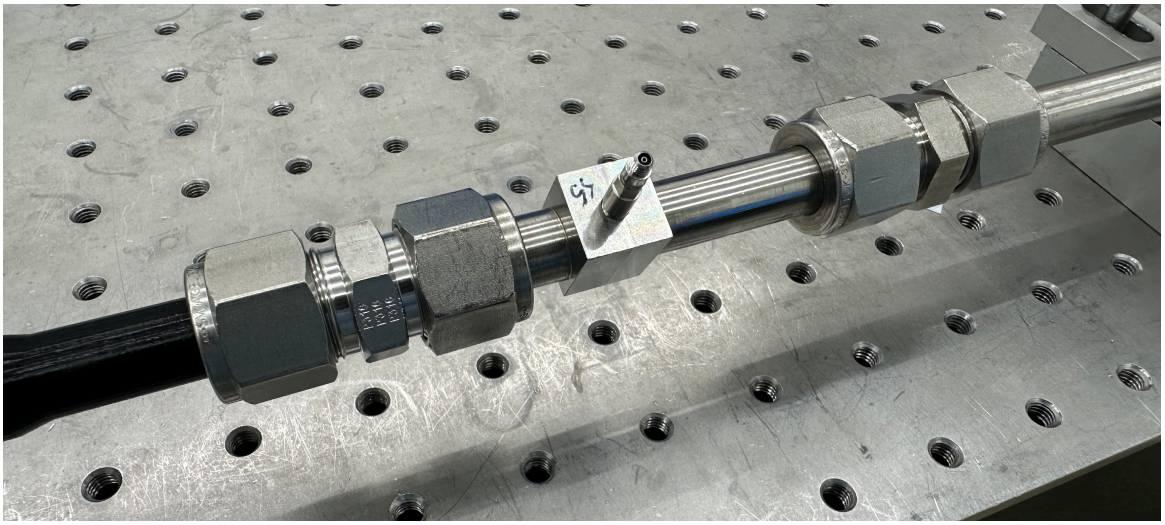

Figure G.2: Photo of the PCB Piezotronics 105C02 ICP pressure sensor (PCB1) on the inlet side of the experiment.

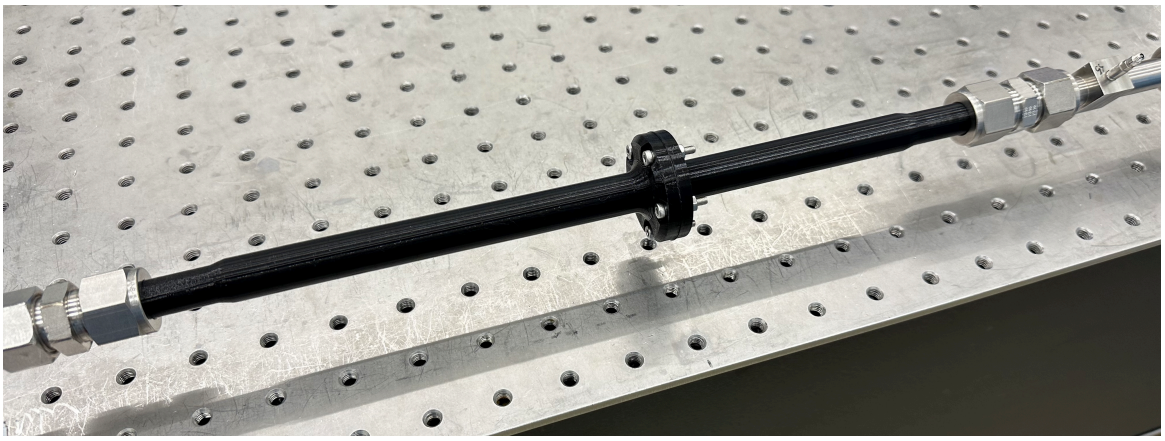

Figure G.3: Photo of the additively manufactured experimental set-up in-situ.

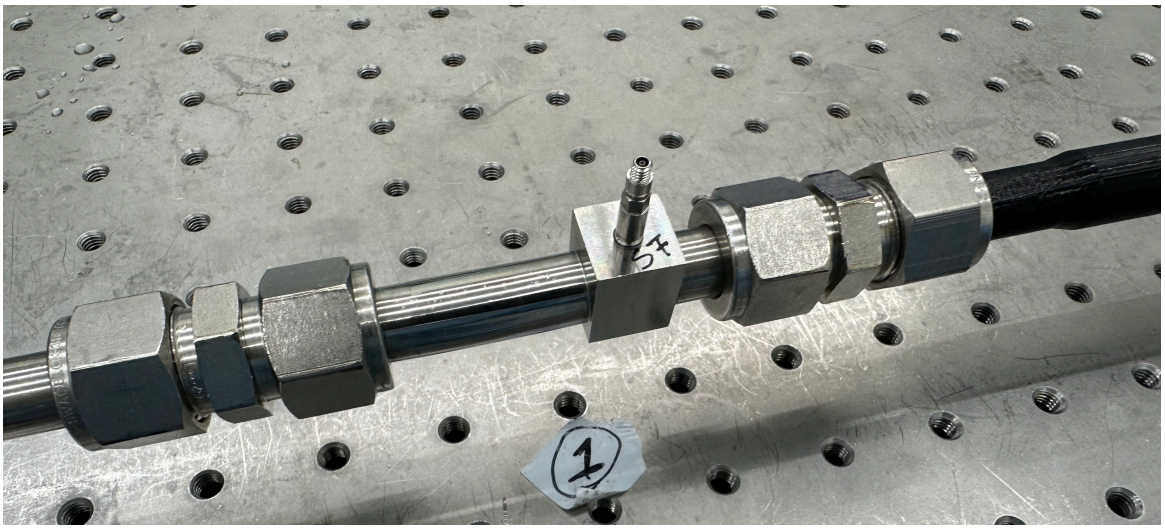

Figure G.4: Photo of the PCB Piezotronics 105C02 ICP pressure sensor (PCB2) on the outlet side of the experiment.

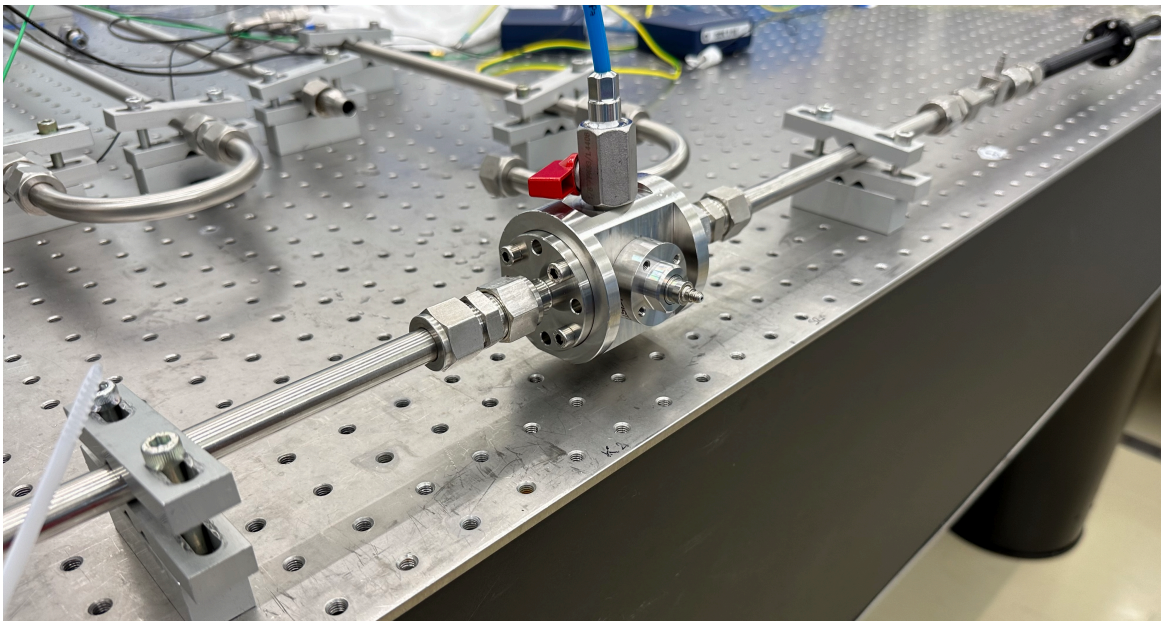

Figure G.5: Photo of the Kistler 7261 piezoelectric low pressure sensor (K2) on the outlet side of the experiment.

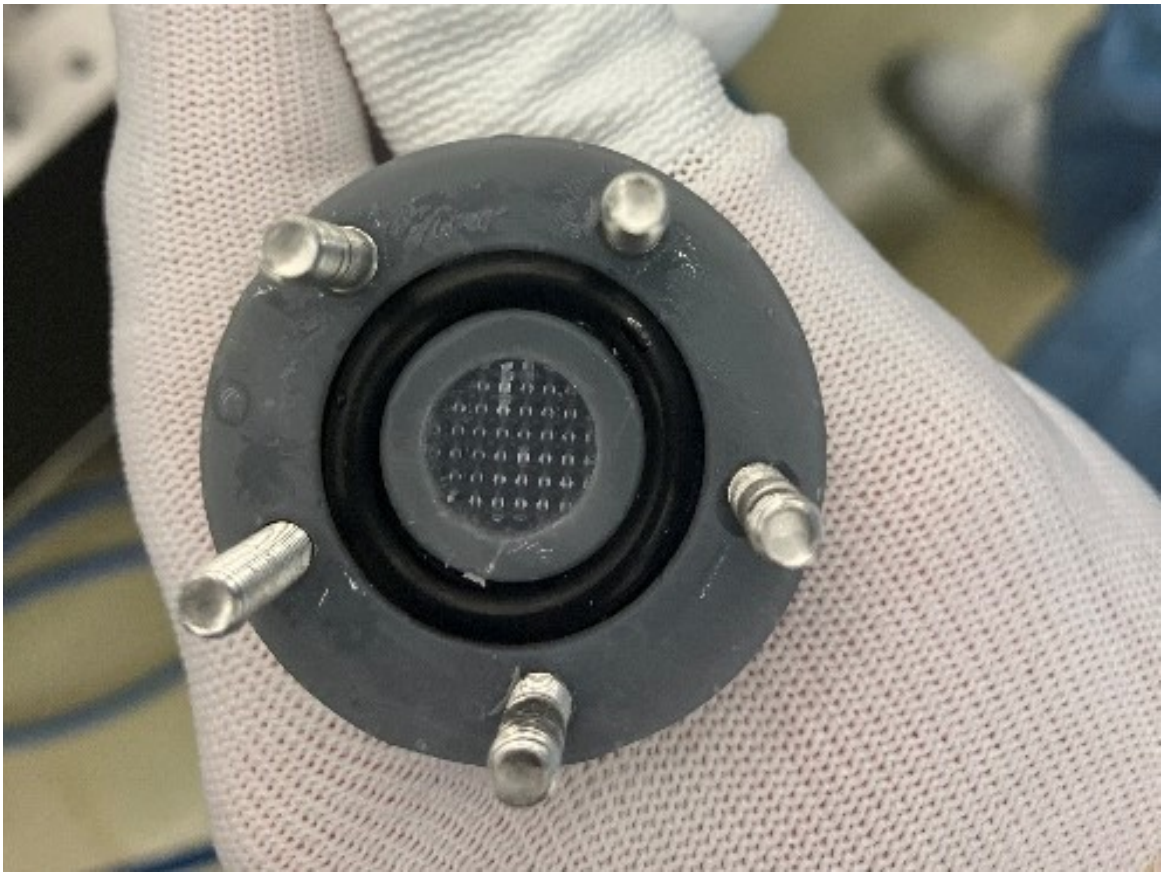

Figure G.6: Photo of one of the inserts placed inside the experimental set-up

H CFD Pressure Drop Data

H.1 Recorded Pressure Data Simulations

Table H.1: CFD pressure drop (Pa) data for the unit cell-size simulations of the SP TPMS.

1mm unit cell	SP Sheet				2mm unit cell	SP Sheet			
Relative Density	20 %	30 %	40 %	50 %	Relative Density	20 %	30 %	40 %	50 %
Velocity (m/s)	Pressure (Pa)	Pressure (Pa)	Pressure (Pa)	Pressure (Pa)	Velocity (m/s)	Pressure (Pa)	Pressure (Pa)	Pressure (Pa)	Pressure (Pa)
1.0	27543	61145	192784	1373005	1.0	23333	55241	177575	1273330
1.2	37793	84744	271241	1937265	1.2	32626	78049	251798	1792413
1.4	49597	112090	362494	2592543	1.4	43421	104556	338161	2414573
1.6	62984	143204	466608	3336731	1.6	55715	134676	436853	3134799
1.8.	77916	178228	583680	4181425	1.8.	69543	168456	544332	3946562
2.0	94384	217310	713084	5098104	2.0	84824	205905	664591	4856112
1mm unit cell	SP Solid				2mm unit cell	SP Solid			
Relative Density	20 %	30 %	40 %	50 %	Relative Density	20 %	30 %	40 %	50 %
Velocity (m/s)	Pressure (Pa)	Pressure (Pa)	Pressure (Pa)	Pressure (Pa)	Velocity (m/s)	Pressure (Pa)	Pressure (Pa)	Pressure (Pa)	Pressure (Pa)
1.0	Not Feasible	6252	13673	28575	1.0	Not Feasible	5376	11844	25669
1.2		8570	18887	39794	1.2		7553	16645	36184
1.4		11258	24939	52661	1.4		10102	22268	48425
1.6		14317	31834	67456	1.6		13025	28722	62381
1.8.		17747	39572	83980	1.8.		16320	36004	78030
2.0		21547	48153	102266	2.0		19988	44092	95352

Table H.2: CFD pressure drop (Pa) data for the unit cell-size simulations of the SD TPMS.

1mm unit cell	SD Sheet				2mm unit cell	SD Sheet			
Relative Density	20 %	30 %	40 %	50 %	Relative Density	20 %	30 %	40 %	50 %
Velocity (m/s)	Pressure (Pa)	Pressure (Pa)	Pressure (Pa)	Pressure (Pa)	Velocity (m/s)	Pressure (Pa)	Pressure (Pa)	Pressure (Pa)	Pressure (Pa)
1.0	26247	38350	61070	96260	1.0	19544	28872	46245	73096
1.2	34689	50789	81004	127905	1.2	26417	39135	62803	99416
1.4	44125	64730	103380	163461	1.4	34233	50834	81704	129519
1.6	54539	80158	128169	202890	1.6	42986	63962	102944	163374
1.8	65921	97057	155347	246169	1.8	52668	78511	126505	200953
2.0	78258	115415	184902	293272	2.0	63279	94473	152366	242228
1mm unit cell	SD Solid				2mm unit cell	SD Solid			
Relative Density	20 %	30 %	40 %	50 %	Relative Density	20 %	30 %	40 %	50 %
Velocity (m/s)	Pressure (Pa)	Pressure (Pa)	Pressure (Pa)	Pressure (Pa)	Velocity (m/s)	Pressure (Pa)	Pressure (Pa)	Pressure (Pa)	Pressure (Pa)
1.0	9196	15672	26584	36335	1.0	7174	12315	20786	28424
1.2	12338	21081	35704	48753	1.2	9766	16769	28291	38669
1.4	15871	27170	45956	62704	1.4	12703	21804	36813	50299
1.6	19783	33919	57305	78140	1.6	15975	27390	46335	63323
1.8	24066	41311	69722	95035	1.8	19564	33522	56847	77731
2.0	28710	49332	83191	113359	2.0	23450	40190	68349	93541

Table H.3: CFD pressure drop (Pa) data for the unit cell-size simulations of the SG TPMS.

1mm unit cell	SG Sheet				2mm unit cell	SG Sheet			
Relative Density	20 %	30 %	40 %	50 %	Relative Density	20 %	30 %	40 %	50 %
Velocity (m/s)	Pressure (Pa)	Pressure (Pa)	Pressure (Pa)	Pressure (Pa)	Velocity (m/s)	Pressure (Pa)	Pressure (Pa)	Pressure (Pa)	Pressure (Pa)
1.0	20247	29322	41852	65880	1.0	15006	22279	31885	50263
1.2	26954	39018	55784	88016	1.2	20377	30207	43302	68130
1.4	34456	49860	71470	112637	1.4	26510	39272	56245	88343
1.6	42736	61811	88657	139737	1.6	33438	49448	70595	110804
1.8.	51782	74877	107348	168995	1.8.	41153	60708	86304	135521
2.0	61601	89074	127662	200912	2.0	49628	73029	103487	162071
1mm unit cell	SG Solid				2mm unit cell	SG Solid			
Relative Density	20 %	30 %	40 %	50 %	Relative Density	20 %	30 %	40 %	50 %
Velocity (m/s)	Pressure (Pa)	Pressure (Pa)	Pressure (Pa)	Pressure (Pa)	Velocity (m/s)	Pressure (Pa)	Pressure (Pa)	Pressure (Pa)	Pressure (Pa)
1.0	5805	11086	19774	35109	1.0	4457	8838	15923	28559
1.2	7725	14921	26737	47629	1.2	6081	12145	21909	39376
1.4	9886	19274	34637	61841	1.4	7944	15948	28780	51875
1.6	12288	24139	43468	77709	1.6	10044	20243	36526	66084
1.8.	14930	29513	53221	95228	1.8.	12382	25026	45133	82053
2.0	17813	35396	63888	114397	2.0	14955	30291	54589	98167

Table H.4: CFD pressure drop (Pa) data for the unit cell-size simulations of the IW-P TPMS.

1mm unit cell	IW-P Sheet				2mm unit cell	IW-P Sheet			
Relative Density	20 %	30 %	40 %	50 %	Relative Density	20 %	30 %	40 %	50 %
Velocity (m/s)	Pressure (Pa)	Pressure (Pa)	Pressure (Pa)	Pressure (Pa)	Velocity (m/s)	Pressure (Pa)	Pressure (Pa)	Pressure (Pa)	Pressure (Pa)
1.0	22519	35040	53325	89285	1.0	17478	27060	41355	68367
1.2	30025	46678	71083	118984	1.2	23933	37005	56411	93110
1.4	38526	59816	91125	152296	1.4	31356	48443	73684	121547
1.6	48014	74443	113418	189255	1.6	39740	61363	93155	153652
1.8	58484	90552	137942	229809	1.8	49072	75752	114819	189292
2.0	69931	108145	164679	273984	2.0	59336	91604	138704	228378
1mm unit cell	IW-P Solid				2mm unit cell	IW-P Solid			
Relative Density	20 %	30 %	40 %	50 %	Relative Density	20 %	30 %	40 %	50 %
Velocity (m/s)	Pressure (Pa)	Pressure (Pa)	Pressure (Pa)	Pressure (Pa)	Velocity (m/s)	Pressure (Pa)	Pressure (Pa)	Pressure (Pa)	Pressure (Pa)
1.0	5929	10315	16784	32170	1.0	4430	7951	12915	25220
1.2	7821	13667	22274	42970	1.2	6020	11051	17936	34709
1.4	9948	17463	28473	55229	1.4	7846	14812	24306	45775
1.6	12312	21726	35391	68952	1.6	9907	19332	32909	58598
1.8	14911	26490	43047	84154	1.8	12202	24709	44204	73637
2.0	17745	31797	51484	100865	2.0	14730	30615	55829	91091

H.2 Second Order Polynomial Fit

This appendix contains plots of the simulation pressure data and their subsequent polynomial fit

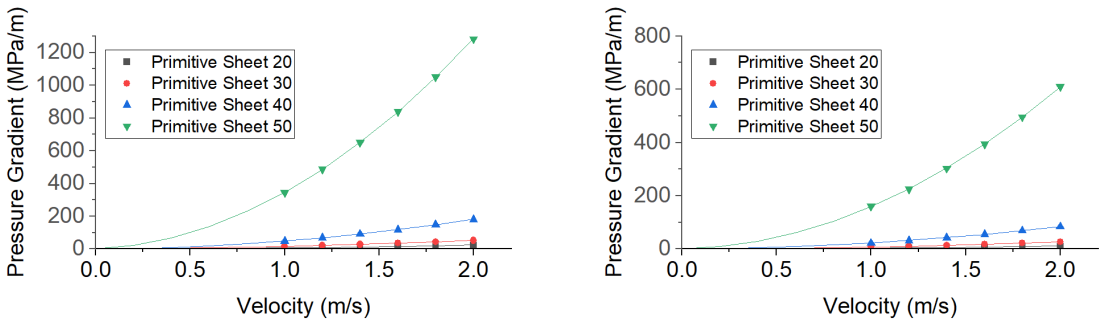

(a) $\alpha = 1$ mm (b) $\alpha = 2$ mm

Figure H.1: Simulation pressure data with respective polynomial fit for SP Sheet. The number in the name denotes relative density D_{rel}.

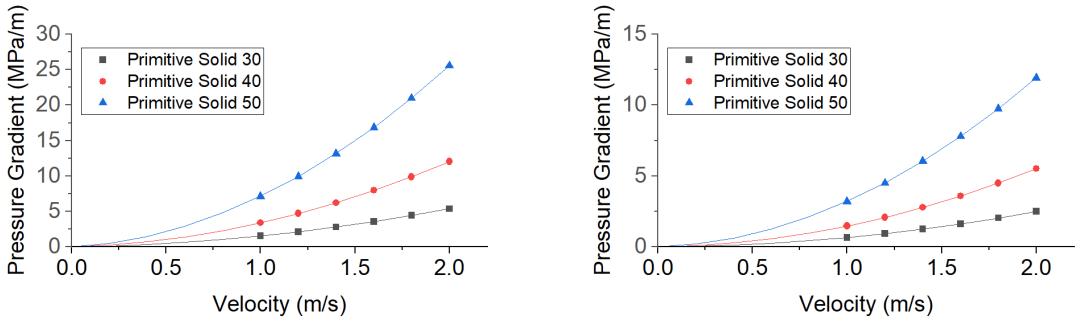

(a) $\alpha = 1$ mm (b) $\alpha = 2$ mm

Figure H.2: Simulation pressure data with respective polynomial fit for SP Solid. The number in the name denotes relative density D_{rel}.

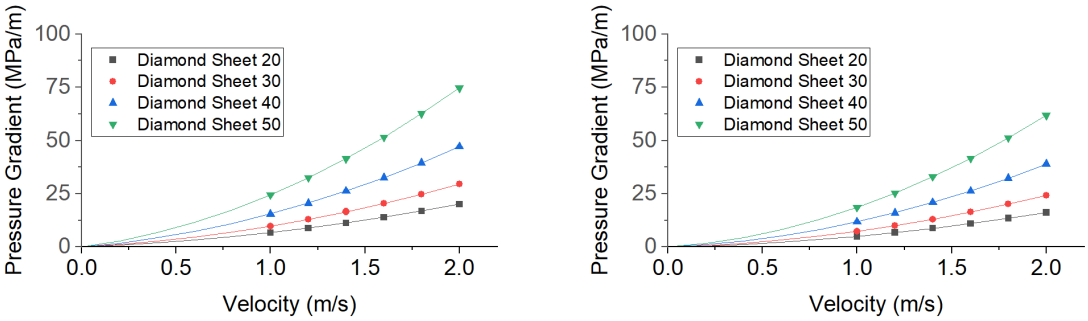

(a) $\alpha = 1$ mm (b) $\alpha = 2$ mm

Figure H.3: Simulation pressure data with respective polynomial fit for SD Sheet. The number in the name denotes relative density D_{rel}.

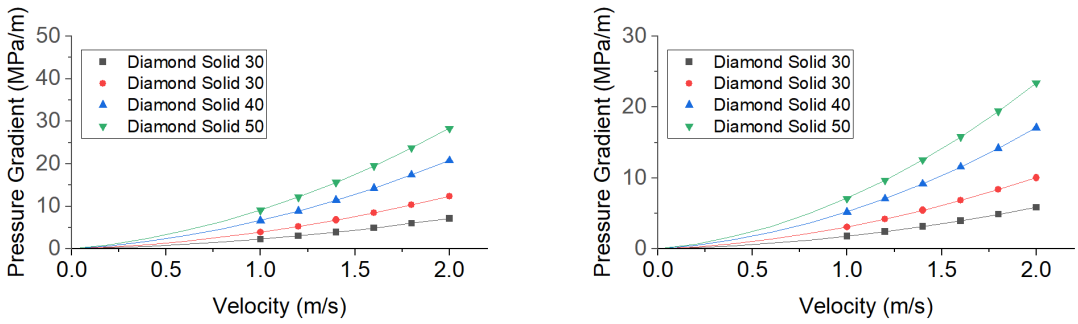

(a) $\alpha = 1$ mm (b) $\alpha = 2$ mm

Figure H.4: Simulation pressure data with respective polynomial fit for SD Solid. The number in the name denotes relative density D_{rel}.

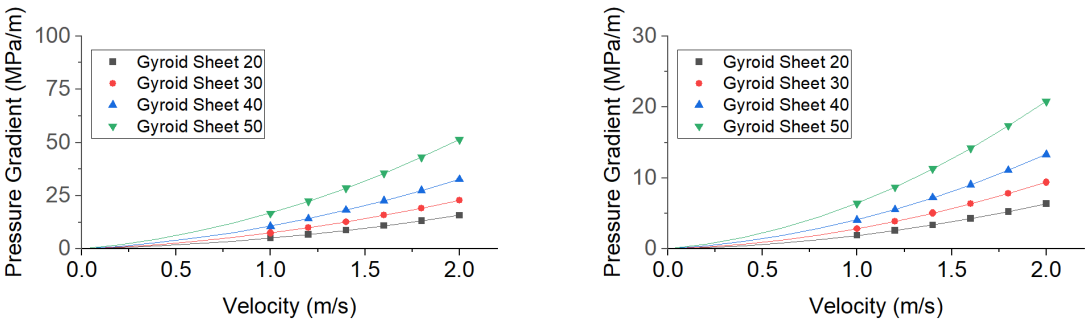

(a) $\alpha = 1$ mm (b) $\alpha = 2$ mm

Figure H.5: Simulation pressure data with respective polynomial fit for SG Sheet. The number in the name denotes relative density D_{rel}.

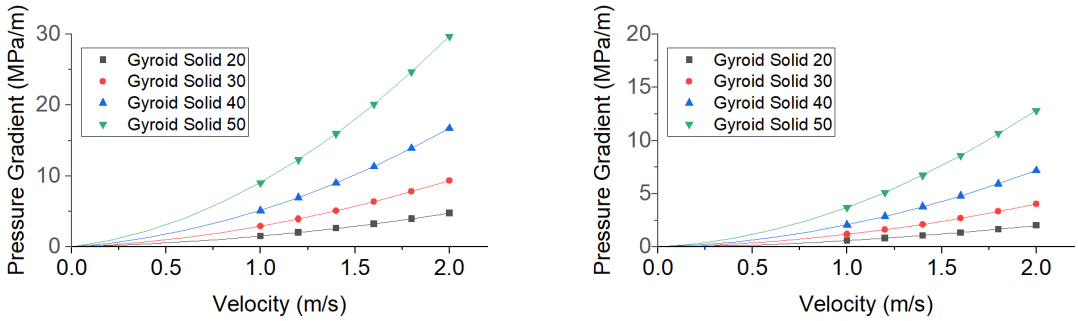

(a) $\alpha = 1$ mm (b) $\alpha = 2$ mm

Figure H.6: Simulation pressure data with respective polynomial fit for SG Solid. The number in the name denotes relative density D_{rel}.

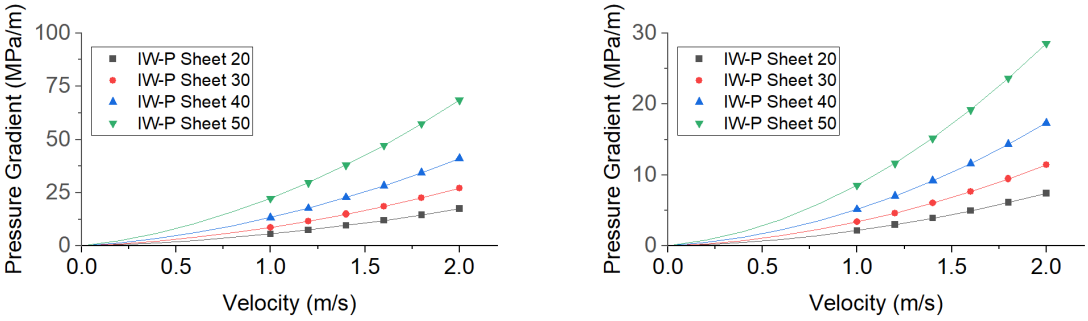

(a) $\alpha = 1$ mm (b) $\alpha = 2$ mm

Figure H.7: Simulation pressure data with respective polynomial fit for IW-P Sheet. The number in the name denotes relative density D_{rel}.

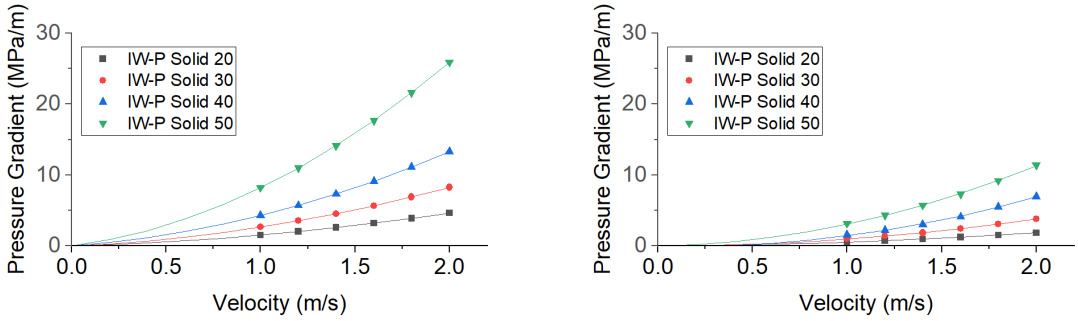

(a) $\alpha = 1$ mm (b) $\alpha = 2$ mm

Figure H.8: Simulation pressure data with respective polynomial fit for IW-P Solid. The number in the name denotes relative density D_{rel}.

I Difference Pressure Drop Data

This section contains the raw data upon which the box plot in Section 6.1 is based.

Table I.1: Full dataset of pressure drop values resultant from simulations and theoretical derivation for the SP geometries.

SP Sheet $\alpha = 1$	$v = 1m/s$			$v = 2m/s$			SP Sheet $\alpha = 2$	$v = 1m/s$			$v = 2m/s$		
D_{rel}	Darcy-Forcheimer	Simulation	Difference	Darcy-Forcheimer	Simulation	Difference	D_{rel}	Darcy-Forcheimer	Simulation	Difference	Darcy-Forcheimer	Simulation	Difference
20 %	68920	69257	0,49%	236023	241491	2,32%	20 %	29221	31486	7,75%	106076	113216	6,73%
30 %	152671	151788	-0,58%	542924	545891	0,55%	30 %	69432	71974	3,66%	257626	264424	2,64%
40 %	483385	482094	-0,27%	1783892	1775152	-0,49%	40 %	224343	225820	0,66%	832536	835175	0,32%
50 %	3450322	3458855	0,25%	12765316	12747096	-0,14%	50 %	1579567	1574735	-0,31%	6064694	6035562	-0,48%
SP Solid $\alpha = 1$	$v = 1m/s$			$v = 2m/s$			SP Solid $\alpha = 2$	$v = 1m/s$			$v = 2m/s$		
D_{rel}	Darcy-Forcheimer	Simulation	Difference	Darcy-Forcheimer	Simulation	Difference	D_{rel}	Darcy-Forcheimer	Simulation	Difference	Darcy-Forcheimer	Simulation	Difference
20 %							20 %						
30 %	15588	17502	12,28%	53841	60447	12,27%	30 %	6712	8740	30,21%	24980		
40 %	34138	36452	6,78%	120351	127779	6,17%	40 %	14785	17153	16,01%	55108		
50 %	71557	73266	2,39%	255741	261388	2,21%	50 %	32215	34846	8,17%	119292		

Table I.2: Full dataset of pressure drop values resultant from simulations and theoretical derivation for the SD geometries.

SD Sheet $\alpha = 1$	$v = 1m/s$			$v = 2m/s$			SD Sheet $\alpha = 2$	$v = 1m/s$			$v = 2m/s$		
D_{rel}	Darcy-Forcheimer	Simulation	Difference	Darcy-Forcheimer	Simulation	Difference	D_{rel}	Darcy-Forcheimer	Simulation	Difference	Darcy-Forcheimer	Simulation	Difference
20 %	65874	67230	2,06%	195836	197978	1,09%	20 %	49013	49844	1,70%	158306	164176	3,71%
30 %	96186	92926	-3,39%	288767	270727	-6,25%	30 %	72382	72842	0,64%	236328	240206	1,64%
40 %	153154	155736	1,69%	462608	465146	0,55%	40 %	115920	116714	0,68%	381144	381165	0,01%
50 %	241406	245686	1,77%	733724	739386	0,77%	50 %	183197	184525	0,73%	605923	605887	-0,01%
SD Solid $\alpha = 1$	$v = 1m/s$			$v = 2m/s$			SD Solid $\alpha = 2$	$v = 1m/s$			$v = 2m/s$		
D_{rel}	Darcy-Forcheimer	Simulation	Difference	Darcy-Forcheimer	Simulation	Difference	D_{rel}	Darcy-Forcheimer	Simulation	Difference	Darcy-Forcheimer	Simulation	Difference
20 %	23157	24905	7,55%	71902	77782	8,18%	20 %	18108	19724	8,92%	58770	64307	9,42%
30 %	39479	40722	3,15%	123557	129951	5,18%	30 %	31104	33043	6,23%	100706	107237	6,49%
40 %	66974	67939	1,44%	208363	210840	1,19%	40 %	52299	53212	1,75%	171105	177574	3,78%
50 %	91522	92778	1,37%	283905	284808	0,32%	50 %	71426	71849	0,59%	234080	238278	1,79%

Table I.3: Full dataset of pressure drop values resultant from simulations and theoretical derivation for the SG geometries.

SG Sheet $\alpha = 1$	$v = 1m/s$			$v = 2m/s$			SG Sheet $\alpha = 2$	$v = 1m/s$			$v = 2m/s$		
D_{rel}	Darcy-Forcheimer	Simulation	Difference	Darcy-Forcheimer	Simulation	Difference	D_{rel}	Darcy-Forcheimer	Simulation	Difference	Darcy-Forcheimer	Simulation	Difference
20 %	50928	52126	2,35%	154218	159884	3,67%	20 %	18769	20589	9,69%	62045	68236	9,98%
30 %	73748	75265	2,06%	222975	225458	1,11%	30 %	27932	29644	6,13%	91366	96975	6,14%
40 %	105456	107463	1,90%	319750	322631	0,90%	40 %	40222	41601	3,43%	129613	135911	4,86%
50 %	166345	169182	1,71%	503313	506948	0,72%	50 %	63403	63858	0,72%	203112	206822	1,83%
SG Solid $\alpha = 1$	$v = 1m/s$			$v = 2m/s$			SG Solid $\alpha = 2$	$v = 1m/s$			$v = 2m/s$		
D_{rel}	Darcy-Forcheimer	Simulation	Difference	Darcy-Forcheimer	Simulation	Difference	D_{rel}	Darcy-Forcheimer	Simulation	Difference	Darcy-Forcheimer	Simulation	Difference
20 %	14547	16061	10,40%	44555	49834	11,85%	20 %	5581	6952	24,57%	18701	23483	25,57%
30 %	27794	29599	6,50%	88546	94580	6,81%	30 %	11081	12779	15,33%	37890	43853	15,74%
40 %	49651	50255	1,22%	159875	164908	3,15%	40 %	19997	21848	9,26%	68309	74499	9,06%
50 %	88264	88806	0,61%	286333	286625	0,10%	50 %	36030	38065	5,65%	123391	129918	5,29%

Table I.4: Full dataset of pressure drop values resultant from simulations and theoretical derivation for the IW-P geometries.

IW-P Sheet $\alpha = 1$	$v = 1m/s$			$v = 2m/s$			IW-P Sheet $\alpha = 2$	$v = 1m/s$			$v = 2m/s$		
D_{rel}	Darcy-Forcheimer	Simulation	Difference	Darcy-Forcheimer	Simulation	Difference	D_{rel}	Darcy-Forcheimer	Simulation	Difference	Darcy-Forcheimer	Simulation	Difference
20 %	56342	57409	1,89%	174868	180204	3,05%	20 %	21895	23900	9,16%	74213	81002	9,15%
30 %	87757	88817	1,21%	270475	270734	0,10%	30 %	33874	35943	6,11%	114547	121342	5,93%
40 %	133654	135004	1,01%	411964	411718	-0,06%	40 %	51777	52653	1,69%	173432	178743	3,06%
50 %	224137	227784	1,63%	685565	689928	0,64%	50 %	85596	85747	0,18%	285654	288163	0,88%
IW-P Solid $\alpha = 1$	$v = 1m/s$			$v = 2m/s$			IW-P Solid $\alpha = 2$	$v = 1m/s$			$v = 2m/s$		
D_{rel}	Darcy-Forcheimer	Simulation	Difference	Darcy-Forcheimer	Simulation	Difference	D_{rel}	Darcy-Forcheimer	Simulation	Difference	Darcy-Forcheimer	Simulation	Difference
20 %	14822	16184	9,19%	44363	49043	10,55%	20 %						
30 %	25626	27232	6,27%	79320	84643	6,71%	30 %						
40 %	41896	42986	2,60%	128620	134874	4,86%	40 %						
50 %	80368	81361	1,24%	252092	253026	0,37%	50 %						